

**A Thesis Submitted for the Degree of PhD at the University of Warwick**

**Permanent WRAP URL:**

<http://wrap.warwick.ac.uk/137021>

**Copyright and reuse:**

This thesis is made available online and is protected by original copyright.

Please scroll down to view the document itself.

Please refer to the repository record for this item for information to help you to cite it.

Our policy information is available from the repository home page.

For more information, please contact the WRAP Team at: [wrap@warwick.ac.uk](mailto:wrap@warwick.ac.uk)

THE CRYSTAL GROWTH AND MICROSTRUCTURE OF SOME NIOBIUM OXIDES

by

MELVILLE DOUGLAS BALL

A dissertation submitted to the University of Warwick for  
admission to the degree of Doctor of Philosophy

Department of Physics

November 1976

#### ACKNOWLEDGEMENTS

I would like to thank Professor A. J. Forty for making available to me the facilities at the Department of Physics. I am indebted to Dr. M. H. Lewis for his continued interest and advice concerning the research and during the preparation of this thesis.

My thanks are due to the Science Research Council for providing the financial support of a research studentship.

I would also like to thank the numerous other people who assisted me during this work, particularly Jim Huckfield for his assistance with the preparation of glass apparatus, Georgina Rogers for typing the thesis, Joan Grant for help in the production of some of the photographs and Gerry Smith for general help in the laboratory.

Finally I would like to thank my parents for their continued support and encouragement, and my wife, Pauline, for her help with the diagrams, her patience and her understanding during the course of this work.

DECLARATION

This dissertation is submitted to the University of Warwick in support of my application for admission to the degree of Doctor of Philosophy. It contains an account of my own work performed at the Department of Physics of the University of Warwick in the period October 1971 to October 1974 under the general supervision of Dr.M.H.Lewis. No part of it has been used previously in a degree submitted to this or any other University. The work described in this thesis is the result of my own independent research except where specifically acknowledged in the text.

M. D. Ball

November 1976

## ABSTRACT

Single crystals of NbO, NbO<sub>2</sub>, Nb<sub>12</sub>O<sub>29</sub>, H-Nb<sub>2</sub>O<sub>5</sub>, B-Nb<sub>2</sub>O<sub>5</sub> and P-Nb<sub>2</sub>O<sub>5</sub> have been prepared by a chemical transport technique using tellurium tetrachloride as the transport reagent.

In some of the crystal growth experiments two species could be grown simultaneously and for Nb<sub>2</sub>O<sub>5</sub> crystals, the stability ranges of the various polymorphs during growth could be deduced.

Under certain conditions Nb<sub>12</sub>O<sub>29</sub> crystals were obtained from a starting material of powdered NbO<sub>2</sub>. Analysis of the growth process indicated that the transport reagent is gradually consumed during the reaction and therefore that the maximum obtainable yield of crystals is related to the initial weight of transport reagent. The gradual decrease of the active transport reagent during this growth process inevitably results in a decreasing growth rate.

A similar "non-conservative" process also occurs during the growth of NbO<sub>2</sub> crystals from powdered NbO.

The crystallography and morphology of the various crystal types were studied by light microscopy, scanning electron microscopy and X-ray techniques. For most of the crystals the facet planes, principal growth directions and twinning relationships were established and from the observations of surface features the most important crystal growth mechanisms were deduced.

Transmission electron microscopy of the "as grown" crystals enables many of the crystal defects to be categorised. Planar defects observed in the NbO<sub>2</sub> crystals are explained as the consequence of the structural transition which occurs as the crystals cool from the growth temperature. The block structures of the higher oxides were studied by lattice imaging. The defects which were observed in this way generally consisted of mistakes

in the ordering of the structural blocks or the incorporation of "wrong sized" blocks. Mechanisms are proposed to account for these defects in terms of the crystal growth processes.

Some of the crystals studied by lattice imaging had a highly irregular structure. Although the basic  $\text{ReO}_3$  type structure was preserved, the blocks were of varying sizes in a random arrangement. Within this disordered structure small ordered domains of  $\text{Nb}_{22}^{0}_{54}$  were found. Another, previously unreported ordered block structure was also observed.

TABLE OF CONTENTS

	<u>Page</u>
CHAPTER ONE - INTRODUCTION .....	1
1.1 Transition Metal Compounds .....	1
1.2 The Niobium-Oxygen System .....	2
1.3 Crystal Growth .....	3
1.4 High Resolution Electron Microscopy (H.R.E.M.) .....	4
1.5 Research Aims .....	5
References .....	6
CHAPTER TWO - EXPERIMENTAL TECHNIQUES OF CRYSTAL PREPARATION ....	7
2.1 Introduction .....	7
2.2 Possible Methods of Crystal Growth .....	7
2.2.1 Growth from the melt .....	7
2.2.2 Solution growth .....	10
2.2.3 Growth from the solid .....	10
2.2.4 Vapour growth .....	10
2.3 Crystal Growth of the Niobium Oxides .....	12
2.4 The Chemical Transport Method .....	15
2.5 Choice of Transport Reagent .....	17
2.6 Starting Materials .....	18
2.7 Crystal Growth Apparatus .....	19
2.8 Experimental Details .....	21
2.8.1 Preparing and loading the reaction tube .....	21
2.8.2 Crystal growth .....	22
2.9 Identification of the Crystals .....	23
2.10 Results .....	24
References .....	28
CHAPTER THREE - THE THERMODYNAMICS AND KINETICS OF THE CHEMICAL TRANSPORT PROCESS .....	30
3.1 Introduction .....	30
3.2 The Chemistry of the Transport Reactions .....	30
3.3 Non-Ideal Chemical Transport Reactions .....	31
3.3.1 The growth of Nb <sub>12</sub> O <sub>29</sub> crystals .....	33
3.4 Thermodynamic Considerations and Chemical Equilibrium .....	38
3.4.1 The equilibrium constant for efficient chemical transport .....	39
3.5 Factors Which Influence the Transport Rate .....	43
3.5.1 Diffusion .....	44
3.5.2 Stefan's flow .....	46
3.5.3 Convection .....	48
3.5.4 The rate-determining processes .....	49
3.5.5 The transport rate in non-conservative systems .....	50

	<u>Page</u>
3.6 The Simultaneous Growth of Different Crystal Species ....	51
3.6.1 The simultaneous growth of NbO <sub>2</sub> and Nb <sub>12</sub> O <sub>29</sub> crystals .....	51
3.6.2 Niobium dioxide and niobium ditelluride .....	52
3.6.3 The polymorphic phases of Nb <sub>2</sub> O <sub>5</sub> .....	54
References .....	55
CHAPTER FOUR - CRYSTAL GROWTH MECHANISMS AND MORPHOLOGY .....	56
4.1 Experimental Techniques .....	56
4.2 The Theories of Crystal Growth from the Vapour .....	57
4.2.1 Continuous or normal growth .....	57
4.2.2 Growth by the propagation of steps .....	58
4.2.3 The island nucleation theory .....	62
4.2.4 The dislocation theory of crystal growth .....	66
4.2.5 The twin plane re-entrant edge mechanism .....	68
4.2.6 Comparison of the various growth theories .....	71
4.3 The Growth Habits of the Niobium Oxides .....	72
4.3.1 Nb <sub>12</sub> O <sub>29</sub> crystals .....	72
4.3.2 Niobium dioxide crystals .....	77
4.3.3 H-Nb <sub>2</sub> O <sub>5</sub> .....	84
4.3.4 P-Nb <sub>2</sub> O <sub>5</sub> .....	86
4.3.5 B-Nb <sub>2</sub> O <sub>5</sub> .....	87
4.3.6 Niobium monoxide (NbO) .....	87
4.3.7 Niobium ditelluride (NbTe <sub>2</sub> ) .....	88
4.4 Summary .....	89
References .....	90
CHAPTER FIVE - EXAMINATION OF THE CRYSTALS BY TRANSMISSION ELECTRON MICROSCOPY .....	92
5.1 Electron Diffraction and Image Formation in the Trans- mission Electron Microscope .....	92
5.1.1 Electron diffraction .....	92
5.1.2 Image formation by diffraction contrast .....	94
5.1.3 The formation of lattice images .....	96
5.1.4 Factors influencing the contrast in lattice images .....	99
5.2 Experimental Techniques for Electron Microscopy .....	103
5.2.1 Specimen preparation .....	103
5.2.2 The electron microscopes .....	103
5.2.3 Obtaining lattice images .....	104
5.3 The Microstructure of NbO <sub>2</sub> Crystals .....	105
5.3.1 Electron diffraction .....	107
5.3.2 Contrast at antiphase boundaries .....	110
5.3.3 Antiphase boundaries in NbO <sub>2</sub> .....	111
5.3.4 The formation of antiphase domains in NbO <sub>2</sub> .....	114



	<u>Page</u>
5.4 Electron Microscopy of the Nb <sub>12</sub> O <sub>29</sub> Crystals .....	116
5.4.1 Electron diffraction .....	118
5.4.2 Lattice imaging of Nb <sub>12</sub> O <sub>29</sub> .....	118
5.4.3 The generation of defects in Nb <sub>12</sub> O <sub>29</sub> crystals ....	121
5.5 Oxides of Undetermined Stoichiometry .....	123
5.5.1 Electron diffraction and high resolution electron microscopy .....	123
5.5.2 Evidence relating to the growth of these crystals.	125
5.6 The Microstructure of H-Nb <sub>2</sub> O <sub>5</sub> Crystals .....	128
5.6.1 Electron diffraction and lattice imaging .....	129
References .....	131
CHAPTER SIX - SUMMARY AND DISCUSSION .....	133
6.1 The Chemical Transport Growth Technique .....	133
6.2 Chemical Transport Growth in Related Systems .....	134
6.3 Non-ideal Chemical Transport .....	134
6.4 Crystal Growth Mechanisms .....	137
6.5 The Microstructure of the Crystals .....	138
6.6 Non-Stoichiometry .....	138
References .....	142

	<u>Page</u>
5.4 Electron Microscopy of the Nb <sub>12</sub> O <sub>29</sub> Crystals .....	116
5.4.1 Electron diffraction .....	118
5.4.2 Lattice imaging of Nb <sub>12</sub> O <sub>29</sub> .....	118
5.4.3 The generation of defects in Nb <sub>12</sub> O <sub>29</sub> crystals ....	121
5.5 Oxides of Undetermined Stoichiometry .....	123
5.5.1 Electron diffraction and high resolution electron microscopy .....	123
5.5.2 Evidence relating to the growth of these crystals.	125
5.6 The Microstructure of H-Nb <sub>2</sub> O <sub>5</sub> Crystals .....	128
5.6.1 Electron diffraction and lattice imaging .....	129
References .....	131
CHAPTER SIX - SUMMARY AND DISCUSSION .....	133
6.1 The Chemical Transport Growth Technique .....	133
6.2 Chemical Transport Growth in Related Systems .....	134
6.3 Non-ideal Chemical Transport .....	134
6.4 Crystal Growth Mechanisms .....	137
6.5 The Microstructure of the Crystals .....	138
6.6 Non-Stoichiometry .....	138
References .....	142

LIST OF FIGURES

<u>Figure</u>	<u>Page No.</u>
1.1 Phase diagram of the Nb-O system (after Elliot (6)) ...	2
1.2 Schematic diagram of the $\text{ReO}_3$ -type structure .....	2
a. $\text{ReO}_6$ octahedron	
b. One $\text{ReO}_3$ layer of the $\text{ReO}_3$ structure showing the corner sharing octahedra	
2.1 The silica reaction tubes used for chemical transport .	19
2.2 a. Temperature profile recommended by Schafer (3) .....	20
b. A typical temperature profile used in this work .....	20
2.3 A schematic diagram of the furnace .....	20
2.4 The reaction tube after a typical growth experiment. The fine needle-shaped crystals are $\text{H-Nb}_2\text{O}_5$ .....	23
3.1 The relationship between the total yield of $\text{Nb}_{12}\text{O}_{29}$ crystals and the initial weight of $\text{TeCl}_4$ .....	37
3.2 Conditions for the growth of $\text{NbO}_2$ and $\text{Nb}_{12}\text{O}_{29}$ .....	51
3.3 Conditions for the growth of $\text{B-Nb}_2\text{O}_5$ and $\text{P-Nb}_2\text{O}_5$ .....	54
4.1 Simple Kossel crystal showing sites at which atoms can become attached .....	58
4.2 Simple representation of an emergent screw dislocation.	58
4.3 The development of a growth spiral .....	66
4.4 Growth by the TPPE mechanism .....	69
4.5 Comparison of the dependence of growth rate on super-saturation for the various growth mechanisms .....	71
4.6 The structures of the two forms of $\text{Nb}_{12}\text{O}_{29}$ .....	72
a. Orthorhombic $\text{Nb}_{12}\text{O}_{29}$ [010] projection	
b. Monoclinic $\text{Nb}_{12}\text{O}_{29}$ [010] projection	
4.7 Twinning in $\text{Nb}_{12}\text{O}_{29}$ (polarised light) .....	73
4.8 Laue back reflection pattern obtained from one branch of the twinned crystal. The principal growth direction is indicated .....	73
4.9 Schematic diagram of the $\text{Nb}_{12}\text{O}_{29}$ block structure showing the stepped nature of the (010) face .....	73
4.10 The positions of preferred sites for growth in the [010] direction .....	73
4.11a. Well developed {011} facets in $\text{Nb}_{12}\text{O}_{29}$ crystals .....	74
b. Schematic diagram showing the arrangement of $\text{NbO}_6$ octahedra at {011} facets .....	74
4.12 The development of {011} facets .....	74
4.13 A possible arrangement of the $\text{NbO}_6$ octahedra at the twin plane in $\text{Nb}_{12}\text{O}_{29}$ .....	76
4.14 Active growth centres along twin boundaries .....	76
4.15 S.E.M. micrograph of "octahedral" $\text{NbO}_2$ crystals .....	78

<u>Figure</u>	<u>Page No.</u>
4.16 S.E.M. micrographs of growth depressions in NbO <sub>2</sub> crystals .....	78
a. Spiral depression	
b. Growth pits on {111} face	
c. Arrays of pits along low angle boundaries	
4.17 The development of "hollow" growth spirals .....	79
4.18 The formation of faceted depressions during growth ..	80
4.19 Laue pattern taken parallel to the growth direction .	81
4.20 Computed [001] stereographic projection for NbO <sub>2</sub> ....	81
4.21 S.E.M. micrographs showing twinned NbO <sub>2</sub> crystals ....	81
4.22 Twinning in NbO <sub>2</sub> .....	82
4.23 S.E.M. micrographs of twin interfaces in NbO <sub>2</sub> crystals for comparison with Figure 4.22 .....	82
a. (10 $\bar{1}$ ) twin plane	
b. (10 $\bar{2}$ ) twin plane	
4.24 A comparison of the TPPE in NbO <sub>2</sub> and Nb <sub>12</sub> O <sub>29</sub> .....	82
4.25 Schematic diagram of the H-Nb <sub>2</sub> O <sub>5</sub> structure [010] projection .....	84
4.26a. Agglomeration of P-Nb <sub>2</sub> O <sub>5</sub> crystals .....	86
b. Surface growth features on a P-Nb <sub>2</sub> O <sub>5</sub> crystal .....	86
4.27a. Twinning in B-Nb <sub>2</sub> O <sub>5</sub> crystal .....	87
b. Steps propagating on the surface of a B-Nb <sub>2</sub> O <sub>5</sub> crystal	
4.28 SEM micrograph of a "crust" of NbO crystals .....	88
4.29 Plates of NbTe <sub>2</sub> showing growth steps and domain structure (polarised light) .....	88
5.1 The Ewald sphere construction .....	94
5.2 The Rutile type unit cell .....	105
5.3 The Rutile structure indicating the arrangement of NbO <sub>6</sub> octahedra .....	105
5.4 The arrangement of Rutile-type units in the low temperature structure of NbO <sub>2</sub> .....	105
5.5 Electron diffraction patterns for NbO <sub>2</sub> .....	108
5.6 APB's in NbO <sub>2</sub> crystals imaged under different conditions .....	111
5.7 APB's in NbO <sub>2</sub> .....	111
5.8 APB generated by a dislocation .....	115
5.9 Superdislocations in NbO <sub>2</sub> crystals .....	115
5.10 Electron diffraction patterns for Nb <sub>12</sub> O <sub>29</sub> .....	118
5.11 1-d lattice image of a bent region of Nb <sub>12</sub> O <sub>29</sub> .....	118
5.12 Electron diffraction pattern showing the position of the objective aperture used for lattice imaging .....	119

<u>Figure</u>	<u>Page No.</u>
5.13 1-d lattice images of faulted regions of Nb <sub>12</sub> O <sub>29</sub> ...	119
5.14 Schematic diagrams showing the arrangements of blocks at faults in Nb <sub>12</sub> O <sub>29</sub> .....	119
5.15 The possible arrangement of blocks at a type D fault in Nb <sub>12</sub> O <sub>29</sub> .....	120
5.16 [010] diffraction pattern for Nb <sub>12</sub> O <sub>29</sub> showing the position of the objective aperture for lattice imaging .....	120
5.17 Lattice image of ortho-Nb <sub>12</sub> O <sub>29</sub> .....	120
5.18 High magnification image of Nb <sub>12</sub> O <sub>29</sub> showing the structure within the blocks .....	120
5.19 Initiation of a new block at the TPRES .....	122
5.20 Diffraction pattern obtained from the disordered crystals .....	123
5.21 Disordered block structure .....	123
5.22 Part of a "disordered" crystal containing large domains of Nb <sub>22</sub> O <sub>54</sub> .....	123
5.23 The idealised Nb <sub>22</sub> O <sub>54</sub> structure .....	124
5.24 A region containing a small domain of an ordered block arrangement .....	124
5.25 A diagram showing a possible arrangement of the blocks .....	124
5.26a. A disordered region containing large blocks .....	124
b. Diagram of the arrangement of blocks	
5.27 A possible mechanism for the incorporation of "wrong-sized" blocks .....	126
5.28 Variations in block size which could occur during the propagation of steps .....	127
5.29 Diffraction patterns for H-Nb <sub>2</sub> O <sub>5</sub> .....	129
a. Pattern from a 'perfect' region of crystal showing the position of the objective aperture used for lattice imaging	
b. Pattern from a twinned region showing the extra 'twin' spots	
5.30 Area of H-Nb <sub>2</sub> O <sub>5</sub> containing various types of faults .	129
5.31 A twin lamella in H-Nb <sub>2</sub> O <sub>5</sub> .....	129
5.32 Area of H-Nb <sub>2</sub> O <sub>5</sub> containing large twinned regions ...	129
5.33 A faulted region in H-Nb <sub>2</sub> O <sub>5</sub> .....	130

CHAPTER ONE

INTRODUCTION

1.1 Transition Metal Compounds

Advances in the understanding of the mechanical and electrical properties of transition metal compounds have resulted in a marked increase in their application both as engineering materials and in the field of solid state electronic devices. The understanding of the electronic properties of solid compounds of transition metals constitutes one of the most challenging problems in solid state physics, but already the growing research effort in this field has led to the exploitation of some of these materials in novel devices.

One such material which has been the subject of extensive research is vanadium dioxide ( $\text{VO}_2$ ). In 1959 Morin (1) reported the existence of a first order semiconductor-to-metal transition in  $\text{VO}_2$  at a temperature  $T_t \approx 340^\circ\text{K}$ . Changes of conductivity at the transition temperature of five orders of magnitude have been observed (2). Clearly this phenomenon suggests the possible use of crystals of  $\text{VO}_2$  as thermally induced switching devices. The conductivity change exhibited by  $\text{VO}_2$  at its transition temperature is accompanied by a change in reflectivity. This property has been utilised in the development of a prototype permanent erasable holographic information storage system (3), the phase transition being induced in a thin film of  $\text{VO}_2$  by the action of a ruby laser.

Several other oxides have also been found to exhibit a similar semiconductor-to-metal phase transition including  $\text{NbO}_2$ , however in this case the transition temperature is about  $1068^\circ\text{K}$  (4) and consequently the range of potential applications is limited.

The understanding of these transitions and other phenomena in terms of the electronic band structure of materials relies on a detailed knowledge of the crystal structures and on the role and distribution of crystalline defects such as impurity atoms or vacancies.

### 1.2 The Niobium-Oxygen System

The existence of the three principal oxides of niobium, NbO, NbO<sub>2</sub> and Nb<sub>2</sub>O<sub>5</sub>, was firmly established by Brauer in 1941 (5) using X-ray diffraction. By 1959, Elliot (6) was able to construct a phase diagram (fig. 1.1) for the Nb-O system based on his metallographic, X-ray and incipient melting data. His measurements indicated that both NbO and NbO<sub>2</sub> have negligible ranges of solid solubility, whereas Nb<sub>2</sub>O<sub>5</sub> shows a small solubility range. A peritectic reaction between NbO<sub>2</sub> and Nb<sub>2</sub>O<sub>5</sub> was postulated.

More recent work has resulted in the discovery of two additional groups of niobium oxides, the suboxides with compositions lying between Nb and NbO, and the group of oxides with compositions between NbO<sub>2</sub> and Nb<sub>2</sub>O<sub>5</sub>. Oxidation studies of niobium under low oxygen partial pressures indicated the existence of three distinct suboxide phases (7, 8, 9). There is some dispute as to the status of these suboxide phases but it is generally considered that they should be regarded as unstable "transient" phases which form during the course of reaction (10).

Numerous oxides have been discovered in the composition range between NbO<sub>2</sub> and Nb<sub>2</sub>O<sub>5</sub> and most of these compounds are structurally related to ReO<sub>3</sub>. The ReO<sub>3</sub> structure can be described as an infinite three dimensional array of corner sharing ReO<sub>6</sub> octahedra (fig. 1.2). The structures of the niobium oxides can be derived from this by a process of "crystallographic shear".\*

\* See note overleaf

Note:

The crystallographic shear process by which the structure of the higher oxides of Nb is derived from the  $\text{ReO}_3$  structure can be considered in two stages:-

- (a) the elimination of an ordered array of planes of oxygen atoms.
- (b) at each of these planes, the structure on one side is displaced (sheared) with respect to the structure on the other side.

The net effect of this process is that some of the octahedra now share common edges and the Nb : O ratio is increased. Variations in the shear plane spacings lead to corresponding changes in the composition.



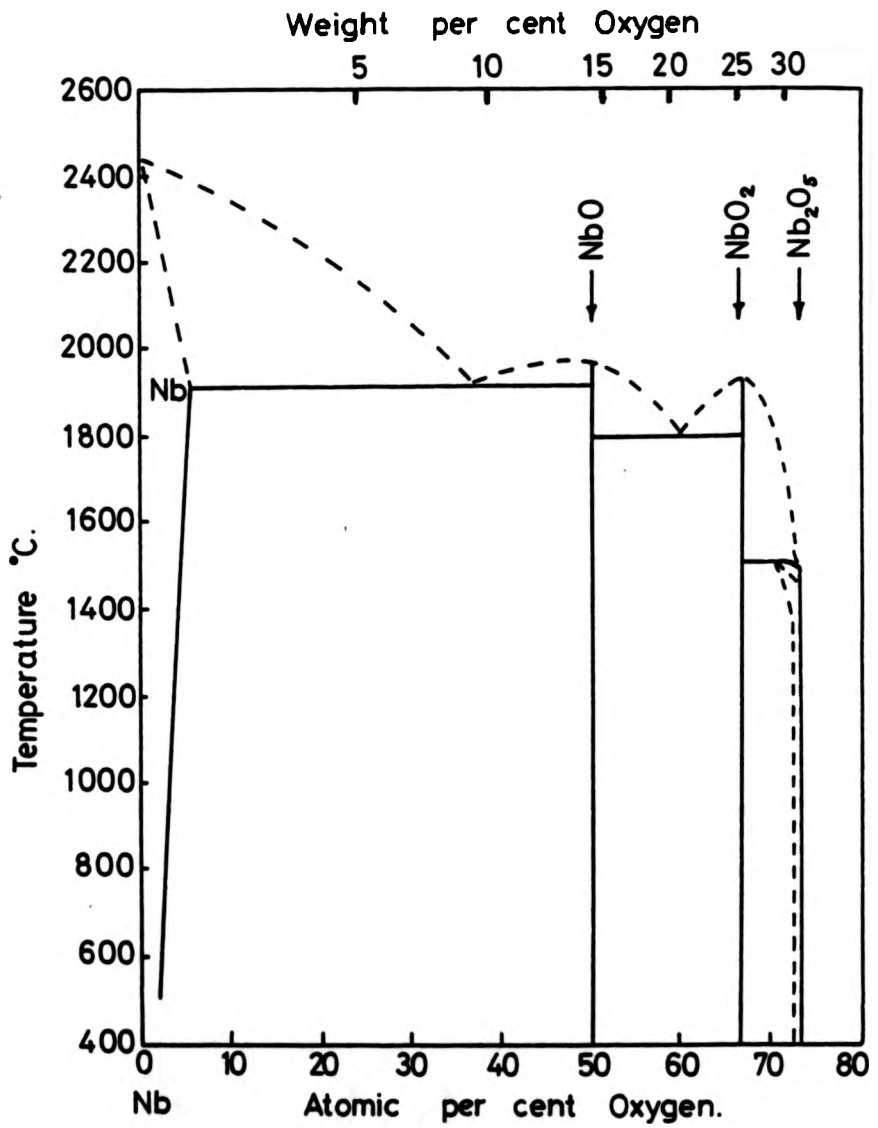
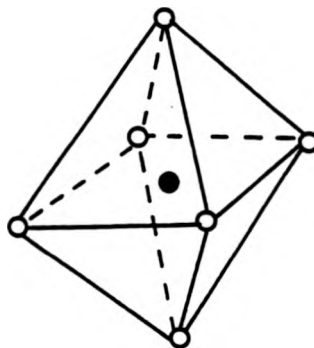


Fig. 1.1. Phase diagram of the Nb-O system (after Elliot (6))

(a)  $\text{ReO}_6$  octahedron.

● - Re  
○ - O



(b) One layer of the  $\text{ReO}_6$  structure showing the corner sharing octahedra.

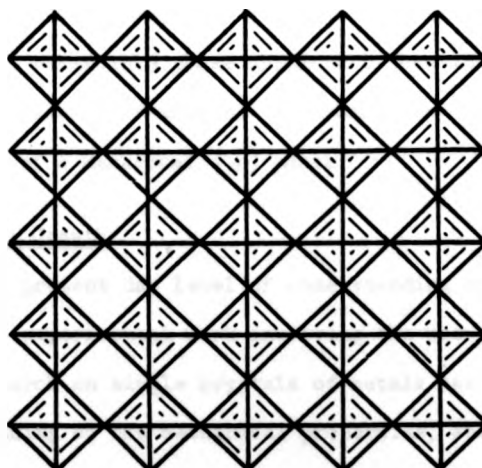


Fig. 1.2. Schematic diagram of the  $\text{ReO}_6$ -type structure.

the idealised  $\text{ReO}_3$  structure in such a way that the bonding between some of the octahedra is changed from corner sharing to edge sharing.

Several of these oxides form a homologous series with the general formula  $\text{Nb}_{3n+1}\text{O}_{8n-2}$  (11). Other oxides in this composition range can be regarded as being made up of ordered microdomains of two of the members of the series. Several reviews of such "intergrowth" structures and shear structure compounds have been published. (see for example reviews by Wadsley (12), Anderson (13) and Allpress and Sanders (14)).

S. Kimura (15) has measured the melting points of several of these structurally related oxides including  $\text{H-Nb}_2\text{O}_5$  and found that in all cases, melting occurs at the same temperature ( $1492^\circ\text{C} \pm 3^\circ\text{C}$ ), and no eutectic or peritectic behaviour could be detected.

More detailed crystallographic studies of  $\text{Nb}_2\text{O}_5$ , reviewed by Schafer (16) have revealed the existence of a large number of polymorphic forms of  $\text{Nb}_2\text{O}_5$ . In addition to the  $\alpha\text{-Nb}_2\text{O}_5$  (also referred to as  $\text{H-Nb}_2\text{O}_5$ ) reported by Brauer (5) at least twelve other crystallographic forms have been distinguished.

All the niobium oxide phases which have been described so far have been observed in bulk samples. However Terao (17, 18) has reported at least one additional metastable phase obtained by heating thin films of niobium in low partial pressures of oxygen. From his X-ray diffraction data he suggested the existence of a hexagonal ( $\delta$ ) phase.

### 1.3 Crystal Growth

The present day level of understanding of solid state physics owes a lot to experimental work involving the use of single crystals. For example, research on single crystals of metals has considerably advanced the understanding of the mechanical properties, and single crystal whiskers

have been prepared which display yield strengths one thousand times greater than previously obtained.

Single crystals are also in great demand for research into radiation damage, superconductivity, N.M.R., E.S.R., molecular structure determination and many other fields. Probably the most important application of single crystal technology is in the field of semiconductor devices. A great deal of research is aimed at understanding the band structure, electrical and optical properties of a range of suitable crystalline materials.

The dramatic effects of impurities and crystalline imperfections on the electrical properties of semiconductors, highlights the need to understand the processes involved in the growth of crystals. Already improvements in growing techniques and in the control of impurity doping levels have led to the production of higher quality semiconductor devices. In the niobium-oxygen system, the use of high resolution electron microscopy has enabled structural imperfections of unit cell dimensions to be directly observed. By the use of this technique a more accurate description of the crystalline defects can be determined and evidence can be obtained concerning the role of defects in the growth of these crystals.

#### 1.4 High Resolution Electron Microscopy (H.R.E.M.)

The information which can be obtained by single crystal X-ray techniques can enable the mean atomic positions within the unit cell to be determined to better than 0.1 nm. However an inherent disadvantage of such methods is that the data obtained is an average over a relatively large volume of the sample. In order to study the subtle structural variations which occur in the niobium oxides a technique with higher spatial sensitivity is required.

Supplementary diffraction information can be obtained by selected area electron diffraction or by microbeam diffraction (in a Scanning Transmission Electron Microscope). However in recent years, improvements in electron microscopes and techniques have enabled structural details of features approaching atomic dimensions to be resolved and interpreted. The use of such techniques in the study of niobium oxides and other complex structures has enabled localised variations in crystal structure to be observed. In this work H.R.E.M. is used extensively both to distinguish between the more complex niobium oxides and to investigate the grown-in defects.

#### 1.5 Research Aims

The principal aims of this work were as follows:-

- (a) To develop a versatile crystal growing technique suitable for the preparation of single crystals of several of the niobium oxides.
- (b) To optimise as far as possible the growth conditions for each particular species.
- (c) To study the thermodynamic, chemical and crystallographic factors which influence the crystal growth.
- (d) To establish the role of crystalline defects on the growth of crystals.
- (e) To study the variations in microstructure with growth conditions.

In chapter two, crystal growth methods are discussed and the reasons for selecting the chemical transport method are presented. The later sections of the chapter describe the experimental conditions used for the growth of the various crystal species.

The third chapter is a more detailed investigation of the chemical transport process. In particular the factors which control the growth rate and the eventual yield of crystals are discussed.

The early part of chapter four reviews the various theories of growth from the vapour and particularly the relationship between growth rate and supersaturation. The subsequent sections of this chapter describe morphological observations of the crystals and on the basis of this evidence, the probable growth mechanisms are deduced.

Chapter five describes the investigation of some of the crystal species by transmission electron microscopy. Where possible the defect structures observed by both conventional transmission microscopy and by H.R.E.M. are analysed and interpreted in terms of the crystal growth process.

The final chapter attempts to summarise the important conclusions of this work and to interpret these findings in terms of reported work on other systems.

REFERENCES

1. F.J. Morin, Phys. Rev. Lett., 3, 34, (1959).
2. L.A. Ladd and W. Paul, Solid State Commun., 7, 425, (1969).
3. W.R. Roach, Applied Phys. Lett., 19, 453-455, (1971).
4. R.F. Janninck and D.H. Whitmore, J. Phys. Chem. Solids, 27, 1183-1187, (1966).
5. G. Brauer, Z. anorg. Chem., 248, 1-31, (1941).
6. R.P. Elliot, Trans. A.S.M., 52, 990-1014, (1959).
7. T. Hurlen, J. Inst. M., 89, 273-280, (1960-61).
8. N. Norman, J. Less Common Metals, 4, 52-61, (1962).
9. N. Norman, P. Kofstad, O.J. Krudtaa, J. Less Common Metals, 4, 124-137, (1962).
10. H.J. Goldschmidt, J. Inst. Metals, 235, (1968 - 69).
11. B.M. Gatehouse and A.D. Wadsley, Acta Cryst., 17, 1545, (1964).
12. A.D. Wadsley in "Non-stoichiometric Compounds", Ed. L. Mandelcorn, Academic Press. New York, 98-209, (1964).
13. S. Anderson, Bull. Soc. fr. Mineral Cristallogr., 522-527, (1967).
14. J.G. Allpress and J.V. Sanders, J. Appl. Cryst., 6, 165-190, (1973).
15. S. Kimura, Internat. Crystallogr. Conf., Melbourne, (1974).
16. H. Schafer, Angew. Chem. Internat. Edit., 5, 40-52, (1966).
17. N. Terao, Japan J. Appl. Physics, 2, 156-174, (1963).
18. N. Terao, Japan J. Appl. Physics, 4, 8-15, (1965).

## CHAPTER TWO

### EXPERIMENTAL TECHNIQUES OF CRYSTAL PREPARATION

#### 2.1 Introduction.

Single crystals of transition metal oxides are generally difficult to grow and the oxides of niobium are no exception. The high melting points, low electrical conductivities and chemical instability often demand the use of specialised techniques. This necessitates a careful evaluation of the possible growth methods.

In this chapter the most promising crystal growth techniques are discussed, with particular reference to the growth of the oxides of niobium and the experimental procedure which was eventually adopted is described in detail. Measurements of the growth rates, crystal dimensions and yields were recorded under different conditions of growth and the growth conditions which resulted in the highest yields are presented for each species of crystal obtained.

#### 2.2 Possible Methods of Crystal Growth.

##### 2.2.1 Growth from the melt.

The most common methods of producing single crystals of ceramic materials involve growth from the melt. Many techniques have been developed according to the material involved. These techniques can be conveniently subdivided into those which involve the use of a crucible and those which do not.

##### (a) Methods involving the containment of a melt in a crucible.

If a suitable crucible material exists which will stay sufficiently robust up to the melting point of the crystal to be grown, and will not react chemically with the melt, large single



crystals can often be prepared. Two commonly used techniques involving the use of a crucible are the Czochralski and Bridgman methods.

Containment in a crucible at high temperatures almost inevitably leads to a degree of contamination of the melt and for this reason methods have been developed in which the melt is contained in a water-cooled hearth, usually made of copper. Reed et al. (1, 2) have succeeded in growing several high melting point materials by arc melting using such a technique.

(b) Crucible-free techniques.

Crucible-free methods such as the floating zone technique eliminate the problems of chemical reactivity, contamination and containment of the melt by a crucible and consequently, high purity single crystals can be produced (3, 4). The Verneuil or flame fusion process can also be useful in the preparation of single crystals of non-reactive compounds such as  $Al_2O_3$ , but in compounds of variable stoichiometry, control of the composition is difficult (5).

Successful growth of single crystals of refractory materials from the melt requires an efficient heating method. For materials with reasonably high electrical conductivity, there are several possible ways of heating the charge to its melting point. High

frequency (HF) induction heating, electron beam heating, arc discharge or simply Joule heating can often be employed successfully. However, in the case of electrical insulators, indirect methods of heating have to be employed. For example, the melting of some non-conductive materials has been achieved by the use of heated crucibles, HF susceptors placed close to the charge and by electron beam heating using electrons accelerated towards the charge by a positively biased grid. These heating methods are inevitably less efficient than the corresponding direct heating of the charge, and for this reason the melting of high temperature non-conducting materials can present severe practical difficulties.

Although a large range of crystals can be grown from the melt, there are certain classes of materials for which this method is impossible. In some cases the material is chemically unstable at temperatures below its melting point. Some materials undergo a peritectic reaction during solidification, whilst in other cases the crystals undergo structural transformations during cooling from the melting point often causing serious disruption. Where several polymorphic forms of a particular compound can exist, it is often only possible to prepare crystals of the high temperature modification.

In general, crystals grown from the melt are subjected to large temperature gradients and can consequently have high concentrations of defects due to the thermally induced stresses. These may be either macroscopic (cracks) or microscopic (dislocations etc.). The main advantage of crystal growth from the melt is the

size of the crystals which can be produced. Crystals of several cubic centimetres are common and for some materials under the right conditions extremely large single crystals can be prepared.

#### 2.2.2 Solution growth.

Where a suitable flux exists, single crystals may be prepared by precipitation from a supersaturated solution. If the precipitating crystals have markedly different solubilities at high and low temperatures, supersaturation can be achieved by slow cooling. Supersaturation will also result from flux evaporation and some crystal growth processes rely on this mechanism.

Crystals can be grown from solution at temperatures significantly below their melting points and this can be an important advantage in cases where thermally induced defects or disruptive phase transitions occur. However, one disadvantage of the method is that the resulting crystals are often contaminated by the flux material.

The use of this technique is limited to systems for which a suitable solvent flux is available.

#### 2.2.3 Growth from the solid.

The high temperature strain-annealing method developed by Fleischer and Tobin (6) has been successfully used to prepare large grain-sized rods, and in some cases, single crystals of some transition metal carbides. In principle the strain-annealing method is applicable to a wide range of materials for which suitable rods can be prepared.

#### 2.2.4 Vapour growth.

Vapour growth involves the transport of a solid, usually from a region of higher temperature to a region of lower temperature via an intermediate gaseous phase.

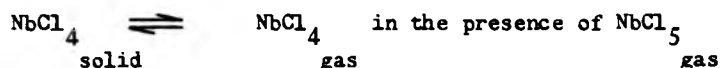
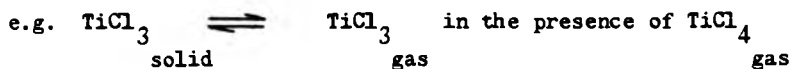
Schafer (7) has classified such processes into the following five categories:-

(a) Sublimation.

Certain solids when heated will readily vaporise and can subsequently condense in a lower temperature region. e.g. iodine, lithium fluoride.

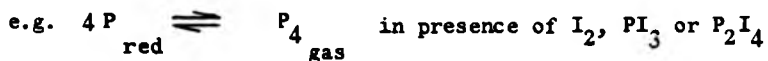
(b) Sublimation with suppression of thermal decomposition.

Some solids which would normally decompose below the sublimation temperature can be stabilised by the presence of another component and are then able to sublime as described in (a) above.



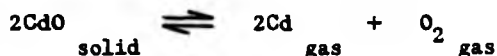
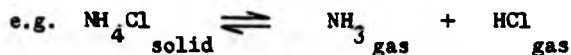
(c) Catalytic sublimation.

In certain cases sublimation is facilitated by the presence of a catalytic agent.



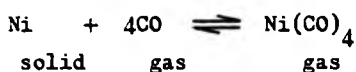
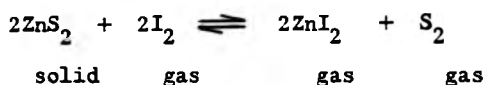
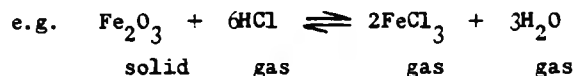
(d) Thermal decomposition and recombination (dissociative sublimation).

In this case the solid dissociates on heating into two or more gaseous phases which when cooled will recombine to produce the original solid.



(e) Chemical transport.

In the chemical transport process a gaseous reagent reacts with the solid, usually in a high temperature region, to form volatile products. At a lower temperature zone, this reaction is reversed, regenerating the solid and the gaseous transport reagent.



N.B. in this case the forward reaction is endothermic and hence transport takes place from the low temp. zone to the higher temp. zone.

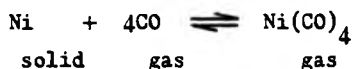
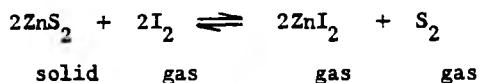
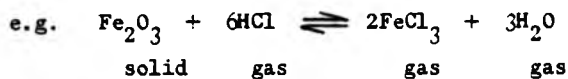
2.3 Crystal Growth of the Niobium Oxides .

Ideally a versatile crystal growth method is required, which, by suitable modification, will enable the whole range of oxides of niobium to be produced. Such a method would enable meaningful comparisons of growth kinetics and parameters to be made.

Methods have been developed for the growth of certain niobium oxides from the melt. NbO is the most chemically reactive of the niobium oxides and this leads to problems of melt containment. However, Reed and Pollard (2) have been able to overcome these difficulties by using a water cooled copper hearth and an arc melting technique. Single crystals of the high temperature form of Nb<sub>2</sub>O<sub>5</sub> (H-Nb<sub>2</sub>O<sub>5</sub>) have also been successfully grown

(e) Chemical transport.

In the chemical transport process a gaseous reagent reacts with the solid, usually in a high temperature region, to form volatile products. At a lower temperature zone, this reaction is reversed, regenerating the solid and the gaseous transport reagent.



N.B. in this case the forward reaction is endothermic and hence transport takes place from the low temp. zone to the higher temp. zone.

2.3 Crystal Growth of the Niobium Oxides.

Ideally a versatile crystal growth method is required, which, by suitable modification, will enable the whole range of oxides of niobium to be produced. Such a method would enable meaningful comparisons of growth kinetics and parameters to be made.

Methods have been developed for the growth of certain niobium oxides from the melt. NbO is the most chemically reactive of the niobium oxides and this leads to problems of melt containment. However, Reed and Pollard (2) have been able to overcome these difficulties by using a water cooled copper hearth and an arc melting technique. Single crystals of the high temperature form of Nb<sub>2</sub>O<sub>5</sub> (H-Nb<sub>2</sub>O<sub>5</sub>) have also been successfully grown

from the melt. Sheasby et al. (8, 9) used a Verneuil flame fusion method and Shindo et al. (10) used a floating zone technique using a halogen lamp image furnace.

Niobium dioxide has a high electrical resistivity and a high melting point ( $\approx 2080^{\circ}\text{C}$ ). In order to establish the feasibility of growing  $\text{NbO}_2$  crystals from the melt using the available facilities, an attempt was made to melt a charge of  $\text{NbO}_2$  in an iridium crucible. This method has been successfully employed in the growth of rutile ( $\text{TiO}_2$ ) single crystals (11). The crucible containing compressed  $\text{NbO}_2$  powder was positioned in an H.F. coil in a sealed crystal growth chamber. The chamber was evacuated and then pressurised with high purity argon.

The iridium is an efficient H.F. susceptor and the temperature was increased by increasing the power output of the H.F. generator. By this means the  $\text{NbO}_2$  charge was successfully melted. However, careful inspection revealed that the molten  $\text{NbO}_2$  had slowly attacked the grain boundary regions of the iridium crucible, and consequently this approach was abandoned.

It is evident from this preliminary survey that the growth of niobium oxides from the melt is extremely difficult. In addition to the practical difficulties, only one of the several polymorphic forms of  $\text{Nb}_2\text{O}_5$  is stable above  $900^{\circ}\text{C}$  and hence the growth of the other forms from the melt is impossible.

Because of the large variation in properties between the niobium oxides it is unlikely that a versatile solution growth technique could be devised. Generally solution growth methods have been developed for particular crystalline phases. For example in the closely related vanadium-oxygen system, crystals of  $\text{VO}_2$  have been synthesised using molten

$V_2O_5$  as a flux (12). However crystals of other vanadium oxides such as  $V_2O_3$  have not been produced using this method.

Although in principle, the strain annealing method can be applied to many materials, suitable polycrystalline rods must first be prepared. The difficulties of preparing such rods for the niobium oxides are comparable with the problems which are encountered in growth from the melt.

Several oxides of niobium have been successfully grown as single crystals by chemical transport methods. Schafer (13) first reported the growth of NbO and  $NbO_2$  crystals by chemical transport using iodine as the reagent. However the growth rates obtained in this work were low. Using  $NbCl_5$  as transport reagent, Schafer (14) was also able to prepare several forms of  $Nb_2O_5$ . More recently crystals of  $NbO_2$  and  $Nb_{12}O_{29}$  have been grown using  $TeCl_4$  (15),  $TeBr_4$  and  $NH_4Br$  (16).

These results suggest that, by a suitable choice of transport reagent and growth conditions, it should be possible to prepare single crystals of most of the oxides of niobium. Furthermore, the use of this type of method enables single crystals to be grown at temperatures considerably below their melting points and this can have several advantages:-

- (a) It may be possible to grow the low temperature polymorphs of  $Nb_2O_5$  under conditions of thermodynamic stability.
- (b) The temperatures required for chemical transport reactions are well within the capabilities of conventional resistance furnaces.
- (c) There are no serious problems concerning the containment of the crystals, since at the growth temperatures they are relatively inert.
- (d) The low growth temperature compared to the melting point results in lower concentrations of thermally induced defects.

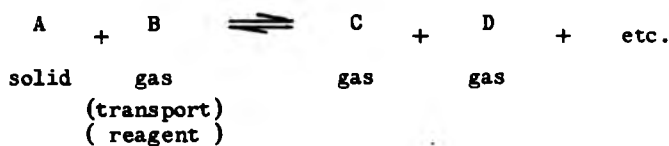


(e) Crystals grown from the vapour generally exhibit faceting and the morphology of the crystals provides a great deal of information about the growth mechanisms which are operating. \*

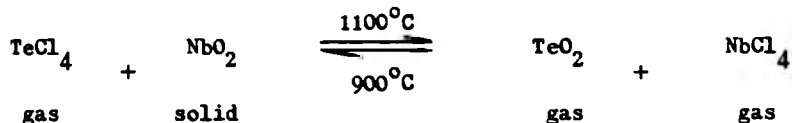
#### 2.4 The Chemical Transport Method

In simple chemical transport reactions, a solid or liquid, A, reacts with a gas, B, to form volatile products. These products are transported by some means to a different part of the system, where the conditions are such that they undergo the reverse reaction, resulting in the deposition of solid, A, and the regeneration of the transport reagent, B.

This can be represented by an equation as follows:-



For example, the transport of niobium dioxide by tellurium tetrachloride has been described by the equation:-



In fact this equation is a simplified representation of the reaction and several other volatile compounds such as niobium oxychloride ( $\text{NbOCl}_3$ ) can occur during the process.

In certain cases, the reaction which takes place is not strictly reversible. For example,  $\text{Nb}_{12}\text{O}_{29}$  crystals have been grown using  $\text{NbO}_2$  powder as the starting material. This type of reaction is best described in two parts.

\* See note overleaf

Note:

The information which can be obtained by morphological studies can be conveniently categorised as

- (a) equilibrium effects
- (b) non-equilibrium effects

Equilibrium features

Under favourable conditions single crystals will develop in such a way that the total energy is minimised. Because certain crystal faces have relatively low energies, at equilibrium, facets will form. The equilibrium shape of the crystals can be determined by plotting surface energy as a function of orientation (22) (Wulff plot).

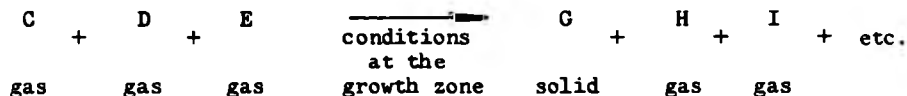
Non-equilibrium features

Crystal growth is a non-equilibrium process and invariably requires the presence of surface imperfections. The growth process can therefore be related to the types of crystal imperfections which can be observed. This will be discussed further in Chapter 4.

Firstly, consider the reaction of the starting material with the transport reagent to form a series of volatile products:-



These products will then be transported, possibly at different rates, to the growth zone. Under the prevailing conditions at the growth zone, the volatile compounds react to form a different solid phase which is deposited as crystals.



Strictly, reactions of this type do not conform to the accepted definition of chemical transport (Schafer (13)) since

- (a) there is a net change in the overall composition of the volatile intermediate compounds during this reaction
- (b) the reaction is not reversible.

Reactions of this type will be referred to as non-ideal chemical transport processes.

For an effective chemical transport process, certain criteria must be satisfied:-

- (a) All the reactants and products must be present in not insignificant quantities under the reaction conditions. This requires the existence of a "quasi-equilibrium" state.
- (b) The conditions of equilibrium must be different at the source and growth zones. Normally this requires that  $K$ , the equilibrium constant, must be a function of temperature.

Obviously when deciding the growth conditions required, factors such as the optimum growth rate and the degree of perfection of the final crystals must be considered. The temperature, temperature gradient, transport reagent and its concentration will all influence the growth kinetics.

2.5 Choice of Transport Reagent

Several chemical compounds have proved to be useful transport reagents for the preparation of transition metal oxides. Most of them rely on the generation of volatile transition metal halides or oxyhalides.

Some of the more common reagents are listed in Table 2.1 with an equation to indicate the possible reaction which could be utilised as the basis of a crystal growth technique for NbO<sub>2</sub>.

Table 2.1

Transport Reagent	Possible reaction with NbO <sub>2</sub>
I <sub>2</sub>	$\text{NbO}_2 + \text{I} + \text{NbI}_5 \rightleftharpoons 2\text{NbOI}_3$
HCl	$\text{NbO}_2 + 4\text{HCl} \rightleftharpoons \text{NbCl}_4 + 2\text{H}_2\text{O}$
Cl <sub>2</sub>	$4\text{NbO}_2 + 7\text{Cl}_2 \rightleftharpoons 2\text{NbCl}_4 + 2\text{NbOCl}_3 + 3\text{O}_2$
SOCl <sub>2</sub>	$\text{NbO}_2 + 2\text{SOCl}_2 \rightleftharpoons \text{NbCl}_4 + 2\text{SO}_2$
TeBr <sub>4</sub>	$\text{NbO}_2 + \text{TeBr}_4 \rightleftharpoons \text{NbBr}_4 + \text{TeO}_2$
TeCl <sub>4</sub>	$\text{NbO}_2 + \text{TeCl}_4 \rightleftharpoons \text{NbCl}_4 + \text{TeO}_2$
NH <sub>4</sub> Br	$\text{NbO}_2 + 4\text{NH}_4\text{Br} \rightleftharpoons \text{NbBr}_4 + 4\text{NH}_3 + 2\text{H}_2\text{O}$

In some chemical transport reaction systems, where sufficient thermodynamic data is available, it is possible to predict which reaction would be the most efficient. However, such data is not available for the reactions described here and the relative efficiencies of the various transport reagents can only be determined empirically.

The available experimental evidence suggests that for crystals of  $NbO_2$  and  $Nb_{12}O_{29}$ , reasonable growth rates can be achieved using  $TeCl_4$  (15),  $TeBr_4$  or  $NH_4Br$  (16). On the basis of this evidence preliminary experiments were carried out using  $TeCl_4$  as the transport reagent.

#### 2.6 Starting Materials

Historically, the chemical transport type of reaction has been used in the refinement of chemical compounds. This indicates that the purity of the starting materials may not be important. However despite this, the most chemically pure materials available were used.

Table 2.2

Compound	Purity	Source
$Nb_2O_5$ (powder)	99.999%	BDH "Optran Grade"
Nb (powder)	99.9%	Koch Light
$TeCl_4$ (powder)	99.0%	BDH Chemicals Ltd.

There is evidence that the stability of the various polymorphic forms of  $Nb_2O_5$  can be influenced by the presence of impurities. For example it has been reported that N- $Nb_2O_5$  is favoured in the presence of trace levels of fluorine (14).

Niobium dioxide ( $\text{NbO}_2$ ) powder was prepared from some of the  $\text{Nb}_2\text{O}_5$  by reduction at  $900^\circ\text{C}$  in a hydrogen atmosphere for six hours.

In order to study the variation in composition of the starting material on the resulting crystals, it was necessary to prepare powdered oxides with a range of compositions.

Powders of various compositions can readily be prepared by mixing together appropriate quantities of  $\text{Nb}_2\text{O}_5$ ,  $\text{NbO}_2$  or Nb powders. To ensure the starting materials were homogeneous, the powders were mixed thoroughly, sealed in an evacuated silica tube, and held at  $1000^\circ\text{C}$  for 100 hours. Under these conditions, oxygen exchange can take place, and the resulting powders have uniform composition.

The compositions of the starting powders were checked gravimetrically by heating a carefully weighed quantity in air until it had been completely oxidised. Assuming that the oxidised product is  $\text{Nb}_2\text{O}_5$ , the weight gained during oxidation enables the composition of the starting material to be calculated.

## 2.7 Crystal Growth Apparatus

In all the chemical transport experiments, silica reaction tubes were used. These tubes were approximately 20 cm long and 18-20 mm inside diameter (Fig. 2.1). Silica has adequate mechanical strength at high temperatures, is chemically inert, and has extremely good thermal shock resistance. The use of silica however restricts the operating temperatures to below about  $1100^\circ\text{C}$  since above this temperature softening occurs.

Crystal growth by chemical transport depends on the condition of chemical equilibrium being different in the growth zone and in the source zone. This criterion can be satisfied by, for example, differences in

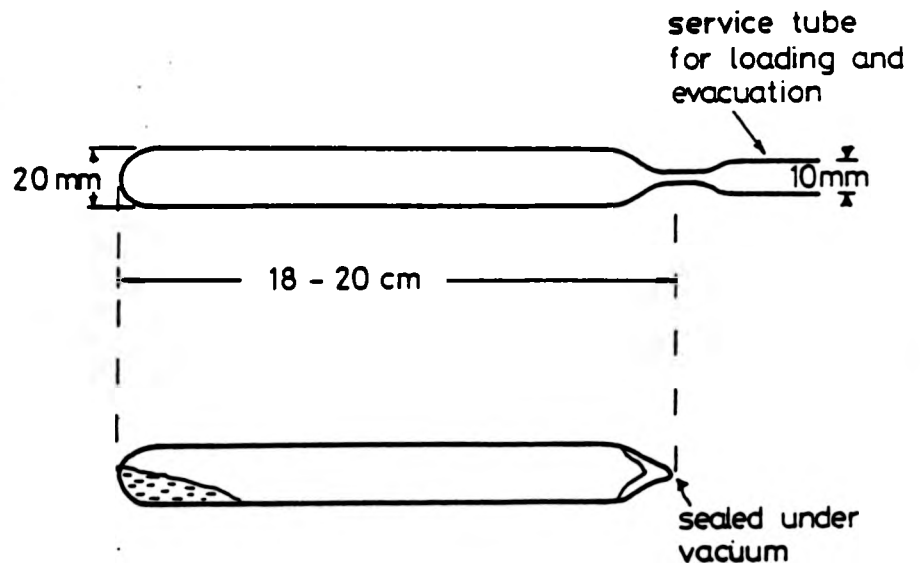


Fig. 2.1. The silica reaction tubes used for chemical transport.

pressure or temperature in the two regions. Normally, chemical transport techniques rely on the temperature dependence of the equilibrium constant for the reaction and are carried out by arranging for a temperature gradient to exist between the source and growth zones.

To enable a variety of different crystals to be grown, a versatile furnace was designed with two independently controlled windings. With this arrangement it was possible to select a wide range of temperatures and temperature gradients according to the conditions required for the growth of each particular crystal species.

Schafer (13), suggested the use of furnaces with long isothermal zones in the source and growth regions, separated by a short steep temperature gradient (Fig. 2.2(a)). This arrangement reduces the influence of temperature gradients on the growth of the crystals. However, if a more gradual temperature gradient is used, it is possible to study the variations of growth rate and composition with position in the furnace. Information concerning the temperature range of stability of a phase can be obtained in this way. In addition, where two phases grow simultaneously under similar conditions, a temperature gradient in the growth zone may facilitate their separation. In fact, this spatial separation of similar phases proved to be useful in the case of the polymorphic forms of  $\text{Nb}_2\text{O}_5$  under particular conditions. Temperature profiles for the furnace were measured for each set of operating conditions using a Pt/Pt-10% Rh thermocouple. A typical temperature profile is depicted in Fig. 2.2(b).

A schematic diagram of the furnace is shown in Fig. 2.3. The furnace was constructed using nichrome windings on a recrystallised alumina tube of approximately 5 cm diameter. This was housed in a Sindanio case, packed with vermiculite granules for thermal insulation. The power supplies



Fig. 2.2

The temperature gradient used for chemical  
transport

The temperature profile shown in Fig. 2.2 (a) has isothermal source and growth zones separated by a short region with a steep temperature gradient. Schafer has suggested that, with suitable choice of source and growth temperatures, such a profile should be the most efficient.

However, temperature profiles similar to that shown in Fig. 2.2 (b) can be readily obtained without resort to sophisticated furnace design. In this work such profiles proved to be adequate for all the crystal growth experiments and in some cases where more than one species was grown simultaneously, the range of temperature at the growth zone generally resulted in the spatial separation of the different crystals.

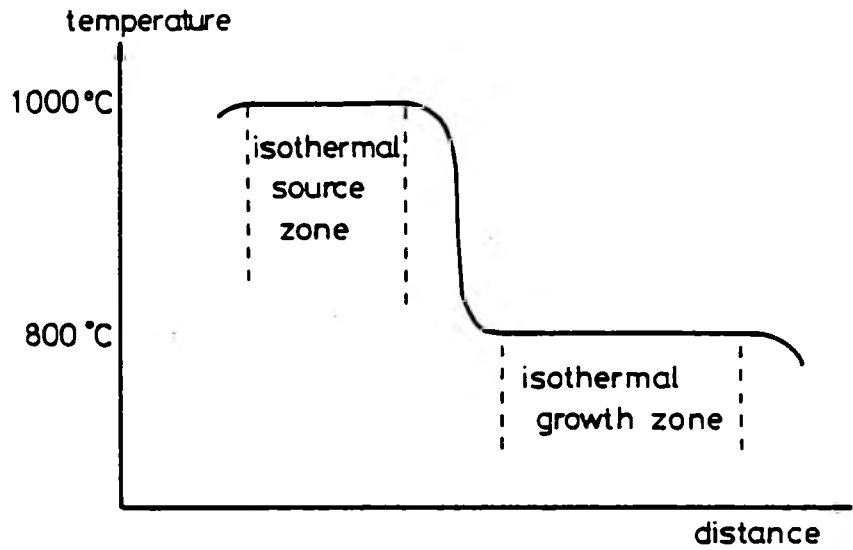


Fig. 2.2a. Temperature profile recommended by Schafer (13).

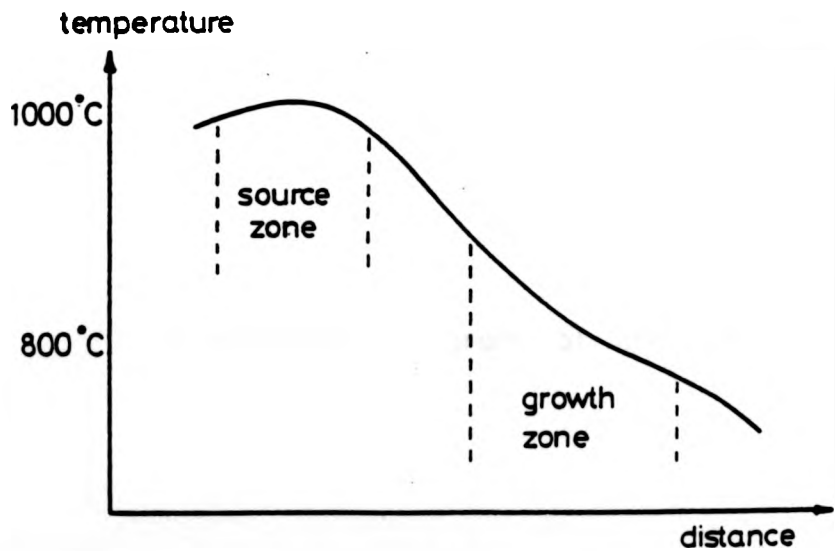


Fig. 2.2b. A typical temperature profile used in this work.

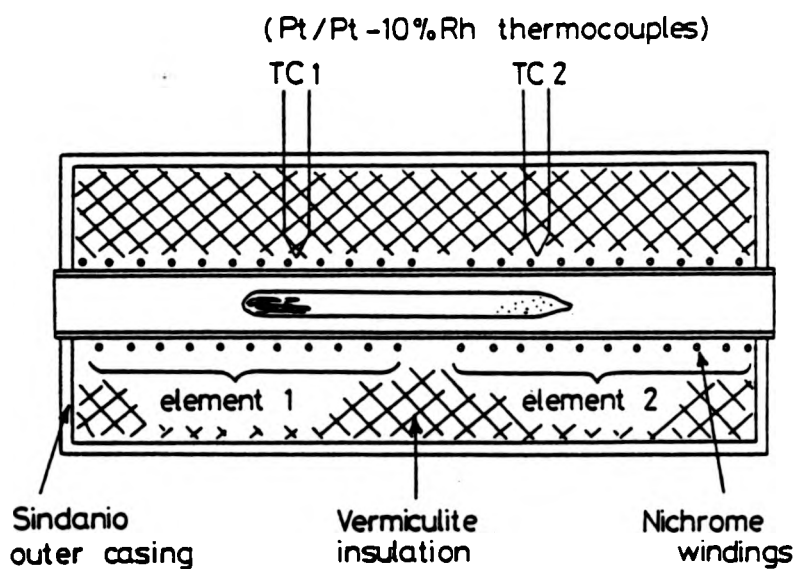


Fig. 2.3. A schematic diagram of the furnace.

for the two elements were regulated using "Ether" stepless temperature controllers. The furnace operated satisfactorily at temperatures below 1100°C.

Note: At the operating temperature, the pressure in the silica tube can rise to several atmospheres and because of the toxic and corrosive nature of  $\text{TeCl}_4$  vapour, the furnace was kept permanently in a fume cupboard.

## 2.8 Experimental Details

### 2.8.1 Preparing and loading the reaction tube

Silica reaction tubes were prepared as shown in Fig. 2.1. The length of 10 mm diameter tube was used for loading and for the evacuation procedure.

During crystal growth, nucleation takes place at surface imperfections on the walls of the reaction ampoules. If large crystals are required, the number of such nucleation sites must be minimised and various elaborate techniques have been evolved to wash and etch the walls of the silica tube (17). Experimentally, however, it was found that crystals of sufficient size could be obtained without resorting to such an involved treatment of the reaction vessel. The tubes were, however, carefully washed to remove any impurities.

A charge of approximately 2 gm of powder of the desired starting composition was introduced into one of the clean dry silica tubes. Since water, adsorbed by the powder or on the walls of the silica tube is known to have an effect on some chemical transport reactions (18), the partially loaded tubes were degassed by holding them at 500°C for 4 hours under vacuum.

After cooling the tubes, the tellurium tetrachloride ( $\text{TeCl}_4$ ) transport reagent was introduced. Due to the volatile, hygroscopic nature

of this compound, this procedure was carried out in a dessicated glove box. To minimise the possible introduction of metallic impurities, specially made silica spatulas were used.

The loaded tube was removed from the glove box and connected to a vacuum pump as quickly as possible. The vacuum pump exhaust was vented to the outside to eliminate the risks associated with the volatile  $\text{TeCl}_4$ . When the tube had been pumped to a pressure of about  $5 \times 10^{-5}$  torr it was sealed off using a gas/oxygen torch.

Note: The weight of  $\text{TeCl}_4$  in the tube could be found by first weighing the tube, charged with the oxide powder after the degassing stage and then reweighing the sealed tube along with the silica service tube.

#### 2.8.2 Crystal growth.

With the exception of  $\text{NbO}$ , all the crystals prepared by this technique involved transport from a hotter "source" zone to a cooler "growth" zone.  $\text{NbO}$  was found to be transported in the opposite direction.

The required temperature gradient for the furnace was set and checked before the loaded silica tube was introduced. Initially the tube was placed in the furnace with the charge of oxide powder in the low temperature zone. In this position any powder which was attached to the walls at the opposite end to the charge would be transported by the action of the  $\text{TeCl}_4$  and redeposited with the main charge. In this way the growth region of the tube was cleared of many potential nuclei.

After 4 or 5 hours, the silica tube was carefully repositioned for normal crystal growth. The exact position of the tube in the furnace was noted so that the temperature at any point in the tube could be established from the temperature profile measurements.

The niobium oxide was transported by the  $\text{TeCl}_4$  and redeposited in the cooler part of the tube as small single crystals. In some cases more than one species of crystal grew, and because of temperature and composition gradients in the reaction tube, the different types grew in different parts of the growth zone.

The typical duration of a crystal growth experiment was about one hundred hours, depending on the rate of transport which was achieved. In the case of  $\text{Nb}_2\text{O}_5$  crystals for example, the transport rate was much higher and consequently shorter times could be used.

To avoid excessive contamination of the single crystals by the volatile reactants, the silica tube was removed from the furnace so that the source end cooled first. The cooling was further accelerated by quenching this end of the tube in water. This procedure ensures that most of the  $\text{TeCl}_4$  and other volatiles condense at the opposite end of the tube from the crystals.

Fig. 2.4 shows a reaction tube after successful chemical transport.

When cold, the silica tubes were carefully broken open and the crystals removed. The crystals were then washed in hot dilute hydrochloric acid to remove any remaining  $\text{TeCl}_4$ . After careful washing and drying, the crystals were weighed to estimate the yield and transport rate.

## 2.9 Identification of the Crystals

It was relatively simple to distinguish between the various crystal species by inspection since they differ in morphology and in some cases colour. Generally the different crystal types were identified by X-ray powder diffraction. Samples were prepared by grinding a few of the crystals to a fine powder using an agate pestle and mortar. The X-ray

The niobium oxide was transported by the  $\text{TeCl}_4$  and redeposited in the cooler part of the tube as small single crystals. In some cases more than one species of crystal grew, and because of temperature and composition gradients in the reaction tube, the different types grew in different parts of the growth zone.

The typical duration of a crystal growth experiment was about one hundred hours, depending on the rate of transport which was achieved. In the case of  $\text{Nb}_2\text{O}_5$  crystals for example, the transport rate was much higher and consequently shorter times could be used.

To avoid excessive contamination of the single crystals by the volatile reactants, the silica tube was removed from the furnace so that the source end cooled first. The cooling was further accelerated by quenching this end of the tube in water. This procedure ensures that most of the  $\text{TeCl}_4$  and other volatiles condense at the opposite end of the tube from the crystals.

Fig. 2.4 shows a reaction tube after successful chemical transport.

When cold, the silica tubes were carefully broken open and the crystals removed. The crystals were then washed in hot dilute hydrochloric acid to remove any remaining  $\text{TeCl}_4$ . After careful washing and drying, the crystals were weighed to estimate the yield and transport rate.

## 2.9 Identification of the Crystals

It was relatively simple to distinguish between the various crystal species by inspection since they differ in morphology and in some cases colour. Generally the different crystal types were identified by X-ray powder diffraction. Samples were prepared by grinding a few of the crystals to a fine powder using an agate pestle and mortar. The X-ray



Figure 2.4 The reaction tube after a typical growth experiment. The fine needle shaped crystals are  $\text{H-Nb}_2\text{O}_5$

---

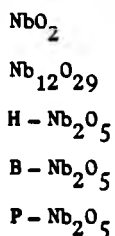


powder patterns were obtained using a Debye-Scherer powder camera and  $\text{Cu K}\alpha$  radiation. Fluorescence due to niobium caused fogging of the film but by choosing suitable exposure times it was possible to detect the Bragg reflected X-ray lines. Normally the crystals could be identified by comparing the measured d-spacings with the published X-ray data for the niobium oxides (14, 19, 20).

The structural similarities between some of the higher oxides resulted in some difficulty in identifying these oxides by X-ray diffraction unambiguously. In these cases an unambiguous identification could be made using the transmission electron microscope to obtain direct lattice images and "single crystal" electron diffraction patterns.

#### 2.10 Results

By varying the composition of the starting material, and the temperature of the growth zone, the following crystal phases were grown.



Crystals of NbO were also prepared by chemical transport in the reverse direction.

Table 2.3 summarises the results of some of the crystal growth experiments and gives the highest transport rates which were obtained in each case and the corresponding growth conditions. The growth rates and crystal sizes obtained compared favourably with the reported results of other workers using different transport reagents. For example Kodama and Goto (16) obtained crystals of  $\text{Nb}_{12}\text{O}_{29}$  and  $\text{NbO}_2$  with maximum dimensions

Table 2.3

Starting Composition	Temp. of Source Zone °C	Temp. of Growth zone °C	Conc. of TeCl <sub>4</sub>	Transport Rate	Crystals Obtained	Maximum Size Obtained	Description of Crystals
1. NbO	740 - 780	880 - 890	8.1 mg/ml	8 mg/hr	NbO	0.25 mm <sup>3</sup>	Crystals grow as a crust of small equiaxed polyhedra with a metallic lustre
2. NbO	1020 - 1030	860 - 920	10.0 mg/ml	7 mg/hr	NbO <sub>2</sub>	8 mm x 3 mm x 2 mm	Blue/black elongated crystals - often twinned
3. NbO	1000 - 1015	870	40.0 mg/ml	6.4 mg/hr	NbO <sub>2</sub> + NbTe <sub>2</sub>	7 mm x 2.5 x 0.3	Hexagonal plates with metallic lustre
4. NbO <sub>2</sub>	1100 - 1120	780 - 880 820 - 900	14.0 mg/ml	12 mg/hr	Nb <sub>12</sub> O <sub>29</sub> (Orth) NbO <sub>2</sub>	2 mm x 2 mm x 1 mm 1 mm <sup>3</sup>	Mainly elongated plates and needles (blue/black) Small blue/black octahedra
5. NbO <sub>2</sub>	1020 - 1030	850 - 900	15.9 mg/ml	10 mg/hr	Nb <sub>12</sub> O <sub>29</sub>	12 mm x 6 mm x 1 mm	Large blue/black plates, often twinned
6. Nb <sub>2</sub> O <sub>5</sub>	1030 - 1050	860 - 890	5.0 mg/ml	~ 80 mg/hr	H-Nb <sub>2</sub> O <sub>5</sub>	10 mm x 0.1 mm x 0.1 mm	White needle shaped crystals
7. Nb <sub>2</sub> O <sub>5</sub>	860 - 890	750 - 775	5.0 mg/ml	~ 80 mg/hr	B-Nb <sub>2</sub> O <sub>5</sub>	8 mm x 5 mm x 1 mm	Transparent yellow platelike crystals
8. Nb <sub>2</sub> O <sub>5</sub>	640	550 - 570 530 - 570	5.0 mg/ml	~ 80 mg/hr	B-Nb <sub>2</sub> O <sub>5</sub> F-Nb <sub>2</sub> O <sub>5</sub>	3 mm x 3 mm x 1 mm ≈ 1 mm	Brown/yellow semi-transparent crystals Crystals grow as a crust of yellow polyhedra

Table 2.3

Starting Composition	Temp. of Source Zone °C	Temp. of Growth zone °C	Conc. of TeCl <sub>4</sub>	Transport Rate	Crystals Obtained	Maximum Size Obtained	Description of Crystals
1. NbO	740 - 780	880 - 890	8.1 mg/ml	8 mg/hr	NbO	0.25mm <sup>3</sup>	Crystals grow as a crust of small equiaxed polyhedra with a metallic lustre
2. NbO	1020 - 1030	860 - 920	10.0 mg/ml	7 mg/hr	NbO <sub>2</sub>	8mm x 3mm x 2mm	Blue/black elongated crystals - often twinned
3. NbO	1000 - 1015	870	40.0 mg/ml	6.4 mg/hr	NbO <sub>2</sub> + NbTe <sub>2</sub>	7mm x 2.5 x 0.3	Hexagonal plates with metallic lustre
4. NbO <sub>2</sub>	1100 - 1120	780 - 880 820 - 900	14.0 mg/ml	12 mg/hr	Nb <sub>12</sub> O <sub>29</sub> (Orth) NbO <sub>2</sub>	2mm x 2mm x 1mm 1mm <sup>3</sup>	Mainly elongated plates and needles (blue/black) Small blue/black octahedra
5. NbO <sub>2</sub>	1020 - 1030	850 - 900	15.9 mg/ml	10mg/hr	Nb <sub>12</sub> O <sub>29</sub>	12mm x 6mm x 1mm	Large blue/black plates, often twinned
6. Nb <sub>2</sub> O <sub>5</sub>	1030 - 1050	860 - 890	5.0 mg/ml	70-80 mg/hr	H-Nb <sub>2</sub> O <sub>5</sub>	10mm x 0.1mm x 0.1mm	White needle shaped crystals
7. Nb <sub>2</sub> O <sub>5</sub>	860 - 890	750 - 775	5.0 mg/ml	80 mg/hr	B-Nb <sub>2</sub> O <sub>5</sub>	8mm x 5mm x 1mm	Transparent yellow platelike crystals
8. Nb <sub>2</sub> O <sub>5</sub>	640	550 - 570 530 - 570	5.0 mg/ml	80 mg/hr	B-Nb <sub>2</sub> O <sub>5</sub> F-Nb <sub>2</sub> O <sub>5</sub>	3mm x 3mm x 1mm ≈ 1mm	Brown/yellow semi-transparent crystals Crystals grow as a crust of yellow polyhedra

of up to 5 mm. Transport rates achieved in their experiments were about 4 mg/hr using  $\text{TeBr}_4$  as transport reagent and up to 11 mg/hr using  $\text{NH}_4\text{Br}$ .

The experiments have shown that increasing the concentration of the transport reagent appears to increase the transport rate. However, there is a concomitant increase in the pressure in the reaction tube and Nagasawa (21) has reported that during the transport of vanadium oxides by  $\text{TeCl}_4$ , the pressure can cause explosion of the silica tube. The silica tubes used in this work proved to be sufficiently robust to withstand the pressure generated by up to 40 mg/ml of  $\text{TeCl}_4$  at about  $900^\circ\text{C}$  without failure.

Although increasing the concentration of  $\text{TeCl}_4$  usually resulted in an increased growth rate, this was usually accompanied by a reduction in crystal quality. Also rapid transport often gave rise to a higher rate of nucleation and did not necessarily result in larger crystals.

Another consequence of high levels of  $\text{TeCl}_4$  in the reaction tube is indicated by reaction 3 (Table 2.3). The excess tellurium in the reaction system gives rise to the formation of niobium ditelluride crystals  $\text{NbTe}_2$ , as well as the niobium dioxide crystals.

In experiments to establish the relationship between the product crystals and the starting materials, the niobium/oxygen ratio was found to be invariably higher in the starting material than in the growth products. Thus for a starting material with a composition between  $\text{NbO}$  and  $\text{NbO}_2$ , crystals of  $\text{NbO}_2$  and  $\text{Nb}_{12}\text{O}_{29}$  formed; the proportion of  $\text{Nb}_{12}\text{O}_{29}$  crystals being higher as the Nb/O ratio of the starting material was reduced. Similarly for starting compositions between  $\text{NbO}_2$  and  $\text{Nb}_{12}\text{O}_{29}$ , the greater proportion of

of up to 5 mm. Transport rates achieved in their experiments were about 4 mg/hr using  $\text{TeBr}_4$  as transport reagent and up to 11 mg/hr using  $\text{NH}_4\text{Br}$ .

The experiments have shown that increasing the concentration of the transport reagent appears to increase the transport rate. However, there is a concomitant increase in the pressure in the reaction tube and Nagasawa (21) has reported that during the transport of vanadium oxides by  $\text{TeCl}_4$ , the pressure can cause explosion of the silica tube. The silica tubes used in this work proved to be sufficiently robust to withstand the pressure generated by up to 40 mg/ml of  $\text{TeCl}_4$  at about  $900^\circ\text{C}$  without failure.

Although increasing the concentration of  $\text{TeCl}_4$  usually resulted in an increased growth rate, this was usually accompanied by a reduction in crystal quality. Also rapid transport often gave rise to a higher rate of nucleation and did not necessarily result in larger crystals.

Another consequence of high levels of  $\text{TeCl}_4$  in the reaction tube is indicated by reaction 3 (Table 2.3). The excess tellurium in the reaction system gives rise to the formation of niobium ditelluride crystals  $\text{NbTe}_2$ , as well as the niobium dioxide crystals.

In experiments to establish the relationship between the product crystals and the starting materials, the niobium/oxygen ratio was found to be invariably higher in the starting material than in the growth products. Thus for a starting material with a composition between  $\text{NbO}$  and  $\text{NbO}_2$ , crystals of  $\text{NbO}_2$  and  $\text{Nb}_{12}\text{O}_{29}$  formed; the proportion of  $\text{Nb}_{12}\text{O}_{29}$  crystals being higher as the Nb/O ratio of the starting material was reduced. Similarly for starting compositions between  $\text{NbO}_2$  and  $\text{Nb}_{12}\text{O}_{29}$ , the greater proportion of

the crystals was  $Nb_{12}O_{29}$ , with some  $NbO_2$  crystals for starting compositions close to  $NbO_2$ . In an experiment using a starting powder with a composition corresponding to  $Nb_{12}O_{29}$ , X-ray diffraction data indicated the presence of higher oxides in addition to  $Nb_{12}O_{29}$ . Further evidence confirming the presence of these higher oxide intergrowths was obtained by high resolution electron microscopy and will be presented in Chapter 5.

In cases where oxides of different composition grew simultaneously, the higher oxide was always deposited in the coolest part of the growth zone.

The implications of these results will be discussed in detail in the next chapter.

REFERENCES

1. T.B. Reed, Materials Res. Bull., 2, 349-367, (1967).
2. T.B. Reed and E.R. Pollard, J. Cryst. Growth, 2, 243-247, (1967).
3. W. Precht and G.E. Hollox, J. Cryst. Growth, 3, 818, (1968).
4. P.S. Bell, Ph.D. Thesis, University of Warwick, (1972).
5. R.W. Bartlett, F.A. Halden and J.W. Fowler, Rev. Sci. Instr., 38, 291, (1967).
6. L.R. Fleischer and J.M. Tobin, J. Cryst. Growth, 8, 235, (1971); 8, 243, (1971).
7. H. Schafer, in "Crystal Growth: An Introduction", (ed. P. Hartman), North Holland, Amsterdam, (1973).
8. J.S. Sheasby and B. Cox, J. Less Common Metals, 15, 129, (1968).
9. J.S. Sheasby, W.W. Smeltzer and A.E. Jenkins, J. Electrochem. Soc., 115, 338, (1968).
10. I. Shindo and H. Komatsu, J. Cryst. Growth, 34, 152-153, (1976).
11. K. Nassau and A.M. Broyer, J. Am. Ceram. Soc., 45, 474-478, (1962).
12. H. Sasaki and Watanabe, J. Phys. Soc. Japan, 19, 1748, (1964).
13. H. Schafer, "Chemical Transport Reactions", Academic Press, New York, (1964), Trans. H. Frankfurt.
14. H. Schafer, R. Gruehn and F. Schulte, Angew. Chem. Internat. Ed., 5, 40, (1966).
15. T. Sakata, K. Sakata, G. Hofer, T. Horiuchi, J. Cryst. Growth, 12, 88, (1972).
16. H. Kodama and M. Goto, J. Cryst. Growth, 29, 77-79 (1975), 29, 222-224, (1975).
17. M.C. DeLong, AD-760 733, Utah Univ. Salt Lake City, Dept. of Physics, (1973).
18. P. Peshev, G. Bliznakov, G. Gyurov and M. Ivanova, Mat. Res. Bull., 8, 915, (1973).

REFERENCES

1. T.B. Reed, Materials Res. Bull., 2, 349-367, (1967).
2. T.B. Reed and E.R. Pollard, J. Cryst. Growth, 2, 243-247, (1967).
3. W. Precht and G.E. Hollox, J. Cryst. Growth, 3, 818, (1968).
4. P.S. Bell, Ph.D. Thesis, University of Warwick, (1972).
5. R.W. Bartlett, F.A. Halden and J.W. Fowler, Rev. Sci. Instr., 38, 291, (1967).
6. L.R. Fleischer and J.M. Tobin, J. Cryst. Growth, 8, 235, (1971); 8, 243, (1971).
7. H. Schafer, in "Crystal Growth: An Introduction", (ed. P. Hartman), North Holland, Amsterdam, (1973).
8. J.S. Sheasby and B. Cox, J. Less Common Metals, 15, 129, (1968).
9. J.S. Sheasby, W.W. Smeltzer and A.E. Jenkins, J. Electrochem. Soc., 115, 338, (1968).
10. I. Shindo and H. Komatsu, J. Cryst. Growth, 34, 152-153, (1976).
11. K. Nassau and A.M. Broyer, J. Am. Ceram. Soc., 45, 474-478, (1962).
12. H. Sasaki and Watanabe, J. Phys. Soc. Japan, 19, 1748, (1964).
13. H. Schafer, "Chemical Transport Reactions", Academic Press, New York, (1964), Trans. H. Frankfurt.
14. H. Schafer, R. Gruehn and F. Schulte, Angew. Chem. Internat. Ed., 5, 40, (1966).
15. T. Sakata, K. Sakata, G. Hofer, T. Horiuchi, J. Cryst. Growth, 12, 88, (1972).
16. H. Kodama and M. Goto, J. Cryst. Growth, 29, 77-79 (1975), 29, 222-224, (1975).
17. M.C. DeLong, AD-760 733, Utah Univ. Salt Lake City, Dept. of Physics, (1973).
18. P. Peschev, G. Bliznakov, G. Gyurov and M. Ivanova, Mat. Res. Bull., 8, 915, (1973).



19. A.S.T.M. Inorganic Index to the Powder Diffraction File, (1969).
20. N. Terao, Japan. J. Appl. Phys., 2, 156 - 174, (1963).
21. K. Nagasawa, Bando and Takada, J. Cryst. Growth, 17, 143 - 148, (1972).
22. J.M. Blakely. "An Introduction to the Properties of Crystal Surfaces", Pergamon, 1973.

### CHAPTER THREE

#### THE THERMODYNAMICS AND KINETICS OF THE CHEMICAL TRANSPORT PROCESS

##### 3.1 Introduction

It has already been pointed out that crystal growth by chemical transport depends on the existence of a reaction with a suitable transport reagent and this chemical reaction must be such that the source material is consumed in one region of the reaction vessel and the required crystals are deposited in another region.

The rate and the direction of transport will depend on the chemical equilibrium conditions which exist in the two reaction zones and on the mechanisms of mass transport which are operating.

In this chapter, the chemistry of the transport reactions is discussed in detail and the main factors which control the transport rate are deduced from the results of the crystal growth programme. In addition the conditions of thermodynamic stability of the various crystal phases are considered with particular reference to the experiments in which more than one crystal species were grown.

##### 3.2 The Chemistry of the Transport Reactions

In practice, the precise details of the vapour phase reactions which occur during chemical transport are difficult to establish. In some cases however it was possible to identify some of the final reaction products and this was carried out in the following way. After some of the crystal growth experiments, the reaction tubes were quenched so as to condense some of the volatile phases present. Some of these condensed residues could be

identified by X-ray diffraction. The information obtained in this way is summarised in Table 3.1. The X-ray powder diffraction method was also used to check the chemical state of the unused starting material. In general, where the starting material was of a composition corresponding to a single phase oxide, (e.g.  $\text{NbO}_2$ ) it remained unchanged during the reaction.

Although only a few of the final reaction products could be positively identified in this way it is likely that during chemical transport a number of different volatile species were present to a greater or lesser extent. It is this variety of intermediate volatile compounds which is probably responsible for the versatility of this method of crystal growth. Variations in the composition of the starting material and concentration of  $\text{TeCl}_4$  simply result in changes in the proportions of the various volatile species and this in turn enables crystals of various compositions to be grown. However, the complicated nature of the chemistry of these systems renders the quantitative prediction of transport rates difficult.

### 3.3 Non-ideal Chemical Transport Reactions

According to Schafer (1) a chemical transport process involves a reversible reaction in which a solid source material reacts with a volatile transport reagent to form a number of volatile products. These volatile products are transported to a different part of the system where the conditions are such that the reverse reaction occurs and the solid phase is regenerated, usually in the form of single crystals. However in the niobium-oxygen system, there are cases for which the compositions of the reacting source material and the crystals produced are different. For example, it was pointed out in the previous chapter

that in the growth of  $Nb_{12}O_{29}$  crystals from a starting material of  $NbO_2$ , the chemical reactions involved are not reversible.

For the discussion of such cases, the concept of non-ideal chemical transport was introduced. The importance of such non-ideal processes in the growth of some of the niobium oxides requires a detailed treatment.

Consider first the progress of a general crystal growth experiment step by step:-

- (a) Initially, on introduction into the furnace, the transport reagent vaporises and fills the reaction tube. Dissociation of the vapour may also occur.
- (b) The transport reagent reacts with the material in the source zone to produce a mixture of volatile products. This reaction is normally regarded as being rapid compared to the rate at which the volatile products diffuse away and so a quasi-equilibrium situation exists. In this state, the composition of the gases at the source zone is almost the same as that which would be necessary for chemical equilibrium. The removal of the reaction products from the region by diffusion and other processes, causes a slight deviation from equilibrium and provides the driving force for the reaction.
- (c) The products of the source zone reaction diffuse along the silica tube and the composition of the gas at the growth zone gradually changes, becoming progressively richer in the transported elements.
- (d) Eventually the composition of the gases at the growth zone is such that it is chemically unstable and can react to form a stable solid phase. This state represents a condition of supersaturation.

(e) After the formation of suitable nuclei of this solid phase, the reaction proceeds until again a quasi-equilibrium situation is achieved. In this case, the composition of the gaseous phases above the crystalline solid is almost the same as the composition which would be necessary for chemical equilibrium. As the gas in this region is enriched by the products which are arriving from the source zone, the deviation from chemical equilibrium effectively increases the supersaturation. This results in further growth of the crystals and the composition of the vapour is restored to its equilibrium value.

Now in ideal chemical transport systems, the original transport reagent is regenerated at the growth zone, and the net result of the process is simply the transfer of material from the source zone to the growth zone. However, in the case of non-ideal chemical transport, the problem is more complicated. Since the compositions of the source material and the growing crystals are not the same, the transport process must inevitably result in a change of composition of the gaseous phase.

### 3.3.1 The growth of $Nb_{12}O_{29}$ crystals.

The case of  $Nb_{12}O_{29}$  has already been cited as an example of non-ideal chemical transport. In this section the consequences of the composition changes during crystal growth will be considered.

Crystals of  $Nb_{12}O_{29}$  are grown by chemical transport using  $NbO_2$  as the starting material. Since the growing crystals are richer in oxygen than the starting material, it follows that the volatiles must become progressively richer in niobium. These changes in composition may have the following effects:-

- (a) Transport occurs until the composition of the volatiles

reaches a point at which no further deposition of  $Nb_{12}O_{29}$  can occur. The transport reagent has gradually been modified and become "saturated" by niobium atoms, preventing any further reaction at the source zone.

(b) Transport may occur with the concomitant change in vapour composition until the growth of  $Nb_{12}O_{29}$  crystals is no longer the most favourable result. Since the transport reagent is gradually becoming more and more saturated with Nb, the conditions may become favourable for the growth of  $NbO_2$ . If this situation does arise,  $NbO_2$  will grow with no further change in the composition of the transporting gases. Hence in this case, the total yield of crystals would be independent of the initial concentration of transport reagent.

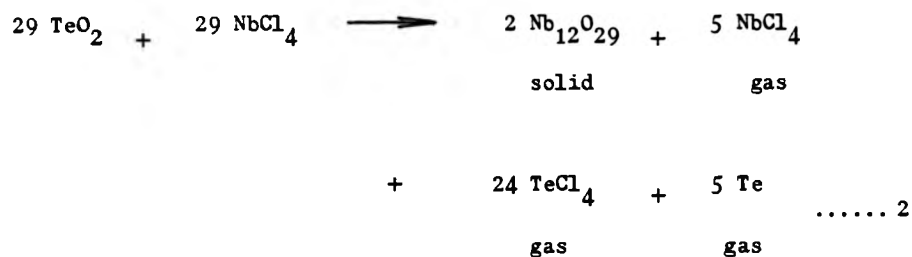
The experimental evidence given in Table 2.2 is consistent with either of these two cases. It is interesting to note that where only crystals of  $Nb_{12}O_{29}$  are produced the argument presented here suggests that the total yield will depend on the initial level of tellurium tetrachloride present. In fact by making some assumptions concerning the chemical reactions involved it is possible to predict the relationship between the total yield and the initial quantity of  $TeCl_4$  used in this reaction.

Assume that the reactions for the transport of  $Nb_{12}O_{29}$  can be expressed by the following equations:-

At the source zone:



and at the growth zone,



Combining equations 1 and 2, the reaction for the complete process may be written:-



In deriving these equations, assumptions have been made as to the chemical species which are present in the vapour phase. However some of these assumptions concerning the intermediate phases which form are of little consequence for this purpose and the major assumptions relate to the overall change in the vapour composition which is expressed in equation 3. Reference to Table 3.1 shows that significant quantities of tellurium vapour are present for most of the reactions observed, but no firm evidence is available to confirm the presence or absence of  $\text{NbCl}_4$ . Indeed it is likely that under the reaction conditions any  $\text{NbCl}_4$  which was present would be in a dissociated form.

However, based on the assumption that equation 3 provides a reasonable description of the overall reaction which takes place during crystal growth, it is possible to estimate the maximum possible yield of  $\text{Nb}_{12}\text{O}_{29}$  crystals as a function of the quantity of  $\text{TeCl}_4$  which was initially present.

Table 3.1

Reaction Products Generated During Chemical Transport

Compound	Description	Occurrence	Method of Identification
Tellurium (Te)	Small metallic globules	Generally observed	X-ray diffraction
TeO <sub>2</sub>	Grey/White condensate	Generally observed	X-ray diffraction
TeCl <sub>2</sub>	-	Frequently observed	X-ray diffraction
	Blue/Black powder	Frequently observed	Unidentified compound probably of Nb
	White powder	-	Unidentified



Referring to equation 3.

5 gm molecules of  $\text{TeCl}_4$  are consumed during the growth of 2 gm molecules of  $\text{Nb}_{12}\text{O}_{29}$  crystals.

i.e. 1 gm of  $\text{TeCl}_4$  is consumed during the growth of 2.35 gm of  $\text{Nb}_{12}\text{O}_{29}$ .

Thus the maximum yield, Y, of  $\text{Nb}_{12}\text{O}_{29}$  which can be expected from a chemical transport reaction of this form will be given by:-

$$Y = 2.35 M_{\text{TeCl}_4} \dots 4 \quad \text{where } M_{\text{TeCl}_4} \text{ is the original mass of } \text{TeCl}_4$$

It is important to realise that during the growth process, the partial pressure of active transport reagent is decreasing and so this limiting value of the total yield will be achieved asymptotically.

To test this relationship, a series of growth experiments was carried out using different starting quantities of  $\text{TeCl}_4$  and keeping everything else constant. Crystal growth was carried out for approximately one hundred hours in each case. The results of these experiments are shown in Fig. 3.1. In all cases, the yield of  $\text{Nb}_{12}\text{O}_{29}$  was never observed to exceed the upper limit predicted by equation 4.

### 3.3.2 The growth of $\text{NbO}_2$ crystals.

So far, the discussion of non-ideal chemical transport has been restricted to the example of  $\text{Nb}_{12}\text{O}_{29}$ . However, under certain conditions crystals of  $\text{NbO}_2$  can be prepared by a non-ideal process. Reference to Table 2.2 in chapter 2 shows that with  $\text{NbO}$  powder as the starting material and tellurium tetrachloride as the transport reagent, crystals of  $\text{NbO}_2$  can be produced.

Fig. 3.1

Comparison of the predicted maximum yield of  $Nb_{12}O_{29}$  crystals with the experimentally determined yields

The dotted line is the predicted variation of the yield of  $Nb_{12}O_{29}$  crystals as a function of the initial weight of  $TeCl_4$  as given by the equation

$$Y = 2.35 M_{TeCl_4} \dots (4)$$

The experimental results were obtained by performing a number of crystal growth experiments under carefully controlled conditions varying only the initial weight of  $TeCl_4$ .

As shown in the figure, all the experimentally determined yields fell below the maximum yield predicted by equation (4).

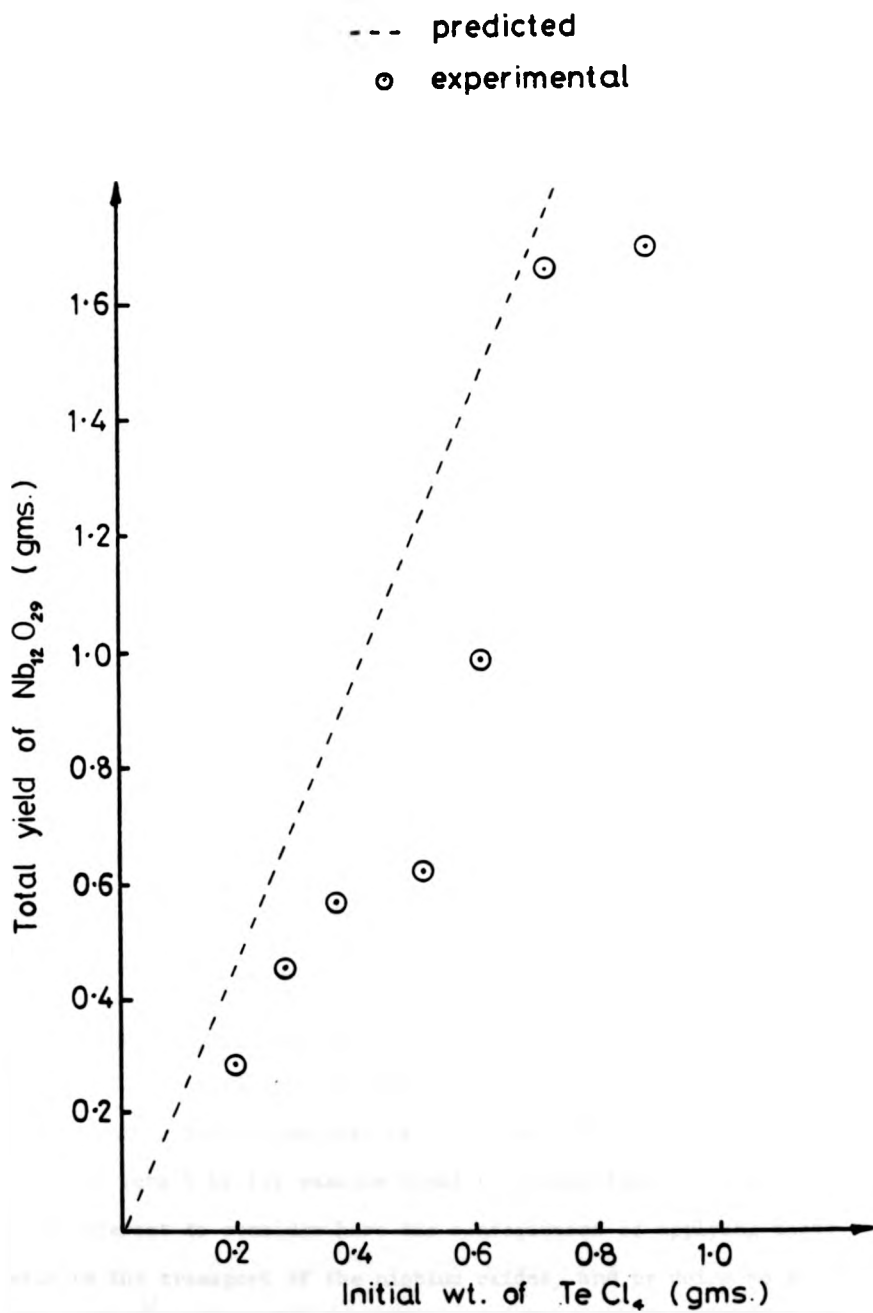


Fig. 3.1. The relationship between the total yield of  $\text{Nb}_{12}\text{O}_{29}$  crystals and the initial weight of  $\text{TeCl}_4$ .

Again, the detailed chemistry of this reaction is not well understood and the representation of the reaction by simple equations might be misleading. However, where no other solid phases occur in the reaction, the details of the intermediate volatile compounds can be eliminated by expressing the equation of the overall reaction as follows:-



Again, the transport reagent will be gradually modified during the growth of the crystals and the transporting properties will be gradually degraded as more and more of the active vapour phase becomes saturated by chemically combined niobium atoms. The inevitable result of this will be an upper limit on the yield of  $\text{NbO}_2$  crystals which can be expected by this process.

Further reference to Table 2.2 shows that as larger quantities of  $\text{TeCl}_4$  are used in this reaction, a point is reached at which niobium ditelluride ( $\text{NbTe}_2$ ) crystals are formed in addition to the  $\text{NbO}_2$  crystals. A further discussion of this phenomenon will be included in a separate section (3.6.2).

### 3.4 Thermodynamic Considerations and Chemical Equilibrium

For an efficient chemical transport reaction, certain chemical and thermodynamic conditions must be fulfilled. These conditions have been discussed at length by for example Schafer (2) and Faktor and Garrett (3). It is of interest to consider here the consequences of applying these criteria to the transport of the niobium oxides, and by doing so it is possible to make some deductions regarding the thermodynamics of the chemical reactions.

3.4.1 The equilibrium constant for efficient chemical transport.

Consider first the case of an ideal chemical transport reaction in which the transport reagent is regenerated as the crystals are deposited. The growth of the various polymorphs of  $Nb_2O_5$  and the growth of NbO crystals are examples of this type. When the loaded tube is introduced into the furnace, there is an initial transient period during which the transport reagent volatilises, possibly dissociates, and reacts with the source material. The products of this reaction then diffuse along the tube eventually leading to the nucleation and growth of crystals in the growth zone.

After a short time a quasi-equilibrium situation is established in both the source and growth regions of the reaction vessel.

In a general reaction of the type



the equilibrium constant K is given by:-

$$K = \frac{P_C \times P_D}{P_B} \quad \dots\dots 6 \quad \text{where } P_C, P_D, P_B \text{ are the partial pressures of the gases C, D and B}$$

It will be shown presently, that diffusive processes are the principal mechanisms by which gas exchange occurs within the reaction tube. Now the diffusion of a gas between two regions is proportional to the difference in partial pressures which exists. Thus for an efficient chemical transport reaction, significant differences in the partial pressures of the volatile species must exist between the two ends of the tube.

If K is very large, then from equation 6, the partial pressure of the transport reagent will be very low and consequently the concentration

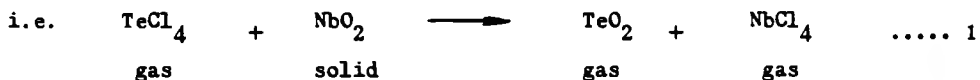
gradient will be small resulting in a slow transport rate. Similarly, if  $K$  is very small the partial pressures of the intermediate volatile compounds will be very low and again transport will be inhibited.

It seems, therefore, that chemical transport can only take place efficiently when  $K$  does not have an extreme value. Normally, the most efficient transport would be expected for a reaction with  $K \approx 1$ .

Since reasonably high transport rates are obtained for the growth of both  $Nb_2O_5$  and  $NbO$ , the chemical equilibrium constants for the reaction of these oxides with  $TeCl_4$  must have a value of the order of unity.

In the case of a non-ideal chemical transport reaction, the situation is somewhat more complicated. As an example, consider the reactions which result in the growth of  $Nb_{12}O_{29}$  crystals from  $NbO_2$  source material.

Assuming that the reaction at the source zone can be described as in equation 1.



The equilibrium constant for this reaction  $K_s$  can be written

$$K_s = \frac{P_{sTeO_2} \times P_{sNbCl_4}}{P_{sTeCl_4}} \dots\dots 7 \quad \text{where } P_s \text{ is the partial pressure of the particular species at the source zone.}$$

Now for a high transport rate, it is essential to have substantial quantities of the reaction products generated in the source zone. Consequently, one might expect the optimum value of  $K_s$  to be as high as possible.

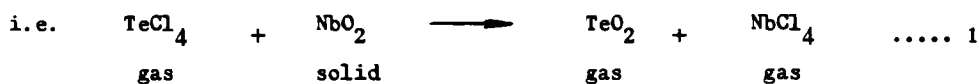
gradient will be small resulting in a slow transport rate. Similarly, if  $K$  is very small the partial pressures of the intermediate volatile compounds will be very low and again transport will be inhibited.

It seems, therefore, that chemical transport can only take place efficiently when  $K$  does not have an extreme value. Normally, the most efficient transport would be expected for a reaction with  $K \approx 1$ .

Since reasonably high transport rates are obtained for the growth of both  $Nb_2O_5$  and  $NbO$ , the chemical equilibrium constants for the reaction of these oxides with  $TeCl_4$  must have a value of the order of unity.

In the case of a non-ideal chemical transport reaction, the situation is somewhat more complicated. As an example, consider the reactions which result in the growth of  $Nb_{12}O_{29}$  crystals from  $NbO_2$  source material.

Assuming that the reaction at the source zone can be described as in equation 1.

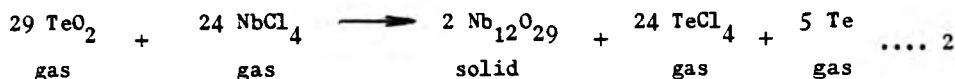


The equilibrium constant for this reaction  $K_s$  can be written

$$K_s = \frac{P_{sTeO_2} \times P_{sNbCl_4}}{P_{sTeCl_4}} \dots\dots 7 \quad \text{where } P_s \text{ is the partial pressure of the particular species at the source zone.}$$

Now for a high transport rate, it is essential to have substantial quantities of the reaction products generated in the source zone. Consequently, one might expect the optimum value of  $K_s$  to be as high as possible.

Again, assuming the reaction at the growth zone can be described by equation 2.



then the equilibrium constant in this case,  $K_g$ , will be given by:-

$$K_g = \frac{[P_g \text{ TeCl}_4]^{24} [P_g \text{ Te}]^5}{[P_g \text{ TeO}_2]^{29} [P_g \text{ NbCl}_4]^{24}} \dots\dots 8$$

Again, the efficient production of  $\text{Nb}_{12}\text{O}_{29}$  crystals apparently requires a large value of  $K_g$ . However inspection of equations 7 and 8 shows that  $K_s$  and  $K_g$  cannot both have a high value. If for example in equation 7  $K_s$  has a high value, then the partial pressures of  $\text{TeO}_2$  and  $\text{NbCl}_4$  at the source zone will be high. If it is reasonable to assume that the gases in the reaction tube mix efficiently, then the partial pressures of these gases at the growth zone will be similarly high. If this is the case then from equation 8 the value for  $K_g$  must be low and the growth zone reaction would therefore be unfavourable.

By similar reasoning it can be shown that a high value of  $K_g$  would require a low value of  $K_s$  and an unfavourable source zone reaction.

Thus as in the ideal case, efficient chemical transport requires that neither  $K_g$  nor  $K_s$  have extreme values.

### 3.4.2 The temperature dependence of the equilibrium constant.

Although in ideal systems, the equilibrium constant,  $K$ , in both the source and growth zones of the reaction vessel should be of the order of unity, chemical transport relies on a difference in the value of  $K$  in the two regions. Generally, chemical transport occurs as the result of the temperature dependence of  $K$ .



The equilibrium constant can be related to thermodynamic functions by the well known equation:-

$$\ln K = \frac{-\Delta G^\circ}{RT} = \frac{-\Delta H^\circ + T \Delta S^\circ}{RT} \quad \dots\dots 9$$

$$\text{Now } \Delta H^\circ_T = \Delta H^\circ_{298} + \int_{298}^T \Delta C_p dT \quad \dots\dots 10$$

$$\text{and } \Delta S^\circ_T = \Delta S^\circ_{298} + \int_{298}^T \frac{\Delta C_p}{T} dT \quad \dots\dots 11$$

Substituting equations 10 and 11, equation 9 becomes

$$\ln K = -\frac{\Delta H^\circ_{298}}{RT} - \frac{1}{RT} \int_{298}^T \Delta C_p dT + \frac{\Delta S^\circ_{298}}{R} + \frac{1}{R} \int_{298}^T \frac{\Delta C_p}{T} dT \quad \dots\dots 12$$

Differentiating this expression with respect to T,

$$\begin{aligned} \frac{d \ln K}{dT} &= \frac{\Delta H^\circ_{298}}{RT^2} + \frac{1}{RT^2} \int_{298}^T \Delta C_p dT \\ &= \frac{\Delta H^\circ_T}{RT^2} \quad \dots\dots 13 \end{aligned}$$

.. This is the well known van't Hoff equation.

Hence to have an appreciable variation of  $K$  with temperature  $\Delta H$  for the reaction must not be too small. For a given temperature gradient, the magnitude of  $\Delta H$  will govern the maximum obtainable transport rate. Also, the sign of  $\Delta H$  will indicate the direction of transport. Thus if  $\Delta H$  for the reaction between the starting material and the transport reagent is positive, then  $\frac{d \ln K}{dT}$  will also be positive. This means that the volatile reaction products have a higher partial pressure as the temperature is increased. Thus the direction of transport will be from the high temperature (high partial pressure) zone to the lower temperature (lower partial pressure) zone.

Similarly if  $\Delta H$  is negative for the reaction, material will be transported towards the hotter zone.

In the niobium-oxygen system, the growth of  $NbO$  crystals using  $TeCl_4$  as the transport reagent is the only example of transport from a cooler zone to a hotter zone. Thus, it can be concluded that for the reaction between  $NbO$  and  $TeCl_4$ ,  $\Delta H$  must be negative, whereas in the case of  $Nb_2O_5$ , for example, transport takes place from the hotter zone to the cooler zone. Hence for this reaction,  $\Delta H$  must be positive. (i.e. the reaction is endothermic).

### 3.5 Factors Which Influence the Transport Rate

In order to establish the principal factors which govern the transport rate, it is normal to consider chemical transport reactions as a series of sequential events.

Most sealed tube reactions can be conveniently described in terms of the following processes:-

- (a) The reaction at the source zone.
- (b) The transport of the reaction products from the source region to the growth region.

(c) The reaction of the volatile products at the growth zone, to produce single crystals.

Normally, for most chemical transport processes, the reactions at the source and growth zone can occur rapidly enough to maintain the quasi-equilibrium situation in these zones, and it is generally found that the transport of volatile products from the source zone to the growth zone is the rate determining process.

There are several mechanisms by which gases may be transported in a closed tube depending on the particular conditions and the geometry of the tube.

### 3.5.1 Diffusion.

If a concentration gradient exists in a mixture of gases, then there will be a net movement of gas molecules such that this concentration gradient is reduced. This phenomenon is referred to as diffusion.

It is found experimentally that the net flux of each component is proportional to the concentration gradient of that component.

$$\text{i.e. } J_i = - D_i \nabla C_i \quad \dots 14$$

This is a statement of the famous Fick's Law.

$D_i$  is the constant of proportionality (the diffusion coefficient)

$J_i$  is the net flux of species  $i$ .

$\nabla C_i$  is the concentration gradient of  $i$ .

The negative sign in the equation indicates that the direction of gas flow is such as to reduce the concentration gradient. Clearly in chemical transport, the diffusion rate will depend on the appropriate diffusion coefficients of the volatile species, and on the concentration gradients which exist.

The concentration gradients are a consequence of the quasi-equilibrium situations which are set up at the source and growth zones. Hence the difference between the equilibrium constants for the source and growth zones is important. For a normal chemical transport reaction, the variation of K (the equilibrium constant) with temperature is given by the von't Hoff equation (equation 13).

$$\frac{d \ln K}{dT} = \frac{\Delta H^{\circ}}{RT^2} \quad \dots 13$$

From this equation it is clear that increasing the temperature gradient for a given reaction will result in a larger difference in K, and a consequent increase in transport by diffusion.

Simple kinetic theory of gases (see for example Jeans (4)) predicts a variation of the diffusion coefficient (D) with temperature of the form:-

$$D \propto \frac{T^{3/2}}{p}$$

Now for constant volume  $p \propto T^*$

and hence  $D \propto T^{\frac{1}{2}}$

Thus the diffusion rate can be increased by increasing the temperature. This result shows that in diffusion controlled systems, chemical transport reactions will be most efficient when carried out at the highest practical temperatures. The highest temperature is usually limited by factors such as:-

- (a) the stability of the reaction vessel
- (b) the furnace design
- (c) the thermodynamic stability of the required crystals.

For most of the experiments performed in this work, the maximum temperatures used were limited by the use of silica reaction tubes to

\* See note overleaf

Note:

This statement is only strictly true for ideal non-associating gases.

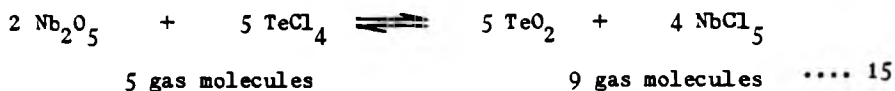
In the case of chemical transport, there are necessarily interactions between the gas molecules, and so the use of the "ideal" gas laws is an approximation.

between 1000°C and 1100°C. In some cases, much lower temperatures had to be used because the crystal phases required were only stable at these temperatures. The growth of B-Nb<sub>2</sub>O<sub>5</sub> and P-Nb<sub>2</sub>O<sub>5</sub> for example were carried out at temperatures below 600°C.

### 3.5.2 Stefan's flow.

In many chemical transport processes the reaction of the transport reagent with the source material results in an increase in the number of gas molecules.

As an example consider the transport of Nb<sub>2</sub>O<sub>5</sub>. Assuming the equation for the reaction can be written



At the source zone, there is clearly a net increase in the number of gas molecules as the reaction proceeds since during the reaction five molecules of TeCl<sub>4</sub> are consumed resulting in the generation of five TeO<sub>2</sub> molecules and four NbCl<sub>5</sub> molecules. At the growth zone, the reverse reaction occurs and there is a net reduction in the number of gas molecules.

The generation of gas molecules at the source zone and their subsequent removal at the growth zone constitutes a net flow of gas along the tube from the source to the growth zone. This phenomenon is known as Stefan's flow (5) and can be an important transport process in sealed tube chemical transport reactions.

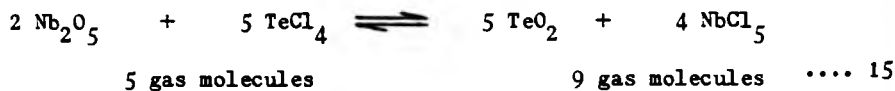
If the whole of the gas in the tube is considered to be moving away from the source zone with velocity U, and that simultaneously, the gases generated at the source zone and the rest of the gaseous contents

between 1000°C and 1100°C. In some cases, much lower temperatures had to be used because the crystal phases required were only stable at these temperatures. The growth of B-Nb<sub>2</sub>O<sub>5</sub> and P-Nb<sub>2</sub>O<sub>5</sub> for example were carried out at temperatures below 600°C.

### 3.5.2 Stefan's flow.

In many chemical transport processes the reaction of the transport reagent with the source material results in an increase in the number of gas molecules.

As an example consider the transport of Nb<sub>2</sub>O<sub>5</sub>. Assuming the equation for the reaction can be written



At the source zone, there is clearly a net increase in the number of gas molecules as the reaction proceeds since during the reaction five molecules of TeCl<sub>4</sub> are consumed resulting in the generation of five TeO<sub>2</sub> molecules and four NbCl<sub>5</sub> molecules. At the growth zone, the reverse reaction occurs and there is a net reduction in the number of gas molecules.

The generation of gas molecules at the source zone and their subsequent removal at the growth zone constitutes a net flow of gas along the tube from the source to the growth zone. This phenomenon is known as Stefan's flow (5) and can be an important transport process in sealed tube chemical transport reactions.

If the whole of the gas in the tube is considered to be moving away from the source zone with velocity U, and that simultaneously, the gases generated at the source zone and the rest of the gaseous contents

of the tube are diffusing into each other, then the net flux can be described in terms of a flow term and a diffusion term.

In a simple system, such as the transport of a volatile solid in the presence of an inert gas, the flow can be described by the following equations:-

$$J_{\text{vap}} = \frac{U}{RT} p_{\text{vap}} - \frac{D}{RT} \frac{dp_{\text{vap}}}{dx} \quad \dots\dots 16$$

where  $J_{\text{vap}}$  is the flux of the vapour  
 $p_{\text{vap}}$  is the partial pressure  
 $D$  is the diffusion coefficient  
 $T$  is the temperature  
 $x$  is the position co-ordinate in the tube.

Similarly, for the inert gas,

$$J_{\text{i.g.}} = \frac{U p_{\text{i.g.}}}{RT} - \frac{D}{RT} \frac{dp_{\text{i.g.}}}{dx} = 0 \quad \dots\dots 17$$

No net flow of inert gas will occur (ignoring the small flow which results from the transfer of solid from the source to the growth zone).

Adding these two equations and simplifying:-

$$J_{\text{vap}} = \frac{Up}{RT} - \frac{D}{RT} \frac{dp}{dx} \quad \dots\dots 18$$

where  $p$  is the total pressure in the tube.

Now normally  $\frac{dp}{dx}$  will be negligibly small (except when the velocity is large.)



$$\text{Hence } \frac{J_{\text{vap}}}{P} = \frac{U}{RT} \quad \dots\dots 19$$

Substituting into equation 16

$$J_{\text{vap}} \frac{RT}{P} = \frac{D}{P - p_{\text{vap}}} \frac{dp_{\text{vap}}}{dx} \quad \dots\dots 20$$

When  $p_{\text{vap}}$  is small compared to the total pressure,  $P$ , in the tube, the equation describes a diffusion only process. However, as  $p_{\text{vap}}$  increases, the flow rate  $J$  is increased. Hence Stefan's flow will be particularly important in cases where the volatile products of the source zone reaction have significant vapour pressures.

In the growth of most of the niobium oxides using  $\text{TeCl}_4$  as transport reagent, the source zone reaction results in an increase in the number of gas molecules and hence Stefan's flow will contribute to the transport rate. A study of the non-ideal examples of chemical transport, such as for example  $\text{Nb}_{12}\text{O}_{29}$ , shows that as the reaction progresses, there is a gradual build up of inactive gaseous components. The rise in the partial pressures of these gases relative to the active transporting components will result in a decrease in the Stefan's flow contribution to the transport rate.

### 3.5.3 Convection,

The term convection is used to describe the motion of macroscopic regions of a fluid under the influence of forces such as gravity. Raising the temperature of a body of gas, causes expansion and a decrease in density. Under the action of gravity, cooler, denser gas displaces it. This phenomenon is termed thermal convection.

In chemical transport reactions density differences can also arise from the variations in composition which occur as a result of the chemical reactions.

The contribution of convection to the transport rate is strongly dependent on the geometry of the reaction ampoule. For example, in horizontally mounted tubes of narrow bore, the convection which occurs is generally found to be negligible (6). However, by increasing the cross-section or by arranging the tube vertically, large convection currents can be induced. The analytical treatment of convection in such systems is beyond the scope of this work, however the results of such an analysis shows that convective flow is proportional to the total pressure in the vessel and so can be minimised by keeping the pressure as low as possible.

Where the convective velocity is very large, the partial pressures in the body of the reaction vessel will be approximately uniform along its length.

Normally a uniform partial pressure gradient is established between the source zone and growth zone. However since the partial pressure during convective flow is uniform over most of the length of the tube large compositions gradients must inevitably result at the source and growth zones. These large gradients in the vicinity of the growing crystals may detrimentally affect the surface stability of the crystals and lead to dendritic growth behaviour.

Thus despite the fact that convection should result in enhanced transport kinetics, no attempt was made to induce convection by modifying the geometry of the reaction vessel. Thus in the experiments described here, the effects of convection should be negligible.

#### 3.5.4 The rate determining processes.

In a chemical transport reaction, the transport rate will depend on the quasi-equilibrium vapour pressures which exist at the source and growth zones, and on the kinetics of the processes by which vapour is

transported between these two regions.

The complicated and uncertain nature of chemical reactions which result in the transport of niobium oxides mean that precise understanding of the equilibrium conditions which exist at the source and growth zones is not yet possible.

By general discussions of vapour transport systems it seems that for the conditions of growth which were used, the most important contributions to the transport rate will be due to Stefan's flow and diffusion.

A study of these phenomena indicates that if required, improvements in the transport rate could be achieved by increasing the overall temperature or increasing the temperature gradient. Alternatively the presence of an inert gas in the system would increase the overall working pressure and result in a decrease in the transport rate.

### 3.5.5 The transport rate in non-conservative systems.

There have been several publications recently describing the growth of  $\text{Nb}_{12}\text{O}_{29}$  and  $\text{NbO}_2$  crystals by chemical transport reactions using various transport reagents (7, 8, 9). The authors have estimated the transport rates achieved in their experiments in order to compare the transport ability of the various reagents. In all cases, they assumed that the transport rate remained constant during the experiment.

The evidence presented here, however, shows that in non-ideal chemical transport systems, the active transport reagent is gradually consumed during the reaction, leading to a progressive decrease in the transport rate. Hence the transport rates quoted in the previously cited works are in fact average transport rates, and the initial transport rate is probably significantly higher. Furthermore it has been shown earlier in this chapter that the total yield of  $\text{Nb}_{12}\text{O}_{29}$  is a function of the initial level of the

transport reagent which is present. Where yields of  $Nb_{12}O_{29}$  have been quoted by other workers, they are in agreement with the predictions of equation 4, falling below the predicted maximum yield.

### 3.6 The Simultaneous Growth of Different Crystal Species

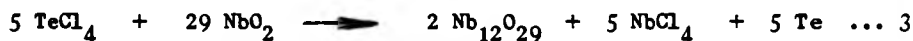
Reference to Table 2.1 shows three examples of crystal growth experiments in which two different crystal species were produced in different regions of the reaction tube. In this section, the conditions of growth are discussed for each of these cases.

#### 3.6.1 The simultaneous growth of $NbO_2$ and $Nb_{12}O_{29}$ crystals.

With  $NbO_2$  as the starting material and  $TeCl_4$  as the transport reagent crystals of  $NbO_2$  and  $Nb_{12}O_{29}$  can be prepared. The growth conditions used in this reaction are illustrated by Fig. 3.2.

It has already been pointed out that the growth of  $Nb_{12}O_{29}$  crystals in this way necessarily involves a change in the composition of the gaseous reactants. It is interesting to consider, therefore, the effect of these changing reaction conditions on the system.

Assume that initially  $Nb_{12}O_{29}$  crystals nucleate and begin to grow at the extreme end of the reaction vessel. This reaction has been described previously by the equation



Thus as the  $Nb_{12}O_{29}$  crystals grow,  $TeCl_4$  is consumed and  $NbCl_4$  and Te are generated. The gas in the reaction tube therefore becomes enriched with the Nb-bearing  $NbCl_4$  and depleted in  $TeCl_4$ , the transport reagent. This gradual change in the chemistry of the vapour phase may have one of two possible consequences.

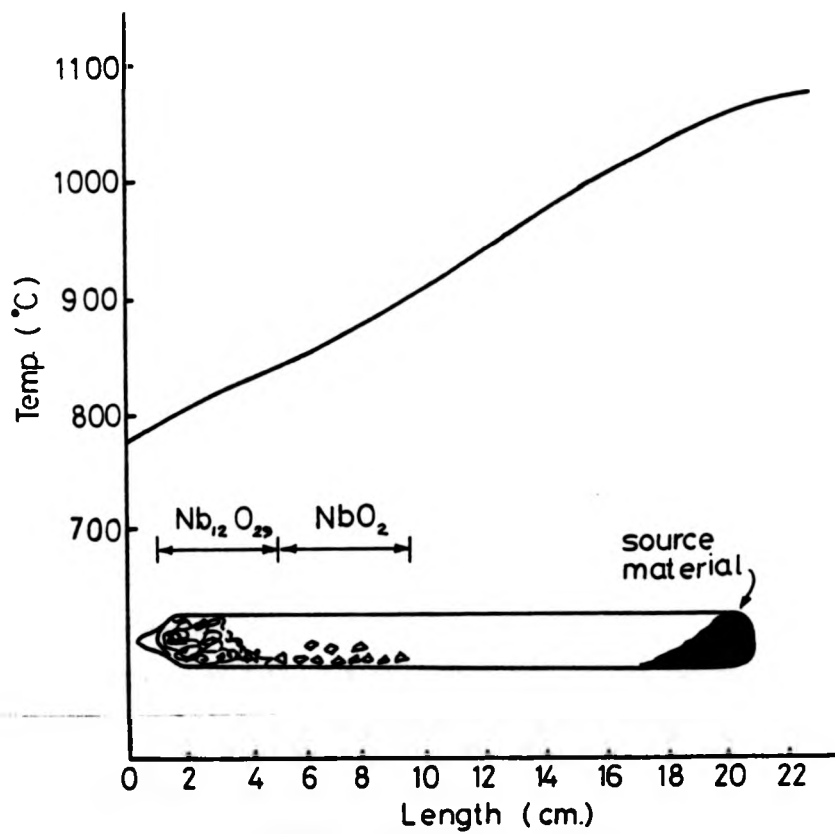


Fig. 3.2. Conditions for the growth of NbO<sub>2</sub> and Nb<sub>12</sub>O<sub>29</sub>

Firstly, the  $\text{TeCl}_4$  transport reagent may eventually become completely exhausted. When this happens no further transport will take place. This condition, however, will be reached asymptotically, the transport rate gradually becoming slower and slower.

The other possibility is that as the vapour in the reaction tube becomes more and more enriched with Nb-bearing phases, a condition may be reached at which  $\text{NbO}_2$  crystals can nucleate and begin to grow. Now since the source material is  $\text{NbO}_2$ , this reaction constitutes a normal chemical transport process which involves no further changes in the vapour composition.

Consider in this case the spatial variation of the vapour composition along the reaction tube. At the source end, the composition of the gases must be such that  $\text{NbO}_2$  reacts to form volatile products. In the region above the growing  $\text{Nb}_{12}\text{O}_{29}$  crystals, the gas must be of a composition which causes the precipitation to proceed. A relatively uniform composition gradient will exist between these two extremes. Hence it is not surprising that when the gases have been suitably enriched by Nb-containing volatiles, the nucleation and growth of  $\text{NbO}_2$  crystals takes place at an intermediate point in the tube.

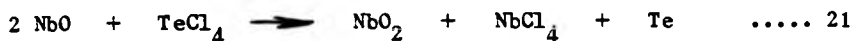
Reference to Table 2.8 shows that both of the two cases described here have been realised experimentally.

### 3.6.2 Niobium dioxide and niobium ditelluride.

If the growth of  $\text{NbO}_2$  crystals from  $\text{NbO}$  powder is carried out using a relatively large quantity of  $\text{TeCl}_4$ , metallic, hexagonal platelets of  $\text{NbTe}_2$  are also produced. In this case, however, the two species of crystal are not well spatially separated but grow together at the cooler end of the reaction tube.

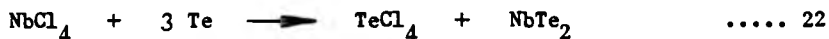
The growth of NbO<sub>2</sub> from powdered NbO is once again an example of a non-ideal process, the composition of the gaseous phase being changed during the reaction.

The proposed chemical reaction for this process is as follows:-

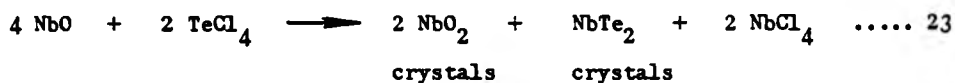


Thus as growth proceeds, some of the transport reagent is used up, the resulting gases becoming richer in NbCl<sub>4</sub> and tellurium (Te) vapour.

Where only small quantities of TeCl<sub>4</sub> were used it quickly becomes consumed by the reaction and transport is stopped. However, if a larger quantity of TeCl<sub>4</sub> is introduced, the concentrations of tellurium vapour and NbCl<sub>4</sub> vapour build up in the tube and eventually the following reaction may be possible.



By combining equations 21 and 22 an overall equation for the reaction may be written:-



In this case, the second crystalline phase (NbTe<sub>2</sub>) is not constrained by vapour composition gradients as in the previous case, and so the crystals of NbTe<sub>2</sub> therefore grow at the extreme end of the reaction tube alongside the crystals of NbO<sub>2</sub>.

### 3.6.3 The polymorphic phases of $\text{Nb}_2\text{O}_5$ .

Under certain conditions it is possible to grow two polymorphic forms of  $\text{Nb}_2\text{O}_5$  simultaneously. This example is perhaps the simplest case of simultaneous growth since the phase which forms depends on the temperature of the growth zone.

Fig. 3.3 shows the conditions which were used to grow B- $\text{Nb}_2\text{O}_5$  and P- $\text{Nb}_2\text{O}_5$  crystals. The B- $\text{Nb}_2\text{O}_5$  crystals were formed in the hotter part of the growth zone, whereas the P- $\text{Nb}_2\text{O}_5$  crystals grew only in the coolest region.

By increasing the temperature of the growth zone by 20 - 30°C it was possible to grow the B-form only. Alternatively, lowering the temperature encouraged the growth of P- $\text{Nb}_2\text{O}_5$  crystals in a larger proportion of the growth zone at the expense of some of the B- $\text{Nb}_2\text{O}_5$  crystals. The conclusion of this experiment is that under the conditions of growth P- $\text{Nb}_2\text{O}_5$  is the more stable form at lower temperatures, but is less stable than B- $\text{Nb}_2\text{O}_5$  above about 550°C.

This result is in good agreement with the work of Kodama et al. (10), who have studied the relative stabilities of several forms of  $\text{Nb}_2\text{O}_5$ .



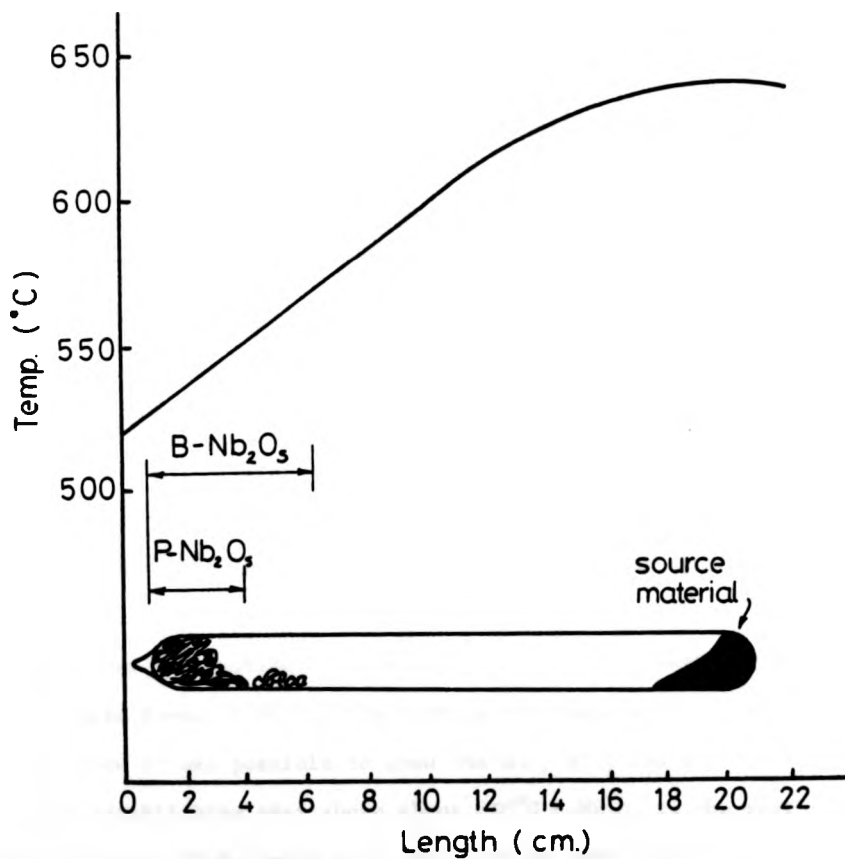


Fig. 3.3. Conditions for the growth of B-Nb<sub>2</sub>O<sub>5</sub> and P-Nb<sub>2</sub>O<sub>5</sub>

SUMMARY

In this chapter it has been demonstrated that by careful consideration of the chemistry of the transport reactions, many of the experimental observations can be adequately explained.

Of particular interest are the reactions in which the transport reagent is consumed during crystal growth. The consequences of this are:-

- (a) there is a relationship between the maximum obtainable yield and the quantity of transport reagent used.
- (b) the transport rate gradually decreases during growth.
- (c) in some cases a point is reached at which the growth conditions have changed to such an extent that the growth of a different crystalline species is favoured.

Further interesting observations concern the growth of the polymorphic forms of  $\text{Nb}_2\text{O}_5$ . By varying the temperature of the growth zone it was possible to grow the H-, B-, and P- forms, thereby establishing that above about  $850^\circ\text{C}$  H- $\text{Nb}_2\text{O}_5$  is the most stable form, P- $\text{Nb}_2\text{O}_5$  being most stable below about  $550^\circ\text{C}$  with B- $\text{Nb}_2\text{O}_5$  being the stable phase between these two temperatures.

REFERENCES

- (1) H. Schafer in "Crystal Growth: An Introduction" ed. P. Hartman. North Holland, Amsterdam 197.
- (2) H. Schafer "Chemical Transport Reactions", Academic Press, New York, (1964)
- (3) M. M. Faktor and I. Garrett, "Growth of Crystals from the Vapour" Chapman and Hall, London (1974)
- (4) Jeans, Sir J., "An Introduction to the Kinetic Theory of Gases", University Press, Cambridge (1962)
- (5) J. Stefan, Annalen der Physik und Chemie, 17, 550; (1890)
- (6) E. R. G. Eckert and R. M. Drake, "Heat and Mass Transfer", McGraw-Hill, New York (1959)
- (7) T. Sakata, K. Sakata, G. Hofer, T. Horiuchi, J. Cryst. Growth 12, 88, (1972).
- (8) H. Kodama and M. Goto, J. Cryst. Growth 29, 77, (1975)
- (9) H. Kodama and M. Goto, J. Cryst. Growth 29, 222, (1975)
- (10) H. Kodama, T. Kikuchi and M. Goto, J. Less-Common Metals, 29, 415, (1972)

## CHAPTER FOUR

### CRYSTAL GROWTH MECHANISMS AND MORPHOLOGY

So far the discussion of crystal growth has been mainly concerned with the mechanisms by which material is transported from the source zone to the growth zone during chemical transport. In this chapter, the processes which occur at the growth zone are considered.

The first part of the chapter is devoted to a survey of the various theories of nucleation and growth of crystals from the vapour. For each of the proposed mechanisms, the predicted rates of crystal growth as a function of supersaturation are discussed and compared.

The growth habits of some of the niobium oxide crystals have been determined, and this evidence along with the results of a scanning electron microscope examination of the surface morphology of the crystals is considered in terms of the crystal growth mechanisms.

Although the degree of supersaturation during crystal growth by chemical transport is difficult to estimate quantitatively, it is possible in some of the systems described, to relate differences in growth habits to changes in supersaturation.

The consequences of the gradual change in supersaturation which occurs during non-ideal chemical transport processes are also discussed.

#### 4.1 Experimental Techniques

The various species of crystal were examined by standard techniques such as scanning electron microscopy, light microscopy and Laue back-reflection X-ray photography. Using these methods it was normally possible to determine the preferred facet planes and where appropriate, the principal growth directions. Growth features on the surfaces of the crystals were studied in greater detail using the scanning electron microscope (S.E.M.).

With the exception of NbO, the crystals studied have low electrical conductivity, and to minimise charging of the specimens in the S.E.M. it was necessary to deposit a thin layer of gold-palladium onto the surfaces by evaporation under vacuum.

A computer program (1) which generates stereographic projections for any given crystal structure was used extensively in this work and greatly facilitated the indexing of the Laue patterns.

#### 4.2 The Theories of Crystal Growth from the Vapour

In this section a brief description is given of the principal mechanisms which have been proposed to explain the addition of atoms or molecules to a growing crystal surface. In particular, where possible, the predicted dependence of growth rate on supersaturation is included.

A more detailed description of the mechanisms described here can be found in most standard textbooks on crystal growth. (see for example references 2 - 5).

##### 4.2.1 Continuous or normal growth

Early models of crystal growth (6, 7) were based on the assumption that all atoms arriving at the surface of a crystal can become attached. During crystal growth, more atoms arrive at the surface than depart and so there is a net build up of atoms randomly over the crystal. The growth rate can simply be calculated from the net rate of arrival of atoms at the interface.

Now the rate of arrival of atoms of a particular species,  $x$ , at the interface per unit area,  $R_x$ , will be proportional to the partial pressure of that species,  $p_x$ .

$$\text{i.e. } R_x \propto p_x$$

Similarly the rate at which atoms of the same species will evaporate from the interface per unit area  $R_x^1$  will be proportional to the equilibrium vapour pressure,  $p_{ox}$ .

$$R_x^1 \propto p_{ox}$$

Hence the net rate of deposition of species x will be given by

$$R_x - R_x^1 \propto \Delta p_x \dots\dots\dots 1 \text{ where } \Delta p_x = p_x - p_{ox}$$

Thus the growth rate of the crystal will be proportional to the supersaturation.

The continuous growth theory implies the equivalence of all surface sites and does not attempt to consider the effects of surface diffusion. Furthermore, this model does not account for the tendency of crystals to develop facets parallel to close packed crystallographic planes.

4.2.2 Growth by the propagation of steps

In 1927, Kossel (8) first pointed out that a crystal face having steps on it will grow by the addition of atoms to the kinks in the steps.\* For simplicity consider a simple cubic model of a crystal (Kossel crystal) as shown in Fig. 4.1. Three possible sites at which atoms could become attached are indicated, however a simple consideration of the nearest and next nearest neighbour interactions at these sites clearly shows that the kink sites will be preferred. For example consider an atom on the crystal surface at position 1. In this position it will have one nearest neighbour and four next nearest neighbours to interact with. If the interaction energy between nearest neighbours is  $2 \bar{\bar{e}}$ , and between next nearest neighbours is  $2 \bar{\bar{e}}_2$ ,

\* The terrace-ledge-kink (TLK) model, developed from Kossel's ideas is described in detail in standard text books (e.g. (35)).

Fig. 4.1. Simple Kossel crystal showing sites at which atoms can become attached.

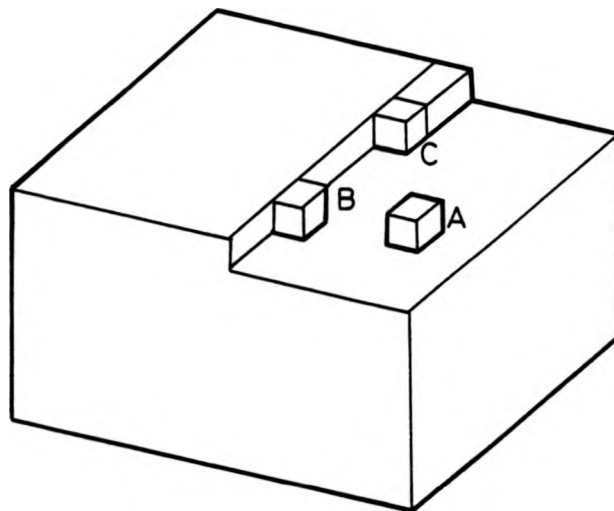
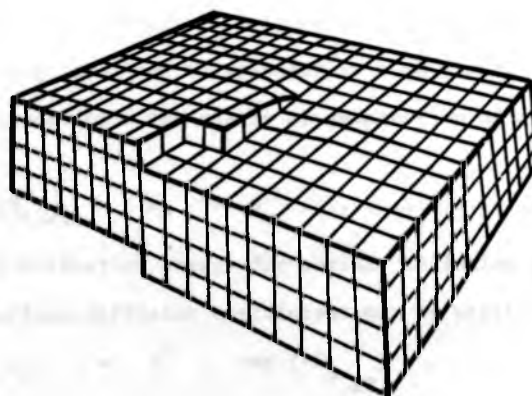


Fig. 4.2. Simple representation of an emergent screw dislocation.



then the total energy gained by the deposition of an atom at sites of type A will be  $2\bar{-}_1 + 8\bar{-}_2$ . Similarly at the step sites (type B in Fig.4.1) there are two nearest neighbours and six next nearest neighbours. The gain in energy will therefore be  $4\bar{-}_1 + 12\bar{-}_2$ .

The energy gain at the kink sites (type C) will be  $6\bar{-}_1 + 12\bar{-}_2$ .

Atoms arriving at the surface of such a crystal will generally become attached to positions of type A. However, the relatively weak interaction at such sites means that they will tend to diffuse over the surface and eventually evaporate. If before re-evaporation, the diffusing atom encounters a surface step, it will become more strongly bound and consequently less likely to evaporate. It may however still diffuse, but will prefer to diffuse along the ledge, eventually arriving at a kink site (type C) where it can again form extra bonds with the crystal.

If the energy required to transfer an atom from a kink (type C) site to a surface (type A) site is  $W_k$ , then for a crystal face in equilibrium with the vapour the fraction of surface site occupied will be given by:

$$\alpha_0^s = \exp\left(\frac{-W_k}{kT}\right) \dots\dots\dots 2$$

Now the total energy of evaporation of an atom,  $\Delta h_{s,v}$ , will be equal to the energy required to transfer an atom from a kink to the surface,  $W_k$ , and in addition the energy of evaporation of a surface atom,  $W_s$

$$\text{i.e. } \Delta h_{s,v} = W_k + W_s \dots\dots\dots 3$$

If the activation energy for surface diffusion of an atom is  $E_s$ , then the surface diffusion coefficient may be written:

$$D_s = r^2 v \exp\left(\frac{-E_s}{kT}\right) \dots\dots\dots 4$$



then the total energy gained by the deposition of an atom at sites of type A will be  $2\bar{-}_1 + 8\bar{-}_2$ . Similarly at the step sites (type B in Fig.4.1) there are two nearest neighbours and six next nearest neighbours. The gain in energy will therefore be  $4\bar{-}_1 + 12\bar{-}_2$ .

The energy gain at the kink sites (type C) will be  $6\bar{-}_1 + 12\bar{-}_2$ .

Atoms arriving at the surface of such a crystal will generally become attached to positions of type A. However, the relatively weak interaction at such sites means that they will tend to diffuse over the surface and eventually evaporate. If before re-evaporation, the diffusing atom encounters a surface step, it will become more strongly bound and consequently less likely to evaporate. It may however still diffuse, but will prefer to diffuse along the ledge, eventually arriving at a kink site (type C) where it can again form extra bonds with the crystal.

If the energy required to transfer an atom from a kink (type C) site to a surface (type A) site is  $W_k$ , then for a crystal face in equilibrium with the vapour the fraction of surface site occupied will be given by:

$$\alpha_o^s = \exp\left(\frac{-W_k}{kT}\right) \dots\dots\dots 2$$

Now the total energy of evaporation of an atom,  $\Delta h_{s,v}$ , will be equal to the energy required to transfer an atom from a kink to the surface,  $W_k$ , and in addition the energy of evaporation of a surface atom,

$$W_s \quad \text{i.e.} \quad \Delta h_{s,v} = W_k + W_s \dots\dots\dots 3$$

If the activation energy for surface diffusion of an atom is  $E_s$ , then the surface diffusion coefficient may be written:

$$D_s = r^2 v \exp\left(\frac{-E_s}{kT}\right) \dots\dots\dots 4$$

and the mean time  $\tau_s$ , which elapses before re-evaporation will be given by:-

$$\frac{1}{\tau_s} = \nu \exp \left( \frac{-W_s}{kT} \right) \quad \dots 5$$

In equations 3 and 4,  $\nu$  is a frequency factor and in each case it is of the order of the atomic frequency of vibration. For this argument they will be assumed to be equal.

Using Einstein's equation for Brownian motion

$$x_s^2 = D \tau_s \quad \dots 6$$

the mean displacement,  $x_s$ , of an atom before re-evaporation can be calculated.

$$x_s = r \exp \left\{ \frac{(W_s - E_s)}{2kT} \right\} \quad \dots 7$$

Now  $E_s$  is generally very much smaller than  $W_s$ , and so  $x_s$  is larger than  $r$ . From this the importance of surface diffusion in the growth of a step is evident. In fact  $x_s$  is generally large compared to the mean distance between kinks in a step. Based on these results it is possible to calculate the rate of advance of a straight step in contact with a supersaturated vapour.

For a stepped face in equilibrium with the vapour, the rate of evaporation of atoms from a given site per unit time will be the product of the fraction of such sites occupied ( $\alpha_0^s$ ) and the frequency of evaporation of each such atom ( $\frac{1}{\tau_s}$ ). In a supersaturated vapour, more atoms will be arriving than evaporating. Thus,  $\frac{i \alpha_0^s}{\tau_s}$  atoms will strike each lattice

site in unit time where  $i$  is the supersaturation ratio defined by  $i = \frac{p}{p_0}$

where  $p$  is the partial pressure

and  $p_0$  is the equilibrium partial pressure.

On average, all atoms adsorbed within a distance  $x_s$  of a step will reach the step before evaporating. Thus the number of atoms reaching a step in unit time will be  $\frac{2x_s i \alpha_o^s}{\tau_s}$ . The factor of two arises because atoms may approach the step from either side.

Similarly the number of atoms leaving a unit length of step per unit time is given by  $\frac{2x_s \alpha_o^s}{\tau_s}$ . Hence the net rate of addition of atoms to the step is :

$$\frac{2x_s(i - 1)\alpha_o^s}{\tau_s}$$

Substituting for  $\alpha_o^s$  and  $\tau_s$  from equations 2 and 5 the velocity,  $U$ , at which the step moves will be given by:

$$\begin{aligned} U &= 2(i - 1)x_s \alpha_o^s \\ &= 2(i - 1)x_s v \exp\left(\frac{-W_k - W_s}{kT}\right) \\ &= 2(i - 1)x_s v \exp\left(\frac{-\Delta H_{s.v.}}{kT}\right) \dots\dots\dots 8 \end{aligned}$$

$i - 1$  can be written as  $\frac{(p - p_o)}{p_o}$  and this is usually referred to as the supersaturation  $j$ .

Thus equation 8 implies that a step will advance with a velocity proportional to the degree of supersaturation in the vapour.

The argument presented here is by no means rigorous, and does not for example take account of the fact that when steps are close together there is competition between them for the available atoms.

A more correct treatment taking this effect into account leads

to the following expression:-

$$U = 2(i - 1) \beta x_s \gamma \exp \left( - \frac{\Delta h_{s.v.}}{kT} \right) \tanh \left( \frac{y}{2x_s} \right) \quad \dots 9$$

where  $y$  is the mean separation between steps.

The factor  $\beta$  is the fraction of atoms reaching a step which become attached.

Further refinements of the theory of step growth take into account the tendency of steps to bunch together under some conditions, leading to phenomena such as platelet growth.

From these arguments it is clear that a stepped crystal face will grow rapidly even at low supersaturations, and as a consequence of this, such faces rapidly disappear from the crystal, and the crystal is limited by slowly growing faces.

To extend the principle of step growth to low index smooth faces it becomes necessary to consider mechanisms by which steps can be generated on such a surface. One such a mechanism is proposed in the island nucleation theory.

#### 4.2.3 The island nucleation theory

Consider a perfectly smooth, low index crystal surface at which atoms are continually arriving. The first atoms to arrive may attach themselves to the surface at any position since all the surface sites will be equivalent. These atoms will diffuse over the surface and may eventually re-evaporate. However, as the atoms diffuse they may interact with one another and become paired or form small clusters. The nucleation of such a two dimensional cluster provides ledge sites and the island nucleus can grow by the propagation of the ledge as described in the previous section.

Thus to fully describe the growth process it is necessary to discuss the factors controlling the formation of such island nuclei.

The free energy,  $\Delta G$ , which results from the formation of a circular nucleus of radius  $r$  will be given by:-

$$\Delta G = n (g_s - g_v) + 2 \pi r \gamma \quad \dots 10$$

when  $n$  is the number of atoms in the nucleus.

$g_s, g_v$  are the free energies per atom in the solid and vapour respectively.

$\gamma$  is the edge free energy per unit length (assumed to be isotropic in this case).

If the area occupied by an adsorbed atom is  $a$ , then

$$na = \pi r^2$$

and equation 10 can be rewritten as

$$\Delta G = \frac{\pi r^2}{a} (g_s - g_v) + 2 \pi r \gamma \quad \dots 11$$

For such an island nucleus, there will be a certain critical radius below which it would be advantageous for atoms to be lost, and above which it would be advantageous to grow further.

This critical radius,  $r_c$ , will occur when  $\frac{\partial \Delta G}{\partial r} = 0$

$$\text{i.e.} \quad \frac{2 \pi r_c}{a} (g_s - g_v) + 2 \pi \gamma = 0 \quad \dots 12$$

$$\therefore r_c = \frac{\gamma a}{(g_v - g_s)} \quad \dots 13$$

Now by treating the vapour as an ideal gas it is possible to derive a relationship between  $p_x$ , the vapour pressure in equilibrium with a perfectly smooth crystal surface, and  $p_r$ , the vapour pressure in equilibrium with an island nucleus of radius  $r$ .

When the vapour pressure is  $p_x$ , then  $g_v = g_s$

similarly when the vapour pressure is  $p_r$ ,  $(g_v - g_s) = \frac{\gamma a}{r}$

Differentiating this expression and remembering that at constant temperature  $dg_v = V_v dp$  and  $dg_s = V_s dp$ .

$V_v$  and  $V_s$  being the volumes per atom in the vapour and solid states.

$$\text{then } (V_v - V_s) dp = -\frac{\gamma a}{r^2} dr \quad \dots 14$$

Now  $V_s$  is small in comparison with  $V_v$  and can be neglected.

Also  $V_v = \frac{kT}{p}$  if the perfect gas approximation holds.

Thus equation 17 becomes

$$\frac{kT}{p} dp = \frac{\gamma a}{r^2} dr \quad \dots 15$$

Integrating from  $p_\infty$  to  $p_r$  and between  $r = \infty$  and  $r$ ;

$$\text{then } kT \ln \frac{p_r}{p_\infty} = \frac{\gamma a}{r} \quad \dots$$

$$\therefore \ln i = \ln \frac{p_r}{p_\infty} = \frac{\gamma a}{rkT} \quad \dots 16$$

where  $i$  is the supersaturation ratio.

The maximum value of free energy increase  $G_c$  can be obtained by combining equations 16 and 14 giving

$$\Delta G_c = \pi \gamma r_c = \pi \gamma^2 a / (kT \ln i) \quad \dots 17$$

The discussion so far has been restricted to the case of an isotropic crystal surface and circular nuclei. When the crystal structure effects are considered and non-circular nuclei result, equation 20 has to be modified and can be written

$$\Delta G_c = C_{22} \gamma^2 a / (kT \ln i) \quad \dots 18$$

$C_{22}$  is a factor which takes into account surface anisotropies.

Now applying the Volmer-Becker theory (9) to two dimensional nucleation, the nucleation rate,  $I$ , will be given by:-

$$I = C_{23} \exp(-\Delta G_c / kT) \quad \dots 19$$

The factor  $C_{23}$  in this equation is not well defined but is approximately equal to the collision frequency of vapour molecules at the surface.

If the rate of growth of a nucleus of greater than the critical size is assumed to be very rapid, then the rate of growth of the crystal in atomic layers per second will be determined by  $I$ , the nucleation rate.

It is useful at this point to evaluate the growth rate predicted by this mechanism for a typical crystal. Frank performed such a calculation and estimated that  $C_{23}$  for a  $1 \text{ mm}^2$  area of crystal face would have a value of about  $10^{22}$ . For the minimum growth rate which could be experimentally detected ( $\sim 1 \mu\text{m}$  per month)  $G_c / kT$  would need to be less than or equal to  $\ln 10^{30} \approx 70$ . This gives  $\ln i \geq 4 \gamma^2 a / (kT^2 \approx 70)$  and leads to the result that a supersaturation of at least 25% would be required. The nucleation rate is very strongly dependent on the supersaturation. Below a certain critical supersaturation, the growth rate is negligible, and above this supersaturation growth is limited by the rate of growth of the nuclei, not by the nucleation rate.

There is very little experimental evidence to support the island nucleation model, although Haward (10), observed the predicted behaviour for the growth of iodine crystals from the vapour.

However there have been many observations suggesting that other growth mechanisms are more important and numerous examples of crystals exhibiting appreciable growth rates at low supersaturations (down to about 1%) have been observed. To explain these results a theory of dislocation assisted growth was proposed by Frank (11).

#### 4.2.4 The dislocation theory of crystal growth

Frank recognised that when a screw dislocation emerges at an otherwise perfect crystal face, a step is generated across part of the face.\* This is illustrated schematically in Fig. 4.2. Furthermore, such a step will persist during growth, new crystal layers growing in a spiral manner around the dislocation. Burton, Cabrera and Frank (12) discussed the growth kinetics of such a surface in some detail. For the purposes of this work a brief summary of the more important features of the model will be described.

In a supersaturated vapour, the step generated by a screw dislocation will advance across the crystal face. However, one end of the step is constrained by the dislocation and cannot advance and so the step must become curved. When the radius of curvature reaches the value,  $r_c$ , determined in the previous section, the step at this point will have zero velocity of advance. Eventually the growing step will develop into a spiral as shown in Fig. 4.3 such that at all points on this spiral the radius of curvature is greater than  $r_c$ .

Modifying equation 8 to take account of the effect of curvature of a step

$$U_r = 2 (i - i^1) x_s \nu \exp \left( - \frac{\Delta h_{s.v.}}{kT} \right) \dots 20$$

where  $i^1$  is the supersaturation ratio for the particular step and takes account of the fact that a curved step has a greater evaporation rate than a straight step.

\* See note overleaf



Note:

To generate a growth spiral, dislocations do not need to be purely screw in character. Any dislocation which has a screw component can give rise to a growth spiral, although in general the burger's vector will not be parallel to the growth direction and the dislocation will eventually "run out" to the edge of the crystal. Pure screw dislocations are the only ones which have burger's vectors parallel to the growth direction.

Fig. 4.3

The development of a growth spiral

Fig. 4.3 (a) represents the surface of a crystal with a single emergent screw dislocation and the associated surface step. The addition of atoms to the step cause it to advance over the surface and successive positions are numbered 1-4. The advancing step is constrained at the dislocation core and therefore develops as a spiral as shown in (b) and (c). The sectional view through the dislocation core (d) shows the multiply stepped surface which eventually develops.

N.B. Any dislocation which has a screw component will result in the generation of a spiral step if it intersects the growing surface.

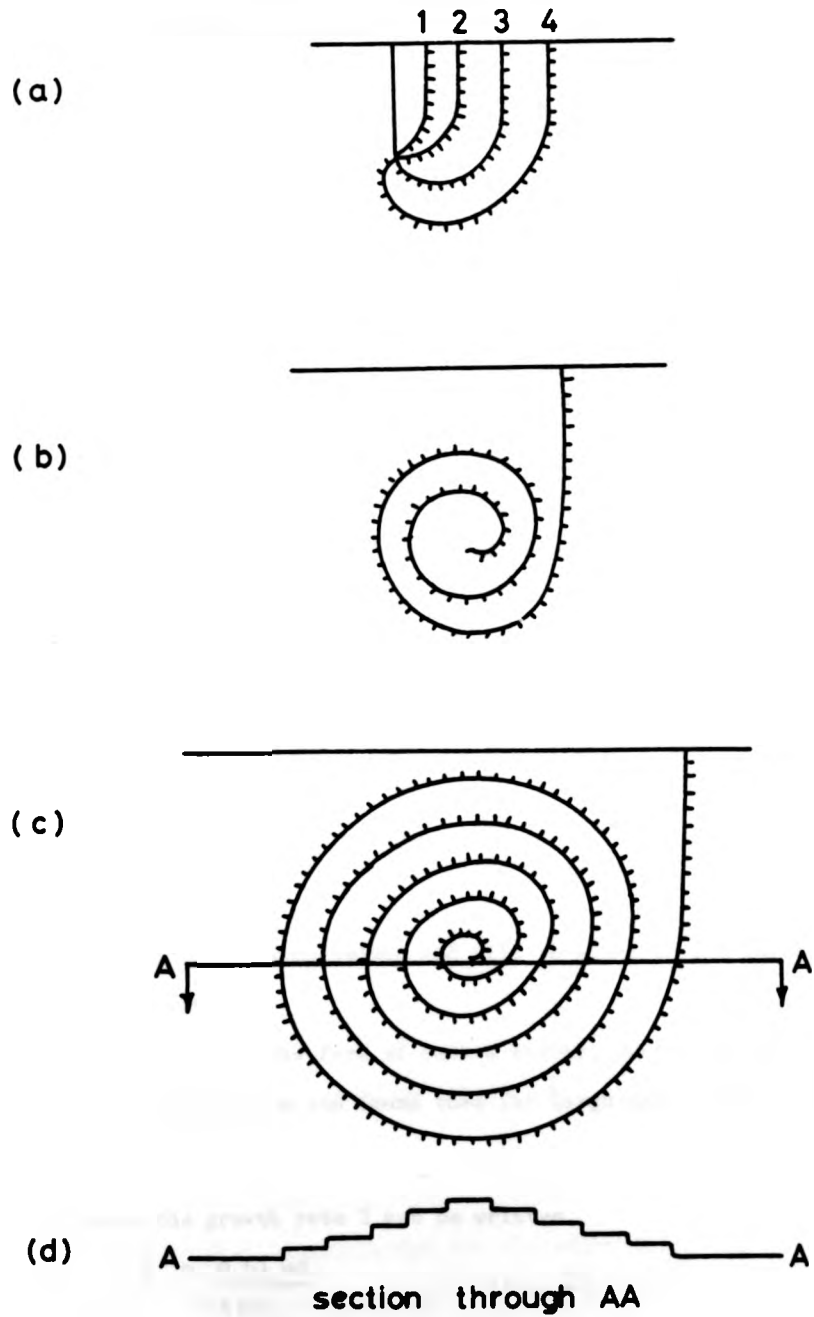


Fig. 4.3. The development of a growth spiral.

From equation 16

$$\ln i = \frac{\gamma a}{r_c kT} \quad \text{where in this case } r_c \text{ is the equilibrium radius of curvature of the boundary}$$

For small supersaturations

$$\ln i \approx i - 1$$

$$\therefore i - 1 \approx \frac{\gamma a}{r_c kT} \quad \dots 21$$

$$\text{Similarly } i^1 - 1 \approx \frac{\gamma a}{r_c kT} \quad \dots 22$$

$$\text{Thus } i - i^1 = (i - 1) \left[ 1 - \frac{r_c}{r} \right] \dots 23$$

$$\text{and therefore } U_r = U \left[ 1 - \frac{r_c}{r} \right] \dots 24$$

During growth, the whole spiral can be considered to be rotating with angular velocity ( $\omega$ ) and thus the rate of growth,  $Y$ , of a crystal face will be given by

$$Y = \frac{\omega d}{2\pi} \quad \dots 25$$

where  $d$  is the step height and will be equal to the Burger's vector of the dislocation.

By calculating the form of such a spiral, Burton Cabrera and Frank were able to estimate  $\omega$  and found that for large values of  $r$ ,  $\omega \approx 0.63u/2r_c$

..... 26

Hence the growth rate  $Y$  can be written

$$Y = \frac{0.63 ud}{4\pi r_c} \quad \dots 27$$

Now from equation 21,  $\frac{1}{r} \propto j$  (the supersaturation)

and also from equation 8,  $U \propto j$

Hence from equation 27 it is clear that

$$Y \propto j^2 \quad \dots 28$$

In this derivation it is important to bear in mind the assumptions which have been made. In fact this relationship is only valid in cases where the spacing between steps is such that competition for arriving atoms can be neglected. This is the low supersaturation case. The rigorous treatment of growth spirals predicts a parabolic growth rate  $Y \propto j^2$  at low supersaturations but also predicts that at higher supersaturations there is a transition to a linear  $Y \propto j$ , growth rate dependence.

So far, the growth of a crystal face due to a single screw dislocation has been considered. In fact, the growth rate is found to be largely independent of the number of dislocations, except at very high densities. This is because the number and curvature of the steps on a surface is only slightly modified by the numbers and nature of the dislocations which generate them.

Considerable experimental evidence has been accumulated in support of the dislocation mechanisms of crystal growth. As well as evidence confirming the predicted dependence of growth rate on supersaturation, some elegant light microscopy has revealed directly the presence of growth spirals (12, 13).

#### 4.2.5 The twin plane re-entrant edge mechanism

The island nucleation model and the screw dislocation model both described the growth process in terms of the generation of a step followed by its subsequent propagation. For certain crystals, however,

other mechanisms of step generation may be more important. In the growth of some crystals new growth layers can originate at a twin plane re-entrant edge. Several observations of crystals which grow by this mechanism have been reported by for example Wagner (14) and Faust and John (15, 16).

The twin plane re-entrant edge (TPRE) provides a line of favourable sites at which atoms can become attached (Fig. 4.4 (1)). The attachment of atoms at such sites initiates the growth of new layers on each of the re-entrant twin faces. Thus the crystal will grow in the direction of propagation of the twin plane.

Assume initially that each re-entrant face of the twinned crystal is perfectly smooth. As atoms arrive at the surface they will diffuse and re-evaporate. On average all the atoms arriving within a distance  $X_s$  of the TPRE will diffuse to these sites and a fraction  $\beta^1$  will become attached. In this way all the sites along the TPRE will rapidly be occupied.

Atoms arriving at the crystal surface will now result in the growth of layers by the step growth process already described.

Once new layers have been established as shown in Figure 4.4 (2) then some of the atoms arriving on these layers may be captured at the freshly generated TPRE sites, initiating yet another new layer on each of the twin faces.

The establishment of such a new layer will depend on the size which the previous layers have attained. Consider the case where addition of atoms to the TPRE sites occurs readily and new growth layers are generated at regular intervals.



Fig. 4.4. Growth by the TPRES mechanism.

Fig. 4.4

Growth by the TPRE mechanism

The re-entrant edge formed by the intersection of two twin related crystals provides a line of favourable sites for the attachment of new growth units. Under appropriate conditions of supersaturation some of these re-entrant edge sites become occupied (a) forming a nucleus for the growth of new layers on each of the twin related faces. These new growth layers quickly extend regenerating the re-entrant edge (b). Eventually a further growth layer can nucleate as shown in (c).

A sectional view (d) shows the first five growth layers to form and illustrates the propagation of the twin boundary.



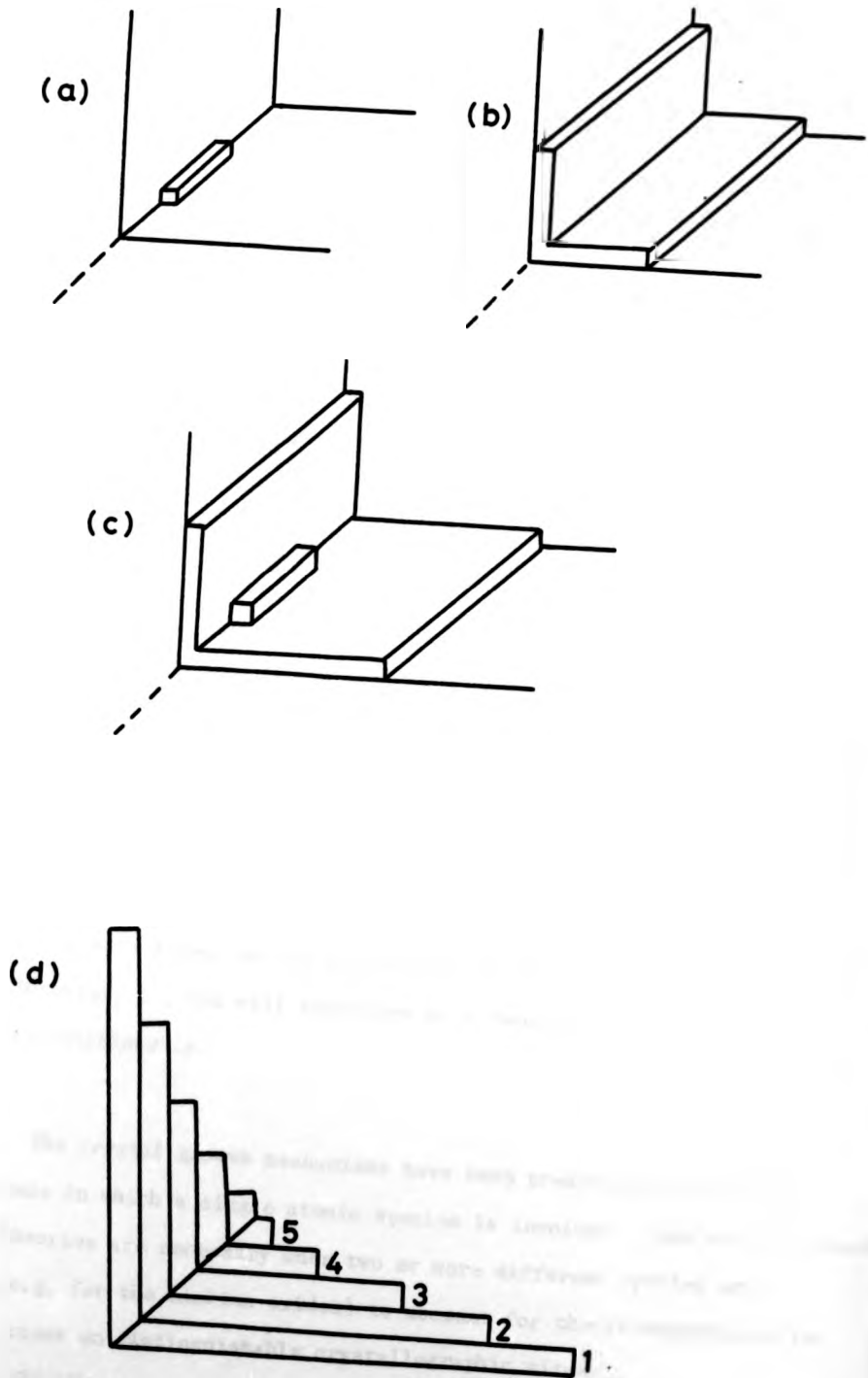


Fig. 4.4. Growth by the TPRES mechanism.

Assume that the first layer grows a distance  $x_1 < x_s$  before the next new layer is initiated. As this new layer grows, it will be in competition with both the TPRES and the previous layer and will grow more slowly. Thus this new layer will grow to a distance  $x_2 < x_p$  before a third layer nucleates. Eventually after a few new layers have been initiated an equilibrium situation will be reached. In this condition a new layer will be initiated after the previous layer has grown to a size  $x_e < x_s$ . Thus the rate of propagation,  $T$ , of the twin plane in this situation will be given by:

$$T = \frac{d}{\sin} \frac{U}{x_e} \quad \dots 29$$

$d$  is the step height

$U$  is the growth rate of a step when distance between steps is  $x_e$ . (Equation 9)

From Equation 9:

$$U \propto j \text{ (the supersaturation)}$$

and therefore:

$$T \propto j$$

$x_e$  will depend on the probability of atoms becoming attached to the TPRES sites,  $\beta^1$ , and will therefore be a function of the geometry of the twin relationship.

Note:

The crystal growth mechanisms have been presented here for the simplest case in which a single atomic species is involved. Some modifications to these theories are necessary when two or more different species are involved (e.g. for the niobium oxides) to account for the arrangement of the different atoms on distinguishable crystallographic sites.

Growth mechanisms such as the vapour-liquid-solid (V.L.S.) mechanism have not been discussed since such processes are not applicable to the chemical transport growth of niobium oxides.

The V.L.S. mechanism (34) requires the presence of a liquid phase which acts as a solvent from which the solute is deposited as a single crystal.

#### 4.2.6 Comparison of the various growth theories

Several mechanisms for the growth of crystals from the vapour have been described and in each case the form of dependence of growth rate on supersaturation has been discussed. In some crystal systems competition between these various mechanisms may occur and by varying the supersaturation different growth mechanisms can dominate the growth. Indeed, often the growth in different directions in the same crystal can occur by different mechanisms.

Figure 4.5 illustrates graphically the dependence of growth rate on supersaturation for a hypothetical crystal.

Consider growth at low supersaturations. The 2-d nucleation mechanism cannot operate under these conditions.

For a suitably rough exposed crystal surface, the continuous growth mechanism may be expected to dominate. If however a high index stepped surface were exposed the step growth mechanism would apply. This could only normally be a transient growth mode, however, since the high index surfaces required would quickly grow out, resulting in a faceted crystal with smooth low index faces.

If a suitable twinning relationship exists for the crystal and a twin is nucleated with a re-entrant edge, the TPPE mechanism may become the most favourable. If such a twinning relationship does not exist, growth may occur by the spiral dislocation mechanism.

#### 4.2.6 Comparison of the various growth theories

Several mechanisms for the growth of crystals from the vapour have been described and in each case the form of dependence of growth rate on supersaturation has been discussed. In some crystal systems competition between these various mechanisms may occur and by varying the supersaturation different growth mechanisms can dominate the growth. Indeed, often the growth in different directions in the same crystal can occur by different mechanisms.

Figure 4.5 illustrates graphically the dependence of growth rate on supersaturation for a hypothetical crystal.

Consider growth at low supersaturations. The 2-d nucleation mechanism cannot operate under these conditions.

For a suitably rough exposed crystal surface, the continuous growth mechanism may be expected to dominate. If however a high index stepped surface were exposed the step growth mechanism would apply. This could only normally be a transient growth mode, however, since the high index surfaces required would quickly grow out, resulting in a faceted crystal with smooth low index faces.

If a suitable twinning relationship exists for the crystal and a twin is nucleated with a re-entrant edge, the TPPE mechanism may become the most favourable. If such a twinning relationship does not exist, growth may occur by the spiral dislocation mechanism.

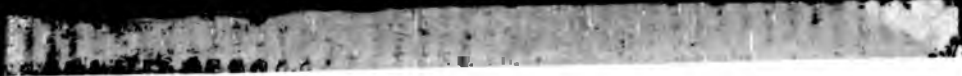


Figure 1. Correlation of the dependence of growth rate on population for the various growth mechanisms.

Fig. 4.5

Comparison of the dependence of growth rate on supersaturation for the various growth mechanisms

The continuous growth model predicts a growth rate proportional to the supersaturation (i.e.  $U \propto j$ ). Since this theory is based on the assumption that all atoms arriving at the growing surface become attached, it represents a maximum obtainable growth rate. In practice this theory does not apply to growth from the vapour but is included here for comparison.

Both the step growth model and the twin plane re-entrant edge model (TPRE) predict growth rates proportional to supersaturation ( $U \propto j$ ).

Dislocation assisted growth has a parabolic dependence of growth rate on supersaturation (i.e.  $U \propto j^2$ ).

Finally the island nucleation model predicts an extremely low probability of growth until some threshold supersaturation is exceeded. Once this occurs the growth rate rises dramatically.

The relative slopes and positions of the curves will depend on the particular crystal species under consideration. The dominant growth mechanism will depend on which mechanisms can operate, the relative positions of the curves and the supersaturation.

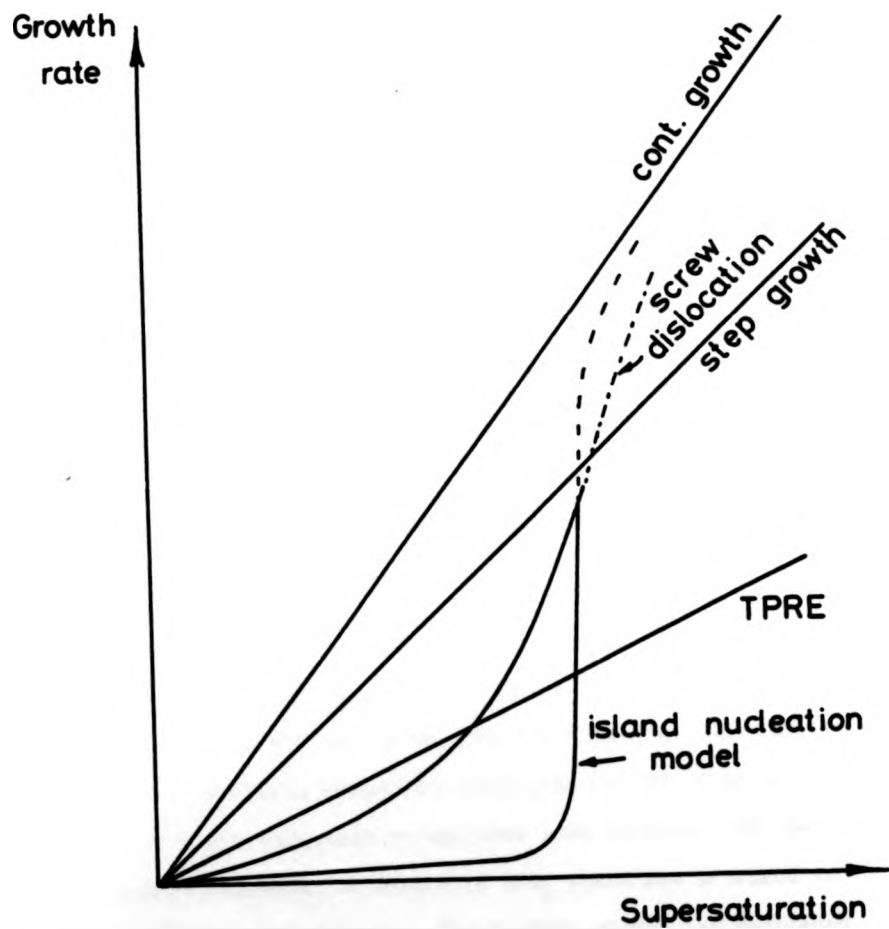


Fig. 4.5. Comparison of the dependence of growth rate on supersaturation for the various growth mechanisms.



The diagram shows that at higher supersaturations a different behaviour would be expected. It is interesting to note that since the spiral dislocation theory depends on the propagation of steps it cannot exceed the growth rate predicted by the step growth mechanism.

Similarly the 2-d nucleation model cannot exceed the growth rate predicted by the continuous growth theory.

#### 4.3 The Growth Habits of the Niobium Oxides

The shape of the crystals produced by chemical transport will depend on the crystallography of the particular species and on the dominant growth mechanisms. For each of the crystal types produced, experimental observations of the growth habits of the crystals and surface features are presented and in each case this evidence is discussed in terms of the theories of growth outlined above.

##### 4.3.1 $\text{Nb}_{12}\text{O}_{29}$ crystals

$\text{Nb}_{12}\text{O}_{29}$  can exist in two allotropic forms (17, 18), an orthorhombic type and a monoclinic type. Fig. 4.6 (a), (b) show schematically the [010] projections of the two structures and illustrate the similarities between them. The generally accepted conventions for the diagrammatic representation of block structure oxides have been adopted. The darker and lighter squares represent octahedra of  $\text{NbO}_6$  which are arranged in blocks of (4 x 3) by corner sharing. The lighter blocks are displaced by a distance  $b/2$  ( $\approx 1.9 \text{ \AA}$ ) along the b-axis. The simpler block convention is also depicted.

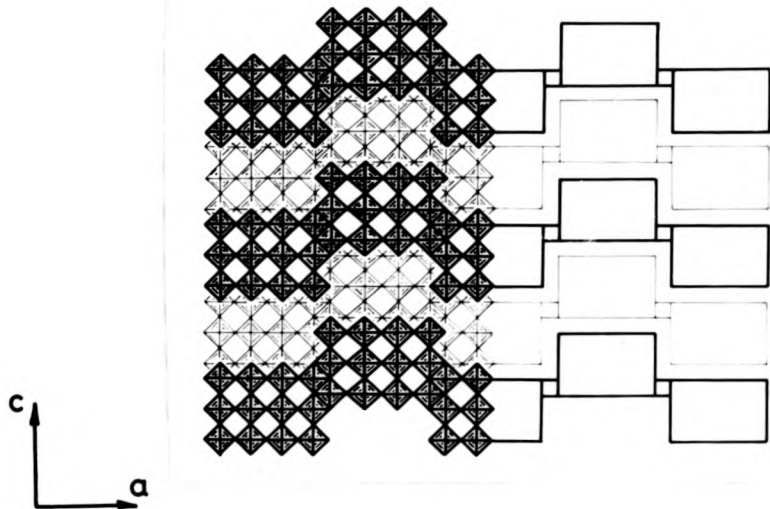
The majority of the crystals which were grown in these experiments were identified by X-ray and electron diffraction as the orthorhombic modification.

Fig. 4.6

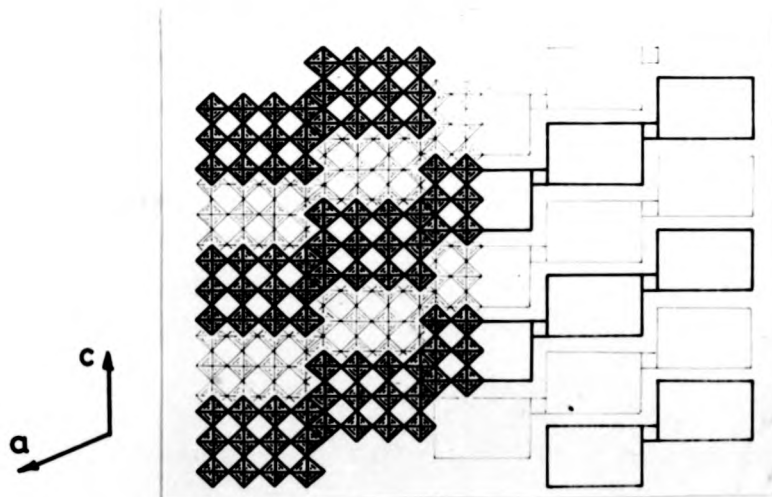
The structures of the two forms of  $\text{Nb}_{12}\text{O}_{29}$

The orthorhombic (a) and the monoclinic (b) modifications of  $\text{Nb}_{12}\text{O}_{29}$  are depicted schematically using the two standard schematic conventions. In each case the  $[010]$  projection of the structure is depicted (i.e. along the columns). The small shaded squares represent individual  $\text{NbO}_6$  octahedra. The darker octahedra are all centred on the same plane, and are arranged in blocks of  $(4 \times 3)$ . The lighter shaded squares represent a similar layer of octahedra displaced along the  $b$ -axis by half a unit cell.

The open rectangle structure (right hand side) shows a simpler representation of the  $(4 \times 3)$  octahedra.



(a) Orthorhombic Nb<sub>12</sub>O<sub>29</sub> [010] projection



(b) Monoclinic Nb<sub>12</sub>O<sub>29</sub> [010] projection

Figure 4.6 The structures of the two forms of Nb<sub>12</sub>O<sub>29</sub>

The crystals grew in the form of blue-black needles or platelets. Fig. 4.7 is a light micrograph of a typical  $\text{Nb}_{12}\text{O}_{29}$  platelet crystal. The use of polarised illumination clearly reveals the presence of twin related regions. The orientation of the plates was determined by the standard Lane back-reflection technique (Fig. 4.8). The results of this examination confirmed the findings of Sakata et al. (19) and verified that the principal growth direction for these crystals is parallel to the b-axis and that the platelets are bounded by  $\{100\}$  type faces.

Fig. 4.9 is a diagrammatic representation of the orthorhombic  $\text{Nb}_{12}\text{O}_{29}$  structure showing the arrangement of  $(4 \times 3)$  blocks of  $\text{NbO}_6$  octahedra. These diagrams clearly show that the surface which is responsible for growth in the  $[010]$  direction has a stepped surface. In fact the arrangement of the structural blocks is such that the surface consists of a regular array of steps each of which having a height equivalent to half that of a complete  $\text{NbO}_6$  octahedron. During the growth process, the edges of the blocks behave as a type of step site and at the corners of blocks are positions analogous to kink sites. Fig. 4.10 shows the  $(100)$  projection of the  $\text{NbO}_6$  octahedra at the growing surface of a crystal. The black dots on this diagram indicate the favourable sites for attachment of Nb atoms.

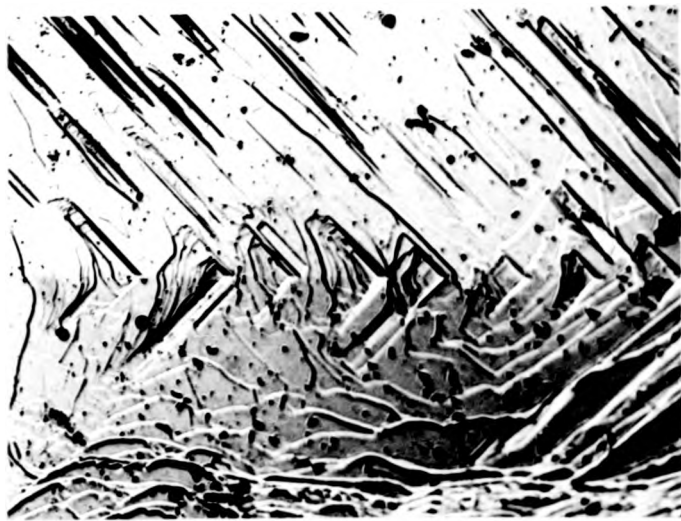
Fig. 4.7

Twinning in Nb<sub>12</sub>O<sub>29</sub>

This micrograph was taken in reflected polarised light using a Zeiss Ultraphot microscope. The specimen, a Nb<sub>12</sub>O<sub>29</sub> platelike crystal, as grown, was viewed perpendicular to the plate surface (i.e. in the [001] direction).

Fig. 4.8

Laue back reflection pattern obtained from one branch of the twinned crystal. The principal growth direction is indicated and analysis of the pattern confirms that it is the [010] direction.



100  $\mu\text{m}$

Figure 4.7 Twinning in  $\text{Nb}_{12}\text{O}_{29}$  (polarised light)

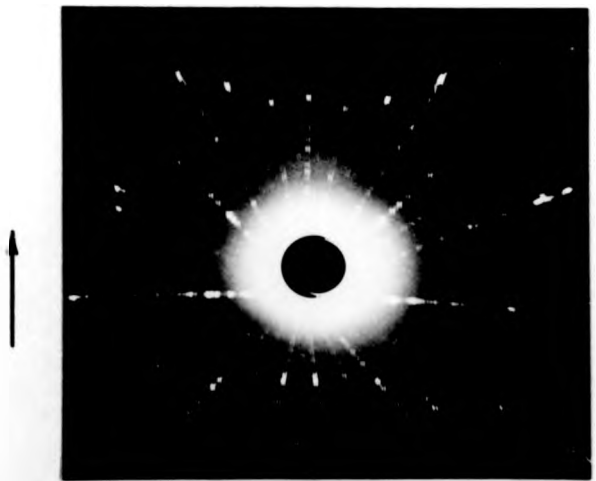


Figure 4.8 Laue back reflection pattern obtained from one branch of the twinned crystal. The principal growth direction is indicated.

Surface Steps on Nb<sub>12</sub>O<sub>29</sub>

This diagram depicts the stacking arrangement of the (4 x 3) blocks of NbO<sub>6</sub> octahedra for the ortho-Nb<sub>12</sub>O<sub>29</sub> structure.

Because successively layers are displaced in the b-axis direction by  $b/2$ , the surface consists of a network of steps. The linkage between adjacent blocks in the same layer results in kinks in these steps as shown.

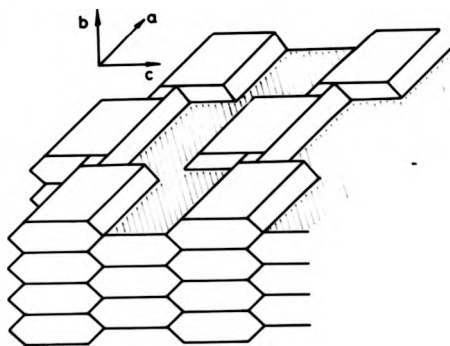


Figure 4.9 Schematic diagram of the Nb<sub>12</sub> O<sub>29</sub> block structure showing the stepped nature of the (010) face.



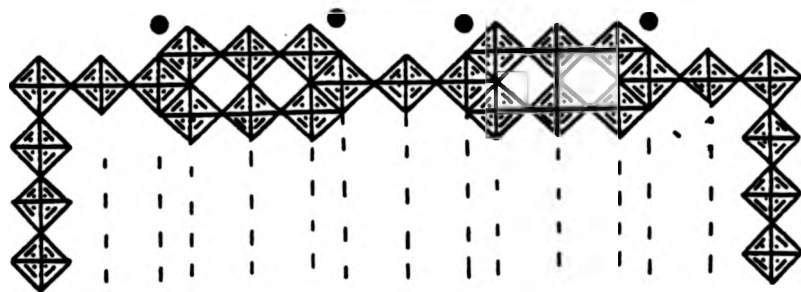


Fig. 4.10. The positions of preferred sites for growth in the [010] direction.

This diagram represents a (100) section of an  $\text{Nb}_{12}\text{O}_{29}$  crystal at the growing interface. The black dots indicate the most favourable "step" on the growing surface.

This diagram suggests that new layers will prefer to grow on blocks which are bounded by at least one raised block.

This growth mechanism is very similar to the growth of a stepped face described in 4.3.2. However in this case the steps are an intrinsic feature of the crystal structure. The essential difference between growth in this case and the growth of a normal high index stepped surface is that the steps on the surface of the  $\text{Nb}_{12}\text{O}_{29}$  crystals are regenerated during growth and do not become exhausted. The dominant nature of the growth in this direction demonstrates the effectiveness of this mechanism.

Some of the crystals which grew in this way developed (011) facets on the growing surface as shown in Fig. 4.11 (a). Fig. 4.11 (b) shows schematically the arrangement of  $\text{NbO}_6$  octahedra at such a surface. Generally crystals with these facets resulted from experiments in which low levels of  $\text{TeCl}_4$  were used. In these cases, because of the exhaustion of the  $\text{TeCl}_4$  during the reaction, the final transport rate would have been low and the supersaturation would have been correspondingly low. Crystals grown at higher supersaturations showed little or no tendency to form these facets.

The formation of facets can be explained if it is assumed that at low supersaturations, the blocks with the highest density of step sites have a greater probability of forming a new layer. Fig. 4.12 shows how an initially non-faceted interface might develop based on this assumption. Because the blocks at the edges of the crystal are never completely surrounded by ledge sites, they will tend to grow at a slower rate than other blocks in the centre of the face.

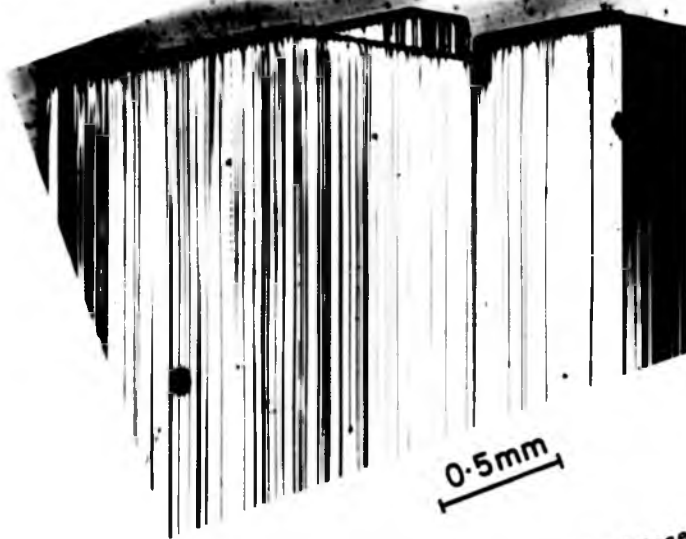


Figure 4.11 (a) Well-developed  $\{011\}$  facets in  $\text{Nb}_{12}\text{O}_{29}$  crystals.

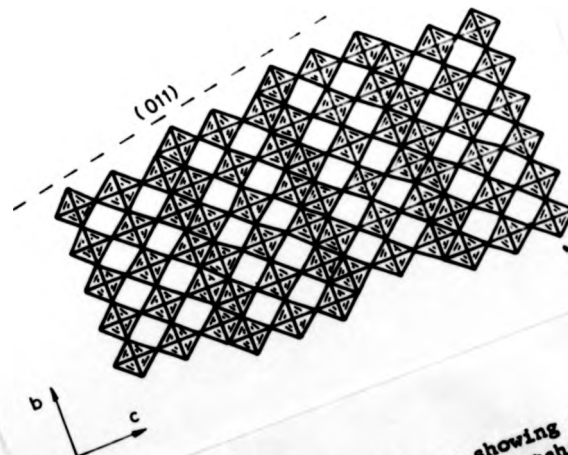


Figure 4.11 (b) Schematic diagram showing the arrangement of  $\text{NbO}_6$  octahedra at  $\{011\}$  facets.

Fig. 4.12

The development of {011} facets in  $\text{Nb}_{12}\text{O}_{29}$

(a) A simplified representation of a (100) section through the growing interface of a  $\text{Nb}_{12}\text{O}_{29}$  crystal (see Fig. 4.10). The most favoured positions for new blocks to develop are those which have step sites on each side. On the arbitrarily chosen interface depicted, these preferred growth sites are indicated and the new blocks dotted in place.

(b) With these new blocks in position, other favourable positions are created as indicated again by the dotted layers.

(c), (d) Addition of new blocks in this way eventually leads to the formation of the {011} facets.

Fig. 4.12

The development of  $\{011\}$  facets in  $\text{Nb}_{12}\text{O}_{29}$

(a) A simplified representation of a (100) section through the growing interface of a  $\text{Nb}_{12}\text{O}_{29}$  crystal (see Fig. 4.10). The most favoured positions for new blocks to develop are those which have step sites on each side. On the arbitrarily chosen interface depicted, these preferred growth sites are indicated and the new blocks dotted in place.

(b) With these new blocks in position, other favourable positions are created as indicated again by the dotted layers.

(c), (d) Addition of new blocks in this way eventually leads to the formation of the  $\{011\}$  facets.

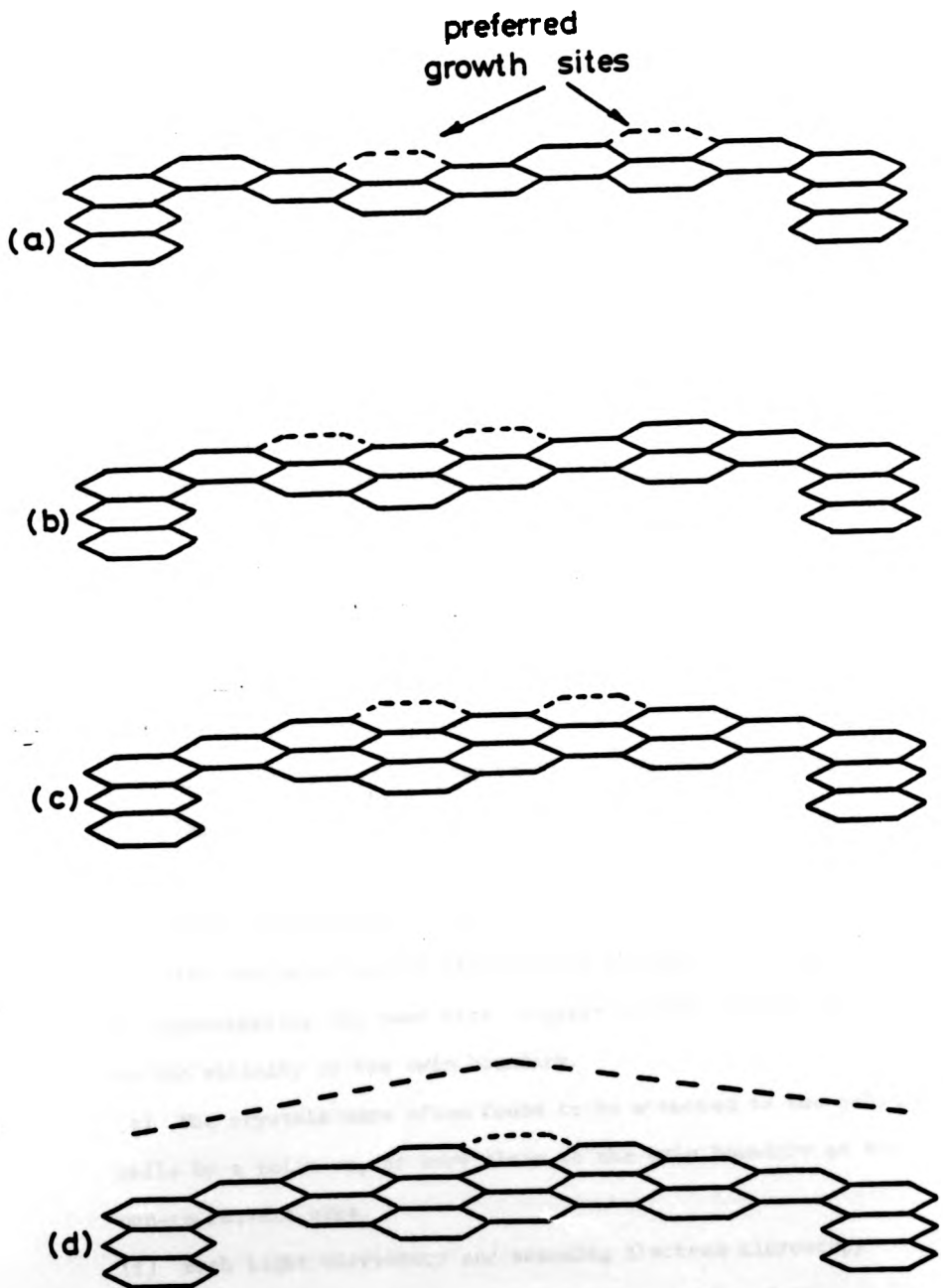


Fig. 4.12. The development of  $\{011\}$  facets.

So far the growth of  $\text{Nb}_{12}\text{O}_{29}$  crystals has only been discussed for the b-axis  $[010]$  direction. For the growth of needle shaped crystals this is sufficient. However, a large number of  $\text{Nb}_{12}\text{O}_{29}$  crystals grow in the form of thin plates. Therefore for a complete description of the growth of  $\text{Nb}_{12}\text{O}_{29}$  it is necessary to account for the growth in the directions other than  $[010]$ .

In every case the crystals which grew as platelets were observed to contain at least one twin boundary. Furthermore, examination of a number of crystals by polarised light microscopy indicated that the twin plane played an important role in the growth of the crystals. The evidence which suggests the importance of twinning in the growth of these crystals can be summarised as follows:-

- (a) With the exception of the fine needle shaped crystals, all the crystals examined contained at least one twin boundary.
- (b) Occasional small twinned regions were observed, but in general the crystals contained one principal twin boundary which extended across the whole crystal.
- (c) This principal twin boundary was always straight and invariably coincided with the thickest part of the crystal.
- (d) The two twin related regions were normally observed to be of approximately the same size, suggesting that growth originated in the vicinity of the twin boundary.
- (e) The crystals were often found to be attached to the substrate walls by a point on, or very close to the twin boundary at the non-re-entrant edge.
- (f) Both light microscopy and scanning electron microscopy revealed the presence of growth features emanating from the twin plane re-entrant edge.

So far the growth of  $\text{Nb}_{12}\text{O}_{29}$  crystals has only been discussed for the b-axis [010] direction. For the growth of needle shaped crystals this is sufficient. However, a large number of  $\text{Nb}_{12}\text{O}_{29}$  crystals grow in the form of thin plates. Therefore for a complete description of the growth of  $\text{Nb}_{12}\text{O}_{29}$  it is necessary to account for the growth in the directions other than [010].

In every case the crystals which grew as platelets were observed to contain at least one twin boundary. Furthermore, examination of a number of crystals by polarised light microscopy indicated that the twin plane played an important role in the growth of the crystals. The evidence which suggests the importance of twinning in the growth of these crystals can be summarised as follows:-

- (a) With the exception of the fine needle shaped crystals, all the crystals examined contained at least one twin boundary.
- (b) Occasional small twinned regions were observed, but in general the crystals contained one principal twin boundary which extended across the whole crystal.
- (c) This principal twin boundary was always straight and invariably coincided with the thickest part of the crystal.
- (d) The two twin related regions were normally observed to be of approximately the same size, suggesting that growth originated in the vicinity of the twin boundary.
- (e) The crystals were often found to be attached to the substrate walls by a point on, or very close to the twin boundary at the non-re-entrant edge.
- (f) Both light microscopy and scanning electron microscopy revealed the presence of growth features emanating from the twin plane re-entrant edge.



From this evidence it would appear that the observed twin planes nucleated at a very early stage of the growth process and it is probably at this stage that the form of the crystal is determined. If a twin plane is nucleated, then the crystal will subsequently develop as a plate; otherwise the crystal will grow as a needle.

The TPRE mechanism is obviously important in the development of  $\text{Nb}_{12}\text{O}_{29}$  crystals as plates. In  $\text{Nb}_{12}\text{O}_{29}$ , the twinning plane has been determined as the (015) plane. Fig. 4.13 is a schematic diagram of such a twin indicating a possible arrangement of  $\text{NbO}_6$  octahedra in the vicinity of the twin interface. The re-entrant edge indicated in the diagram provides energetically favourable sites at which new growth layers can be initiated on the (001) planes. As a result of the TPRE mechanism, growth of the crystals occurs in the direction of propagation of the twin plane and it is this growth which results in the formation of platelike crystals.

To complete the discussion of the growth of  $\text{Nb}_{12}\text{O}_{29}$  crystals, it only remains to consider the way in which the plates increase in thickness (i.e. growth perpendicular to the plane of the plates). Again, there is evidence to suggest that the twin planes have an important role. Observations of the surface of the plates reveals the presence of active growth regions centred on the twin boundary. Fig. 4.14 shows some of these features and the ledges which are growing from such areas are typical of growth generated by the emergent dislocation mechanism. Therefore, it would appear that the twin planes are often associated with dislocations. Scheel and Elwell (20) have reported a similar association between growth hillocks and twin boundaries in flux grown crystals of  $\text{NdAlO}_3$  and  $\text{GdAlO}_3$ .

The new layers of growth generated on the surface of the plates at the twin boundary sites rapidly spread over the crystal resulting in an overall thickening.

Fig. 4.13     A proposed arrangement for the NbO<sub>6</sub> octahedra at  
the twin plane in Nb<sub>12</sub>O<sub>29</sub>

The unit cell dimensions are indicated on the diagram and the twin plane can be indexed by inspection as (015).

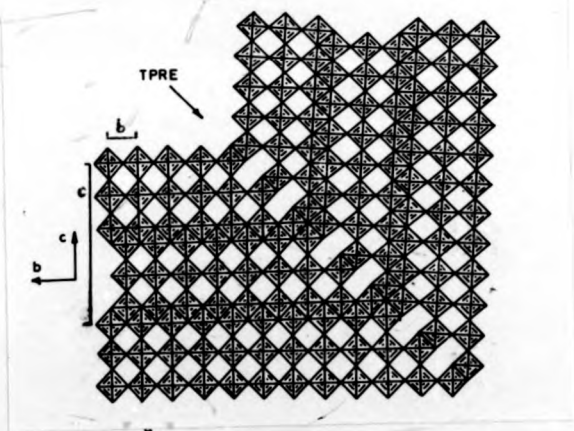


**Figure 4.13** A possible arrangement of the NbO<sub>6</sub> octahedra at the twin plane in Nb<sub>12</sub>O<sub>29</sub>

Fig. 4.14

Active growth centres along twin boundaries

This micrograph was taken using the Zeiss Ultraphot microscope. In this  $\text{Nb}_{12}\text{O}_{29}$  crystal the use of reflected polarised light reveals a number of twin related regions. The most active growth centres are associated with the twin boundaries.

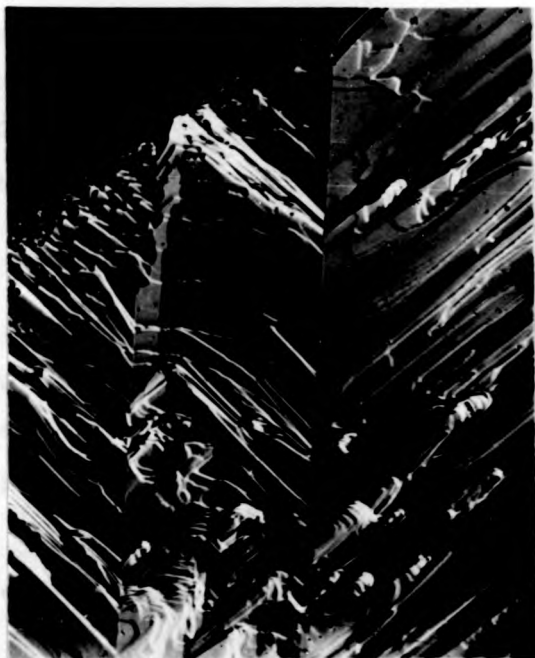


**Figure 4.14** Active growth centres along twin boundaries.

The growth of crystals of  $\text{Nb}_{12}\text{O}_{29}$  is governed by three distinct growth processes and a useful comparison of the relative effectiveness of these processes can be made. The dominant growth mechanism observed was by the propagation of steps, the steps being continually regenerated as a result of the crystal structure. Growth by the TPPE mechanism was almost as effective and in general the crystal plates were almost as wide as they were long. The dislocation generated growth which resulted in a thickening of the plates was very much less effective and plate crystals with areas of about  $1 \text{ cm}^2$  were often less than 0.5 mm in thickness.

Reference to Fig. 4.5 shows that the predicted comparative growth rates for a given low supersaturation agree well with the observations.

#### 4.3.2 Niobium dioxide crystals

Above about  $800^\circ\text{C}$ ,  $\text{NbO}_2$  has a rutile type structure with a tetragonal unit cell having  $a = 4.85 \text{ \AA}$  (21)  
 $c = 2.99 \text{ \AA}$

At temperatures below  $800^\circ\text{C}$  the structure is modified. A periodic distortion of the ideal rutile structure results in a tetragonal unit cell of increased periodicity (22) with  $a = 13.71 \text{ \AA}$   
 $c = 5.985 \text{ \AA}$

A more detailed description of these structures and the relationship between them is included in the next chapter.

Crystals of  $\text{NbO}_2$  were produced in two different ways and the crystals which resulted showed considerable differences in their external appearance. When  $\text{NbO}_2$  powder was used as the starting material well formed octahedral crystals of  $\text{NbO}_2$  could be grown along with the  $\text{Nb}_{12}\text{O}_{29}$  crystals. This technique was first used to prepare  $\text{NbO}_2$  crystals by Sakata et al. (19). However if powdered  $\text{NbO}$  is used as the starting material, crystals of  $\text{NbO}_2$  are produced which take the form of multiply

twinned crystals with less well developed facets.

Consider first the crystals obtained by chemical transport with  $\text{NbO}_2$  powder as the starting material. Sakata et al. (19) reported that the octahedral crystals which were obtained in their experiments were limited by faces of (101) and (011) families. Kodama and Goto (23, 24) grew similar crystals using a variety of transport reagents and on the basis of their observations suggested that the crystal habit may be a function of the chemical transport reagent which is used. They observed crystals having  $\{111\}$  and  $\{110\}$  faces in some cases and  $\{111\}$  and  $\{101\}$  in others. In the experiments reported here, crystals have been observed with faces of  $\{101\}$ ,  $\{111\}$  and  $\{110\}$  types. Fig. 4.15 is an S.E.M. micrograph of a typical crystal showing the various types of facet.

Close examination of the surfaces of these crystals using the S.E.M. revealed the presence of a number of triangular depressions (Fig. 4.16 (a), (b), (c)). The spiral nature of many of these features indicates an association with emergent screw dislocations. However, normally dislocation stimulated growth is characterised by hillocks or raised spirals.

The similarity between these depressions and the more familiar etch pits observed in many materials suggests that these features may arise as a result of a vapour etching process which occurs after the normal vapour growth. However although the composition of the vapour phase is changing during the growth process it would seem to be unlikely that the conditions could change sufficiently for crystals which were initially growing to begin to be etched.

To explain the origin of depressions during the growth of the crystals it is necessary to reconsider the screw dislocation mechanism of



1mm

**Figure 4.15** S.E.M. micrograph of "octahedral"  
NbO<sub>2</sub> crystals





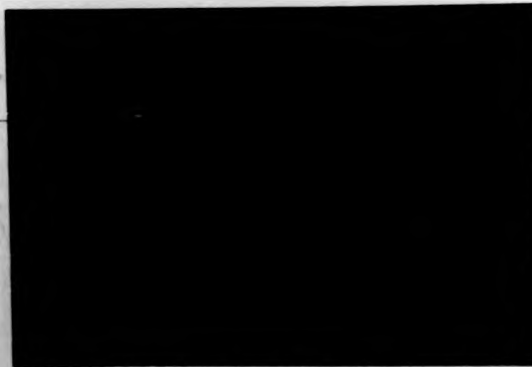
10  $\mu\text{m}$

(a) Spiral depression



100  $\mu\text{m}$

(b) Growth pits on {111} face



10  $\mu\text{m}$

(c) Arrays of pits along low angle boundaries

**Figure 4.16** S.E.M. micrographs of growth depressions in  $\text{NbO}_2$  crystals

crystal growth. In the simple treatment of the growth of steps generated by screw dislocations it was assumed that atoms would be equally likely to become attached to any part of the growth step. However, because of the distortion of the step near the core of the dislocation, the step sites in this vicinity may be less favourable. \*

This would mean that  $\beta$ , the fraction of atoms arriving at a step which become attached, would be a function of the distance from the dislocation core. Consider a crystal with an emergent screw dislocation for which  $\beta$  has a very small value near the dislocation core. The growth spiral will then develop as shown in Fig. 4.17. The cross-sectional view (Fig. 4.17 (d)) shows the resulting arrangement of steps on the surface more clearly. It is interesting to compare this series of diagrams with the simple case of screw dislocation growth (Fig. 4.3) in which only outward growing steps are generated.

In Fig. 4.17 it is clear that the steps spreading out from the dislocation can become widely spaced. However the inward growing steps will become closely spaced and will compete for arriving atoms. Thus one might expect to observe steep sided depressions in the vicinity of dislocations.

To estimate the extent of such features it is first necessary to consider the region of the dislocation core at which the addition of atoms to step sites is less favourable. For a typical material the dislocation core region will be of the order of a few unit cells in diameter. For  $\text{NbO}_2$  this will have a value of a few nanometres. In fact the depressions which are observed for  $\text{NbO}_2$  crystals are on a much larger scale than this and typically have dimensions of the order of microns.

To explain this apparent discrepancy, the tendency of  $\text{NbO}_2$  crystals to develop low index facets must be taken into account. Consider the progress of successive inward growing steps. The first layer grows in

\* See note on following page

Note:

Another reason why the dislocation core region may be less favourable for growth may be the segregation of impurities to these sites. The occupation of the core sites by impurity atoms may prevent further additions at these sites.

Fig. 4.17

The development of "hollow" growth spirals

As in Fig. 4.3, this series of diagrams represents an advancing step on the surface of a crystal with an emergent screw dislocation. In this case, however, the assumption is made that the addition of atoms to the step sites in the vicinity of the dislocation core is prohibited.

The consequence of this assumption is that instead of the spiral rotating as growth proceeds, a tongue like new growth layer advances around the dislocation core.

The sectional view (d) illustrates the depression which develops centred at the dislocation core.

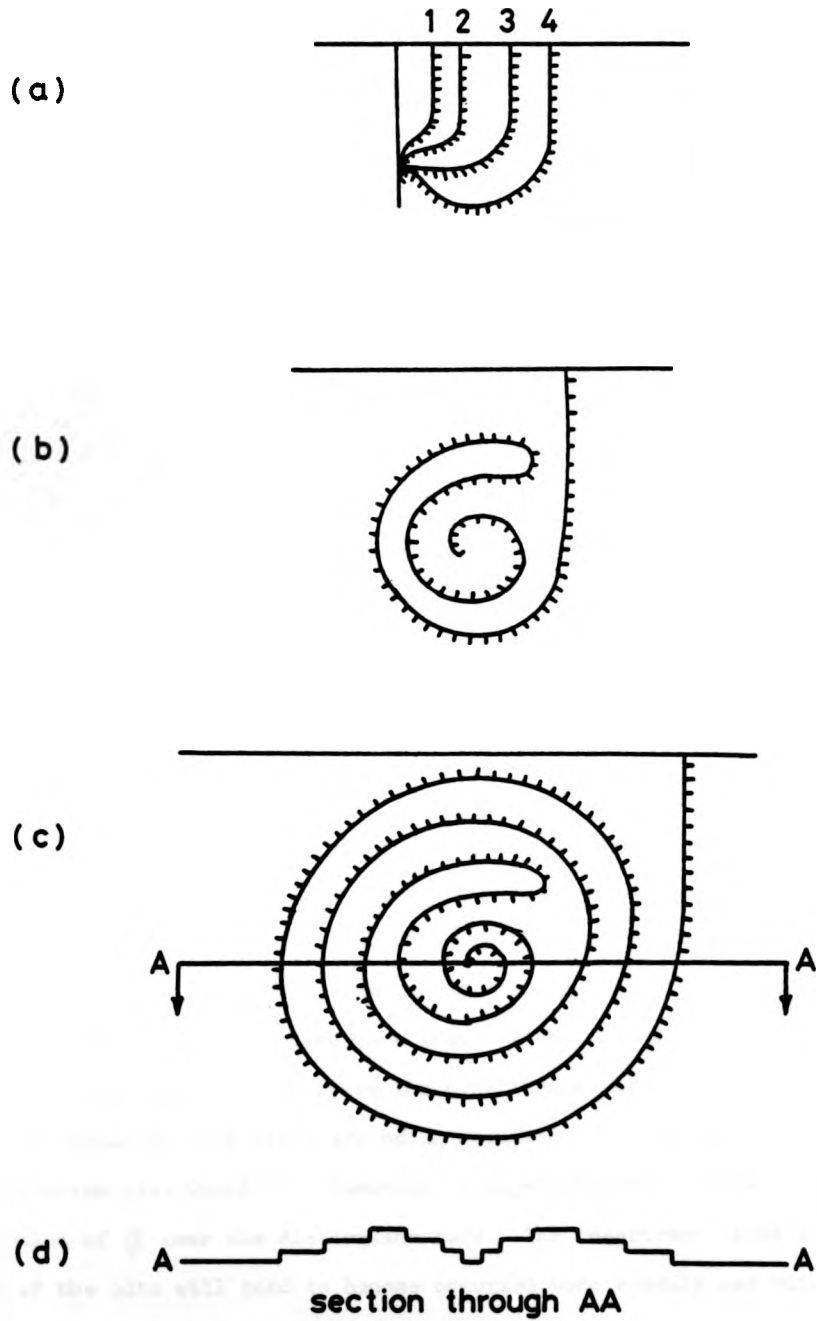


Fig. 4.17. The development of "hollow" growth spirals.

towards the dislocation core until its progress is hampered by the distortion of the step sites. The next layer which is generated will continue to grow inwards until it catches up with the first step. When a series of steps builds up in this way to form a larger multiple step, the advancing face generally takes up a low index configuration forming a facet. This process is shown diagrammatically in Fig. 4.18. In this way, although the unfavourable core region is only a few unit cells across, macroscopic pits can develop during growth.

The S.E.M. micrograph (Fig. 4.16) shows that the internal surfaces of the depressions correspond well to the low index facet planes of the crystal.

Except in cases where interaction between these growth features is occurring, it is noticeable that the majority of the growth depressions on a given crystal surface have similar dimensions (Fig. 4.6 (b)). This suggests that for a given set of growth conditions there is an equilibrium pit depth, otherwise a wide distribution of sizes would be expected.

In formulating this model it was assumed that near the dislocation core,  $\beta$ , the fraction of atoms arriving at step sites which become attached, was assumed to be very small. As the pit grows, however, an increased number of atoms will diffuse to these core sites and they may eventually become occupied. In this way a stable equilibrium will be established. Pits above the equilibrium size will capture more atoms at the core sites and will therefore shrink, whereas pits below the equilibrium size will grow at a faster rate than the core sites are being occupied. If this is the case, the equilibrium size would be a function of supersaturation and will depend on the value of  $\beta$  near the dislocation core. The re-entrant sites at the corners of the pits will tend to become occupied more readily and this will also tend to restrict the size of these growth pits.

Fig. 4.18      The formation of faceted depressions during growth

Hollow growth spirals can be considered as a set of outward facing steps and a set of inward facing steps. (see Fig. 4.17 (d)). As atoms arrive, the inward facing steps will advance towards the dislocation core. Now because the core region is unfavourable it is likely that the growing steps will take up an energetically favourable low index configuration as shown.

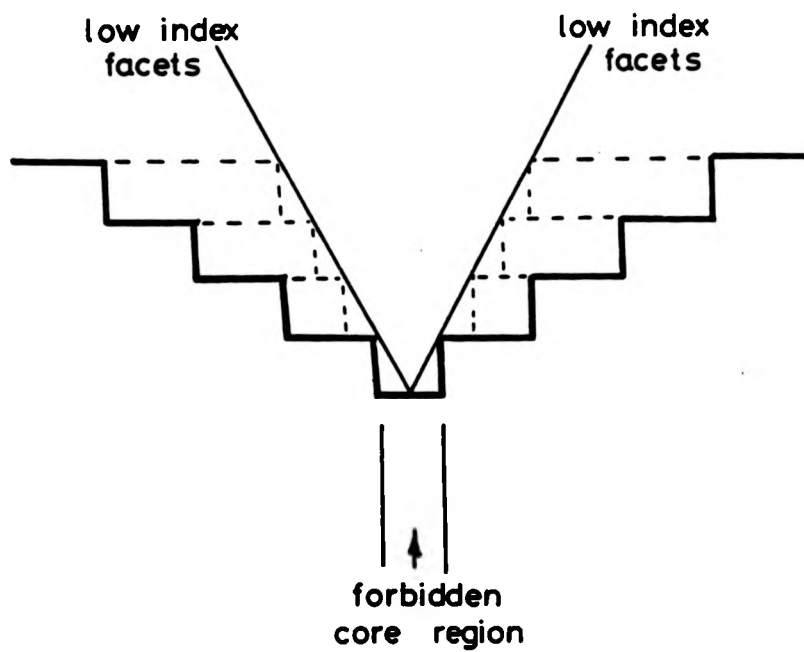


Fig. 4.18. The formation of faceted depressions during growth.



The model proposed here should be generally applicable to all dislocation induced crystal growth processes. The fact that growth pits are not generally observed suggests that in most materials the equilibrium pit size is negligibly small. This may be because near the dislocation core  $\beta$  is large enough to enable atoms to be captured before the pit develops or that the tendency to form facets is not sufficiently high to prevent the collapse of pits because of the re-entrant edge sites.

In several of the  $\text{NbO}_2$  crystals studied, arrays of these growth pits were observed (Fig. 4.16 (c)). Such an array of dislocations constitutes a low angle subgrain boundary and is probably generated by the intergrowth of two crystals which have a slight misorientation with respect to one another.

The other type of  $\text{NbO}_2$  crystals which were grown using  $\text{NbO}$  powder as the starting material invariably exhibited twinning. Each of the twin related branches of these crystals developed as elongated, tapered single crystals.

The principal growth axis of these crystals was established using the Laue diffraction technique. Fig. 4.19 shows the pattern obtained with the crystal oriented with the growth axis parallel to the X-ray beam. The streaking of the spots is due to the crystal being tapered. Comparison of this pattern with the computed [001] stereographic projection for the  $\text{NbO}_2$  structure (Fig. 4.20) shows that the preferred growth direction of the crystals is in fact parallel to [001.]

Many of the crystals consisted of just two twin related components as shown in Fig. 4.21 (a), (b). However several examples of multiply twinned crystals were also observed (Fig. 4.21 (c)). Measurement of the angles between the twin related components was carried out using the

Fig. 4.19

Laue pattern for determining the principal growth  
direction of NbO<sub>2</sub> crystals

An elongated NbO<sub>2</sub> crystal was mounted with its principal growth direction as near parallel as possible with X-ray beam direction. The resulting pattern was obtained by back reflection with the specimen to film distance set at about 3 cm. By indexing the principal reflections it was deduced that the growth direction of the needle shaped crystals was the [001].

Fig. 4.20

Computed [001] stereographic projection for NbO<sub>2</sub>

The indexing of the Laue pattern (Fig. 4.19) was facilitated by the use of the computed stereographic projection, used in conjunction with a Greninger net.

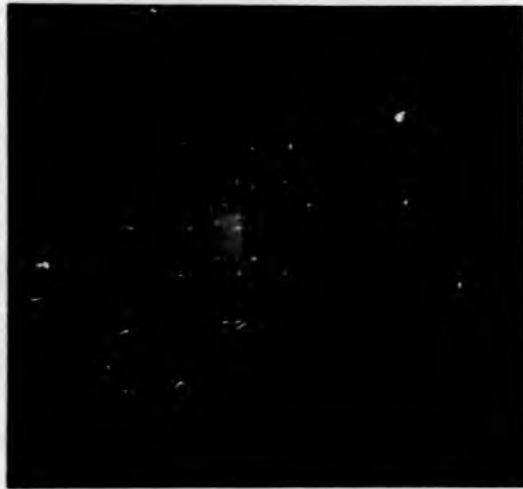


Figure 4.19 Laue pattern - taken parallel to the growth direction

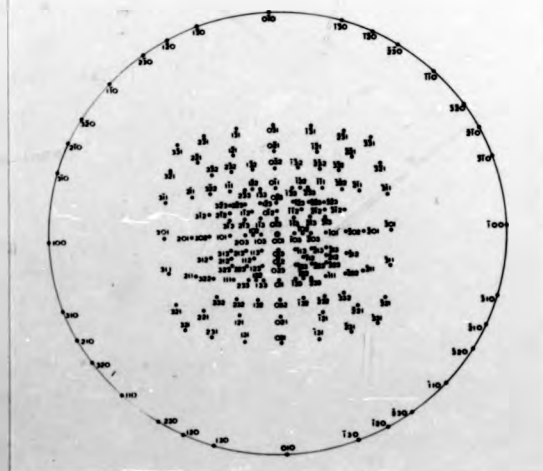


Figure 4.20 Computed [001] stereographic projection for  $\text{NbO}_2$

Fig. 4.21

S.E.M. micrographs showing twinned NbO<sub>2</sub> crystals

These micrographs were obtained using the Cambridge Stereoscan Mk II operating at 30 kV.

By using the tilting facilities it was possible to determine the angles between the twin related branches of the crystals and in this way the twin plane could be determined.

Thus (a) shows a  $(20\bar{1})$  twin

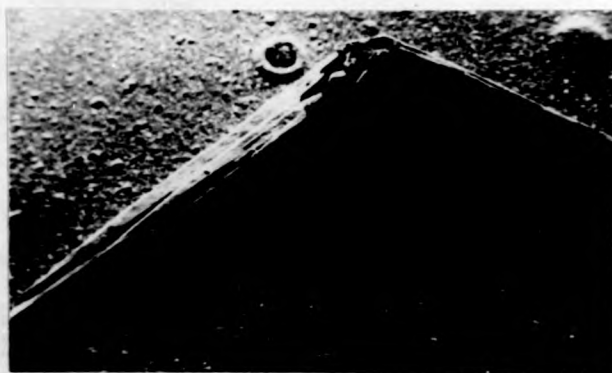
and (b) is a  $(10\bar{1})$  twin.

The crystal shown in (c) is multiply twinned.

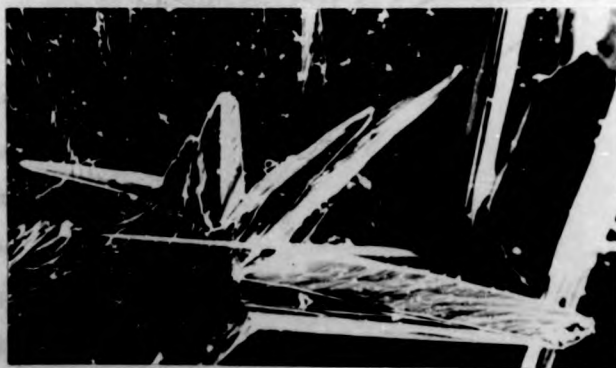
(a)



(b)



(c)



1mm

**Figure 4.21** S.E.M. micrographs showing twinned NbO<sub>2</sub> crystals

goniometer stage of the S.E.M. By comparing the measured angles with a computed list of interplanar angles the twinning relationships could be determined.

Fig. 4.22 shows schematically the two types of twins which were observed. As in the case of  $Nb_{12}O_{29}$  crystals there is strong evidence to suggest that the TPRES growth mechanism is important in the growth of these  $NbO_2$  crystals. Fig. 4.23 (a) and (b) are S.E.M. micrographs of the two types of twin boundaries and show the new growth layers originating at the re-entrant edge.

It is interesting to note that in these  $NbO_2$  crystals the twinning relationship is such that as growth progresses the TPRES increases in size. This is in marked contrast to the case of  $Nb_{12}O_{29}$  in which the TPRES is bounded by a pair of parallel facet planes and is constrained to remain the same size during growth. The differences between the TPRES mechanism in  $Nb_{12}O_{29}$  and in  $NbO_2$  are shown diagrammatically in Fig. 4.24. As indicated in this diagram the twinned components of these  $NbO_2$  crystals often develop  $\{110\}$  facets on the non-re-entrant surfaces. The absence of similar facets on the re-entrant surfaces is a consequence of the continuous generation of new growth layers at the TPRES. This also accounts for the tapering of the crystals away from the twin boundary.

To explain the differences in growth habit of the  $NbO_2$  crystals grown in the two different ways it is important to discuss the growth conditions in each case. The "octahedral" crystals grew during a transport reaction in which the principal product was  $Nb_{12}O_{29}$ . In fact it is likely that these  $NbO_2$  crystals nucleated and grew towards the end of the process when a proportion of the transport reagent had been consumed. Consequently, the effective supersaturation during the growth of these crystals would have been relatively low. However the crystals which were grown during chemical

Fig. 4.22

Twinning in NbO<sub>2</sub>

These two schematic diagrams illustrate the arrangement of the tetragonal, NbO<sub>2</sub>, unit cells at the two types of twin boundary.

In each case the growth direction of the twin branches is [ 001 ] .

The angle between the twin related branches as depicted in this diagram matches the angles between the twinned crystals illustrated in Fig. 4.21 and also Fig. 4.23.

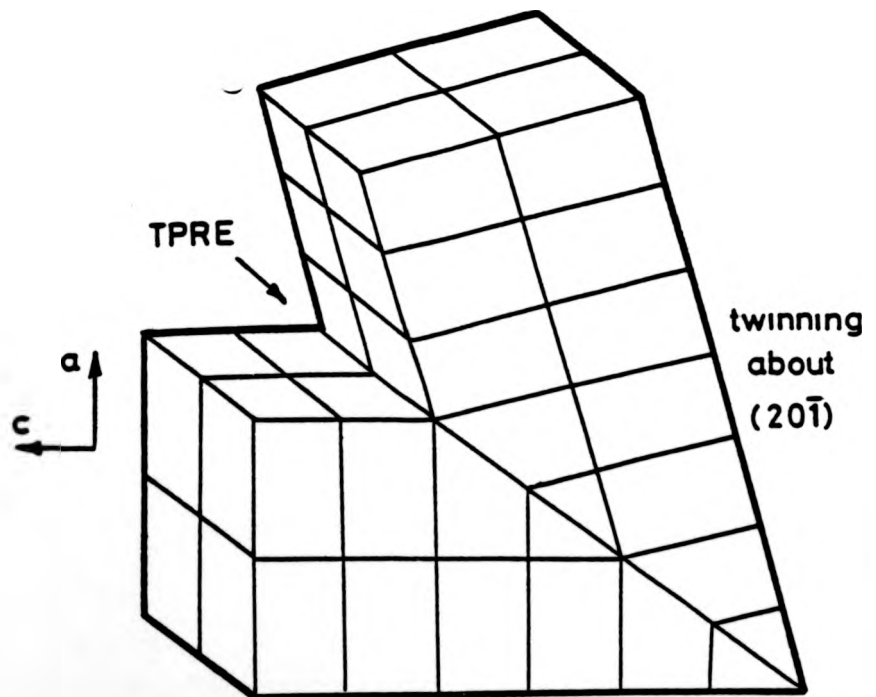
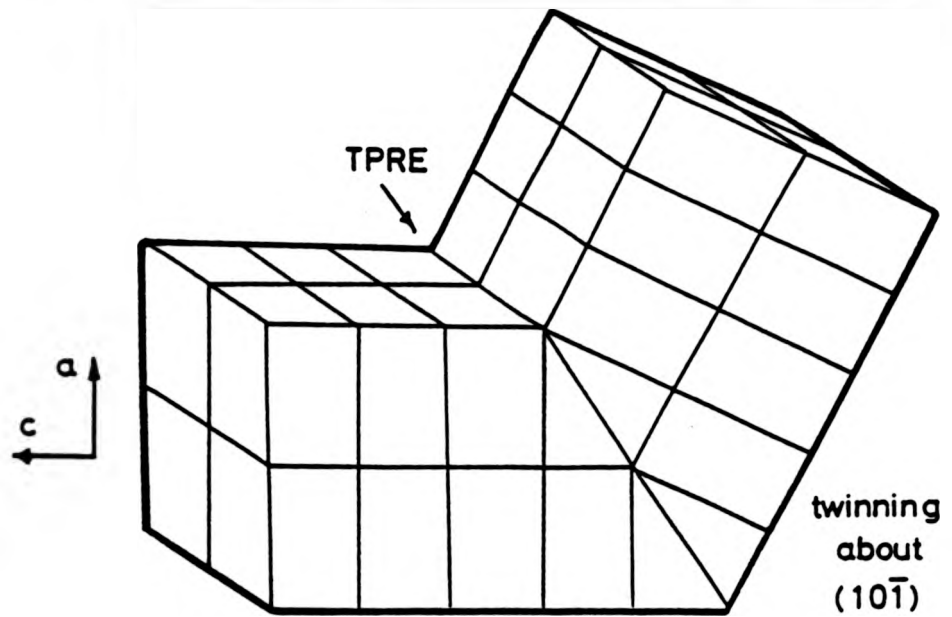


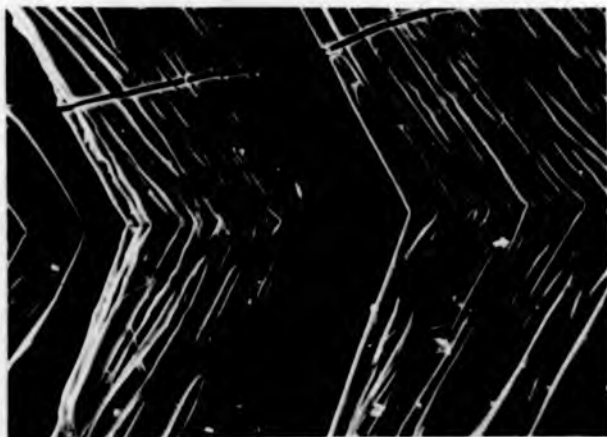
Fig. 4.22. Twinning in  $\text{NbO}_2$



Fig. 4.23

An S.E.M. micrograph showing the surface detail at the twin plane re-entrant edges of the NbO<sub>2</sub> crystals

The extended surface features which emanate from the twin interface clearly indicate the principal growth direction, which has been determined as  $[001]$ . The continued nucleation of new growth at the re-entrant edges means that these edges do not coincide with the growth direction.



50  $\mu\text{m}$

(a)  $(10\bar{1})$  twin plane



50  $\mu\text{m}$

(b)  $(10\bar{2})$  twin plane

**Figure 4.23** S.E.M. micrographs of twin interfaces in  $\text{NbO}_2$  crystals for comparison with Fig 4.22

Fig. 4.24

Twin plane re-entrant edge growth of

- (a) Nb<sub>12</sub>O<sub>29</sub> crystals  
and (b) NbO<sub>2</sub> crystals

In the Nb<sub>12</sub>O<sub>29</sub> crystals, the generation of new growth at the twin plane re-entrant edge results in the twin plane increasing in only one dimension as indicated in the sectional view through A-A, and the re-entrant edge is not increased. This is because the Nb<sub>12</sub>O<sub>29</sub> crystals are bounded by parallel {100} faces.

However, for NbO<sub>2</sub> crystals, the situation is somewhat different. New growth initiated at the re-entrant edge sites causes the twin plane to extend in two dimensions. Consequently, the length of the re-entrant edge is increased during growth as depicted in the sectional view through B-B.

In this case the NbO<sub>2</sub> crystal is bounded by two non-parallel {110} planes.

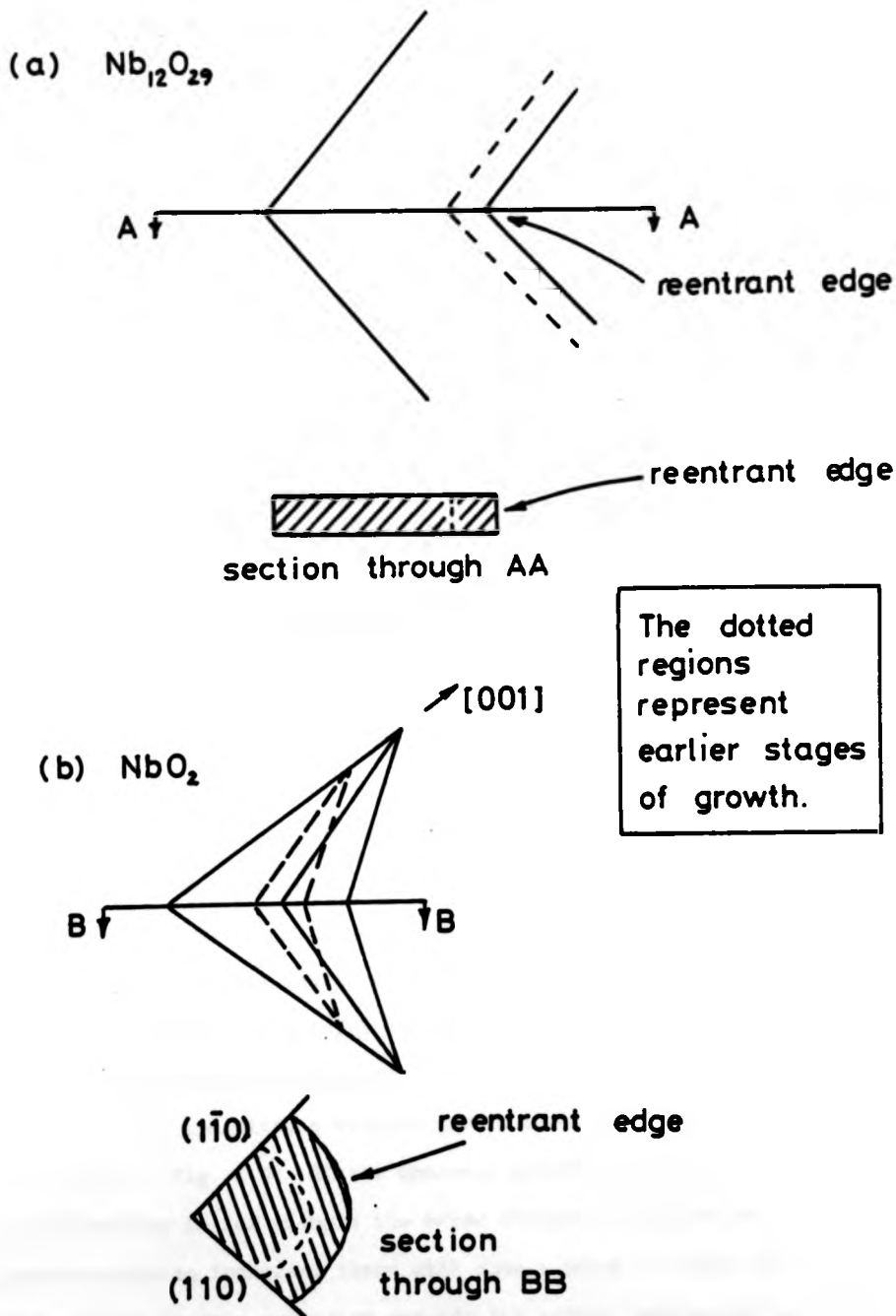


Fig. 4.24. A comparison of the TPRE in  $NbO_2$  and  $Nb_{12}O_{29}$ .

transport with NbO as the starting material were nucleated during the early stages of the reaction when the concentration of the transport reagent was relatively high. Thus these crystals grew when the effective supersaturation was relatively high. Because of the difference in the effective supersaturation during the growth of the two types of NbO<sub>2</sub> crystal it is not too surprising that the external form of the two types of crystal is different.

At the higher supersaturations, the crystals have a significantly lower tendency to form facets. For example, generally the twinned regions continue to grow in the [001] direction without forming {101} or {111} facets, although in some cases near the end of the reaction, when the transport reagent has been partially exhausted, the effective supersaturation is reduced and facets are occasionally observed. For example in Fig. 4.21 (a) the initial stages of development of a {111} facet can be seen, limiting the growth in the [001] direction. Thus there has apparently been a transition between two growth mechanisms in this case. The early part of the growth presumably occurred rapidly by a type of continuous growth process, but as the supersaturation decreased during the reaction a point was reached at which facets began to develop. At this stage the growth mechanism must have reverted to a process consistent with the formation of a low index surface. This could either be a screw dislocation mechanism or an island nucleation mechanism.

Such transitions between growth mechanisms can be understood by reference to Fig. 4.5. If the dominant growth mechanism at low supersaturations is for example the screw dislocation mechanism, then as the supersaturation is increased there will come a point at which the growth rate predicted by this mechanism exceeds the growth rate predicted by, for example, the continuous growth mechanism. Clearly this cannot occur and

so at such high supersaturations there must be a change from growth by the screw dislocation mechanism to continuous growth.

#### 4.3.3 $\text{H-Nb}_2\text{O}_5$

White needle shaped crystals of  $\text{H-Nb}_2\text{O}_5$  can be grown by chemical transport when the temperature of the growth zone is  $950^\circ\text{C}$  or above. Increasing the quantity of  $\text{TeCl}_4$  transport reagent results in a higher transport rate and at higher transport rates an increased frequency of nucleation leads to the growth of a polycrystalline crust. At low transport rates the number of crystals which nucleate is much lower and needle shaped crystals up to about 10 mm long have been obtained.

The structure of  $\text{H-Nb}_2\text{O}_5$  has been determined by Gatehouse and Wadsley (24). The unit cell is monoclinic with

a	=	21.34 Å
b	=	3.816 Å
c	=	19.47 Å
$\beta$	=	$120.3^\circ$

As in the case of  $\text{Nb}_{12}\text{O}_{29}$ , the crystal structure can be described in terms of columns of  $\text{NbO}_6$  octahedra. In  $\text{H-Nb}_2\text{O}_5$  columns of  $(5 \times 3 \times \infty)$  and  $(4 \times 3 \times \infty)$  are arranged as indicated in Fig. 4.25. Because of this arrangement of blocks there is an array of tetrahedral sites which are occupied by Nb atoms.

The growth axis of the needle shaped crystals was found to be parallel to the b-axis. This result is in agreement with the findings of Schafer et al. (25) for similar crystals which were obtained using chlorine gas as the transport reagent.

Fig. 4.25

The H-Nb<sub>2</sub>O<sub>5</sub> structure

In this schematic diagram of the H-Nb<sub>2</sub>O<sub>5</sub> structure, the standard conventions have been used (see Fig. 4.6). Unlike the Nb<sub>12</sub>O<sub>29</sub> structure, the Nb atoms are not all accommodated as NbO<sub>6</sub> octahedra. The black dots in the diagram represent Nb atoms which occupy tetrahedral sites.

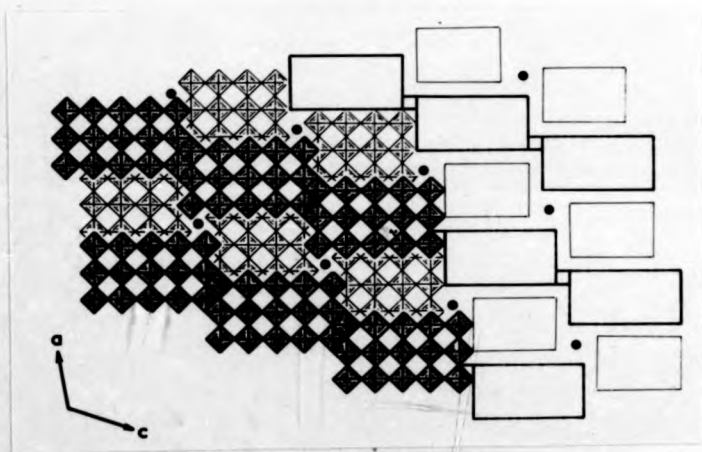


**Figure 4.25** Schematic diagram of the H-Nb<sub>2</sub>O<sub>5</sub> structure [010] projection



Since the crystal structure of  $\text{H-Nb}_2\text{O}_5$  is similar to the  $\text{Nb}_{12}\text{O}_{29}$  structure it is not surprising to find that in each case the principal growth direction is parallel to the columns of  $\text{NbO}_6$  octahedra (i.e. the [010] direction). In both crystals the growing interface has an array of steps with kink sites, which provide favourable sites for deposited atoms.

Unlike  $\text{Nb}_{12}\text{O}_{29}$ , however,  $\text{H-Nb}_2\text{O}_5$  does not grow in the form of platelets but only as needles. The growth of  $\text{Nb}_{12}\text{O}_{29}$  in platelet form was found to be a direct consequence of twinning and the re-entrant edge growth mechanism. No comparably twin related crystals have been observed in the case of  $\text{H-Nb}_2\text{O}_5$  and so this mechanism does not operate.

In many cases it has been demonstrated experimentally that the growth rate of whiskers exceeds the rate predicted by considering only the atoms arriving on the growing interface. To resolve this problem it has been proposed (26) that some of the atoms arriving along the length of the whisker can diffuse to the end and so contribute to the growth. Similarly atoms arriving along the length may also diffuse to the point at which the crystal is attached to the substrate and if suitable re-entrant sites exist, new growth layers may be initiated resulting in a thickening of the needles. Although this mechanism seems to provide a reasonable description of the growth of  $\text{H-Nb}_2\text{O}_5$  whiskers, experimental confirmation is difficult because the relationship between growth rate and supersaturation cannot easily be established.

It is interesting to note at this point, that the average transport rate observed during the growth of  $\text{Nb}_2\text{O}_5$  crystals was significantly higher than the transport rates observed under similar conditions for  $\text{Nb}_{12}\text{O}_{29}$  (see Table 2.3). Since  $\text{H-Nb}_2\text{O}_5$  and  $\text{Nb}_{12}\text{O}_{29}$  grow by a similar mechanism

and have very similar melting points and properties, this might appear to be surprising. However, because of the non-ideal nature of the chemical transport reaction leading to the growth of  $\text{Nb}_{12}\text{O}_{29}$  crystals the transport rate will be gradually reduced as the reaction progresses. In the growth of  $\text{H-Nb}_2\text{O}_5$ , however, the transport reagent is continually regenerated and after an initial transient period, the growth conditions remain constant.

#### 4.3.4 $\text{P-Nb}_2\text{O}_5$

Laves (27) investigated the structure of  $\text{P-Nb}_2\text{O}_5$  and found it to have a tetragonal unit cell related to  $\text{V}_2\text{O}_5$ . The unit cell parameters were determined by Mertin (28) from Guinier X-ray photographs to be

$$\begin{array}{rcl} a & = & 3.90 \text{ \AA} \\ c & = & 25.5 \text{ \AA} \end{array}$$

Petter and Laves (29) observed a high incidence of internal twins in rectangular platelike crystals of  $\text{P-Nb}_2\text{O}_5$  grown by chemical transport.

In this work  $\text{P-Nb}_2\text{O}_5$  grew in the form of a crust of small yellow crystals as shown in Fig. 4.26 (a). An examination of these crystals in the S.E.M. showed that well developed facets were formed during growth, the crystals commonly taking the form of tetragonal prisms or truncated octahedra (Fig. 4.26 (b)).

These crystals were too small to be oriented using the standard Laue diffraction technique, although by measuring interplanar angles using the goniometer stage in the S.E.M. and comparing these angles with a computed set of interplanar angles, some of the faces of the crystals could be tentatively indexed. The results obtained in this way were consistent with the assumption that the crystals were limited by faces of the  $\{001\}$ ,  $\{100\}$  and  $\{011\}$  types.

Of the growth mechanisms discussed in the early part of this chapter, only the island nucleation model and the screw dislocation model are

Fig. 4.26

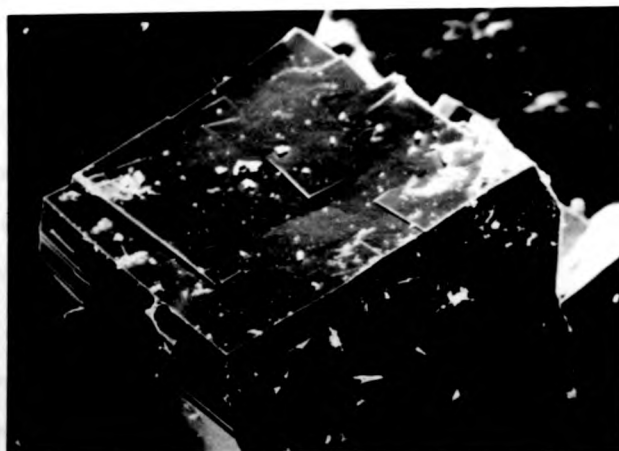
P-Nb<sub>2</sub>O<sub>5</sub> crystals

The S.E.M. micrograph (a) shows part of a crust of yellow P-Nb<sub>2</sub>O<sub>5</sub> crystals. The individual crystallites (b) had dimensions of the order of 0.1  $\mu$ m. The well developed facets often exhibited step-like features indicating a dislocation assisted growth mechanism.



1 mm

Figure 4.26 (a) Agglomeration of P-Nb<sub>2</sub>O<sub>5</sub> crystals



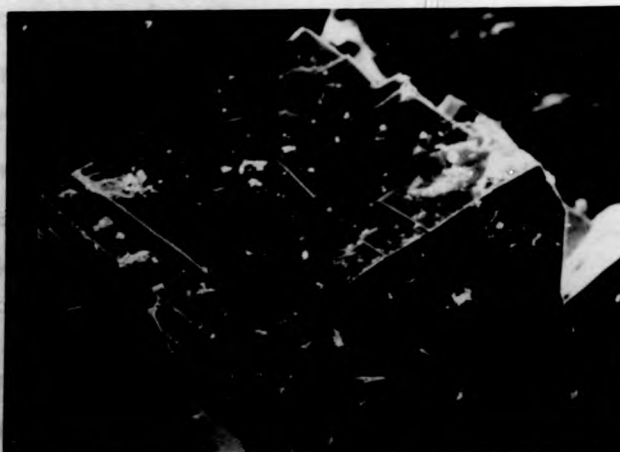
100 μm

Figure 4.26 (b) Surface growth features on a P-Nb<sub>2</sub>O<sub>5</sub> crystal



1 mm

**Figure 4.26 (a) Agglomeration of  $P-Nb_2O_5$  crystals**



100  $\mu$ m

**Figure 4.26 (b) Surface growth features on a  $P-Nb_2O_5$  crystal**

consistent with faceted growth. The spiral nature of the ledge shown in Fig. 4.26 (b) suggests that the screw dislocation mechanism dominates the growth behaviour.

#### 4.3.5 B-Nb<sub>2</sub>O<sub>5</sub>

The crystal structure of B-Nb<sub>2</sub>O<sub>5</sub> was also investigated by Laves et al. (30) and they determined the unit cell to be monoclinic with

$$\begin{aligned} a &= 12.73 \text{ \AA} \\ b &= 5.56 \text{ \AA} \\ c &= 4.88 \text{ \AA} \\ \gamma &= 105^{\circ} 05' \end{aligned}$$

The crystals of B-Nb<sub>2</sub>O<sub>5</sub> which were produced in the course of this work grew in the form of yellow/white semi-transparent, monoclinic plates. In fact most of the crystals studied were comprised of two or more twin related components as shown in Fig. 4.27 (a).

In both NbO<sub>2</sub> and Nb<sub>12</sub>O<sub>29</sub> twinning was normally observed to have occurred during the early stages of growth. However, observations of twinning in the crystals of B-Nb<sub>2</sub>O<sub>5</sub> apparently occur at any stage of the growth process. Once a twin has nucleated there is strong evidence that the TPFE mechanism accelerates the thickening of the plates. Fig. 4.27 (a) and (b) show the generation of growth steps at the re-entrant edge sites and their subsequent propagation.

#### 4.3.6 Niobium monoxide (NbO)

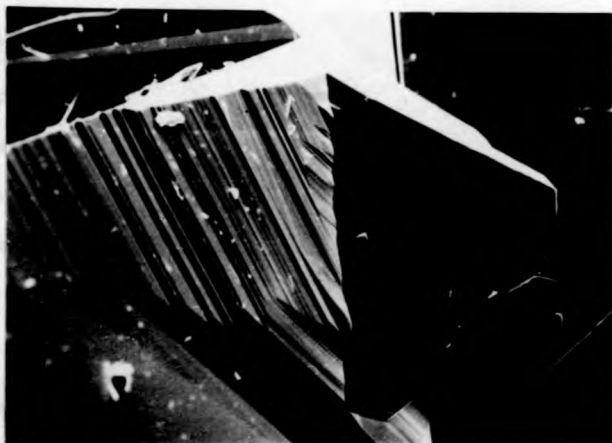
Andersson and Magneli (31) determined the crystal structure of NbO by X-ray diffraction using single crystals obtained by arc melting. The unit cell is cubic with a defective NaCl structure; the positions 0,0,0 and  $\frac{1}{2}, \frac{1}{2}, \frac{1}{2}$  being vacant.

Fig. 4.27

B-Nb<sub>2</sub>O<sub>5</sub> crystals

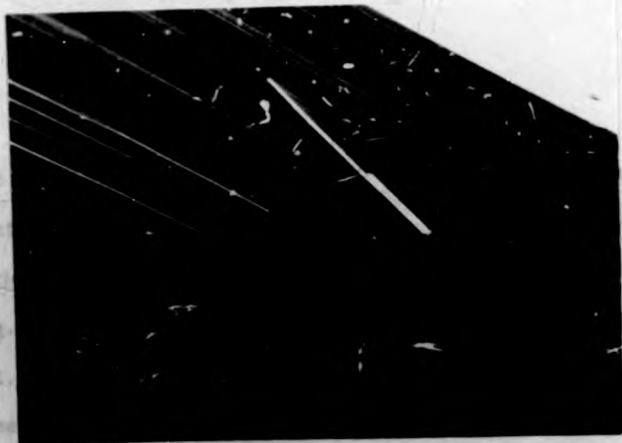
Scanning electron micrograph (a) shows twin-related plate crystals characteristic of the B-Nb<sub>2</sub>O<sub>5</sub> growth experiments. The principal growth features appear to be initiated at the twin plane re-entrant edge.

The new growth layers which develop at these sites rapidly spread on the surfaces of the twin related branches as shown in micrograph (b).



100  $\mu\text{m}$

**Figure 4.27 (a) Twinning in  $\text{B-Nb}_2\text{O}_5$  crystal**



50  $\mu\text{m}$

**Figure 4.27 (b) Steps propagating on the surface of  $\text{B-Nb}_2\text{O}_5$  crystal**



Growth of NbO crystals by chemical transport involves the transfer of material from a cooler source zone to a hotter growth zone. A high nucleation rate on the substrate walls resulted in the formation of a crust of very small NbO crystals as shown in Fig. 4.28. The mechanism of growth of these crystals has not yet been fully investigated.

#### 4.3.7 Niobium ditelluride (NbTe<sub>2</sub>)

If a high concentration of TeCl<sub>4</sub> is used during the growth of NbO<sub>2</sub> crystals from powdered NbO, pseudohexagonal plates of NbTe<sub>2</sub> may also result.

Van Landuyt et al. (32) have prepared similar crystals by a chemical transport technique using iodine as the transport reagent. According to Brown (33), the structure of NbTe<sub>2</sub> is layered similar to the cadmium iodide structure. However there is slight deviation from the hexagonal symmetry and the unit cell is monoclinic with

$$\begin{array}{rcl} a & = & 19.39 \text{ \AA} \\ b & = & 3.642 \text{ \AA} \\ c & = & 9.375 \text{ \AA} \\ \beta & = & 123^{\circ} 35' \end{array}$$

The monoclinic unit cell can be derived from the undeformed hexagonal structure by a perturbation in any one of three directions. This gives rise to the domain structure described by Van Landuyt et al. (32).

Fig. 4.29 is a micrograph of the NbTe<sub>2</sub> plates taken using polarised light. The domain structure is clearly visible. The crystals have clearly been growing by a mechanism involving the generation and propagation of ledges.

Fig. 4.28

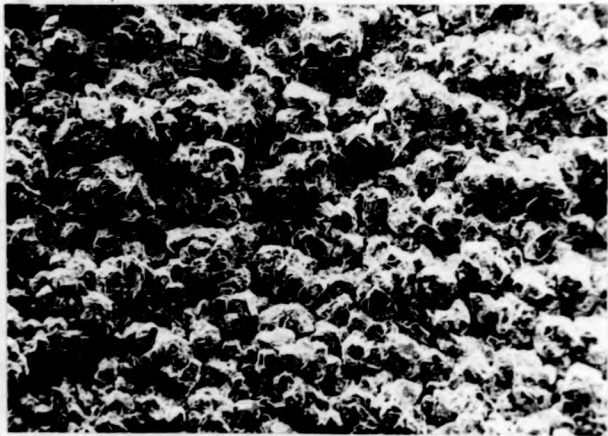
NbO crystals

The crust of NbO crystals was removed from the hot end (1050 - 1100°C) of a chemical transport reaction tube. The individual crystallites are of the order of 0.1 mm in diameter and are very irregular with poorly developed facets.

Fig. 4.29

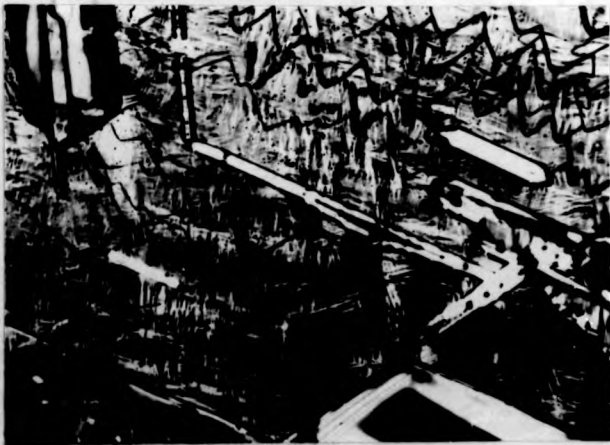
Niobium ditelluride crystals

The pseudohexagonal plates of NbTe<sub>2</sub> were photographed using a Zeiss Ultraphot microscope in reflected polarised light. The "saw-tooth" pattern on the crystal surface is due to growth steps. The use of polarised light reveals the fine domain structure and indicates that a structural transformation has occurred during cooling from the growth temperature.



1 mm

Figure 4.28 S.E.M. micrograph of a "crust" of NbO crystals



0.2 mm

Figure 4.29 Plates of Nb Te<sub>2</sub> showing growth steps and domain structure (polarised light)

4. 4 Summary

The crystals which have been grown by chemical transport display a wide range of growth morphologies which can be related both to their crystal structures and to the mechanism of growth and the morphological observations of the chemically transported crystals provides a great deal of information about the growth process. However this information can be supplemented in some cases by the use of transmission electron microscopy. Such studies of the internal structure of "as grown" crystals can provide information about the degree of perfection of the crystals and the frequency and nature of growth accidents as a function of growth rate.

The use of high resolution electron microscopy for the study of the "block structure" niobium oxides can also be used to study subtle structural variations and non-stoichiometry.

REFERENCES

1. Computer program developed by Dr. P.S. Bell.
2. R.A. Laudise, "The Growth of Single Crystals", Prentice-Hall, Inc., New Jersey, 1970.
3. J.W. Christian, "The Theory of Transformations in Metals and Alloys", Pergamon Press, Oxford, 1965.
4. M.M. Faktor and I. Garrett, "Growth of Crystals from the Vapour", Chapman and Hall, London, (1974).
5. P. Hartman (ed.), "Crystal Growth; An Introduction", North Holland Pub. Co., Amsterdam, (1973).
6. H.A. Wilson, Phil. Mag., 50, 238, (1900).
7. J. Frenkel, Physik Z. Sovjetunion, 1, 498, (1932).
8. W. Kossel, Nachr. Ges. Wiss. Gottingen, p. 135, (1927).
9. M. Volmer, "Kinetik der Phasenbildung", Steinkopf, Dresden, (1939).  
R. Becker, Proc. Phys. Soc., 52, 71, (1940).
10. R.N. Haward, Trans. Faraday Soc., 35, 1401, (1939).
11. F.C. Frank, Disc. Faraday Soc., 5, 48, 67, (1949)
12. A.J. Forty, Phil. Mag., 43, 72, (1952).
13. A.R. Verma, "Crystal Growth and Dislocations", Butterworth's, London, (1953).
14. R.S. Wagner, Acta Met., 8, 57, (1960).
15. J.W. Faust and H.F. John, J. Phys. Chem. Solids, 25, 1407, (1964).
16. J.W. Faust and H.F. John, Trans. Met. Soc. AIME, 233, 230, (1965).
17. R. Norin, Acta Chem. Scand., 17, 1391, (1963).
18. R. Norin, Acta Chem. Scand., 20, 871, (1966).
19. T. Sakata, K. Sakata, G. Hofer, T. Horiuchi, J. Cryst. Growth, 12, 88, (1972).

20. H.J. Scheel and D. Elwell, *J. Cryst. Growth*, 20, 259, (1973).
21. A. Magneli, G. Anderson and G. Sundkvist, *Acta Chem. Scand.*, 9, 1402, (1955).
22. T. Sakata, K. Sakata and I. Nishida, *Phys. Stat. Sol.*, 20, K155, (1967).
23. H. Kodama and M. Goto, *J. Cryst. Growth*, 29, 77, (1975). *J. Cryst. Growth*, 29, 222, (1975).
24. B.M. Gatehouse and A.D. Wadsley, *Acta Cryst.*, 17, 1545, (1964).
25. H. Schafer, F. Schulte and R. Gruehn, *Angew. Chem. Internat. edit.*, 3, 511, (1964).
26. R.V. Coleman and G.W. Sears, *Acta Met.*, 5, 31, (1957).
27. F. Laves, R. Moser and W. Petter, *Naturwissenschaften*, 51, 356, (1964).
28. W. Mertin - results presented in reference (25).
29. W. Petter and F. Laves, *Naturwissenschaften*, 52, 617, (1965).
30. F. Laves, W. Petter and H. Wulf, *Naturwissenschaften*, 51, 633, (1964).
31. S. Andersson and A. Magneli, *Acta. Chem. Scand.*, 11, 1065, (1957).
32. J. Van Landuyt, G. Remaut and S. Amelinckx, *phys. stat. sol.*, 41, 271, (1970).
33. B.E. Brown, *Acta Cryst.*, 20, 264, (1966).
34. R.S. Wagner and W.C. Ellis, *Appl. Phys. Lett. (U.S.A.)*, 4, 89-90, (1964).
35. J.M. Blakely. "An Introduction to the Properties of Crystal Surfaces", Pergamon, 1973.

## CHAPTER FIVE

### EXAMINATION OF THE CRYSTALS BY TRANSMISSION ELECTRON MICROSCOPY

The oxides of niobium have been studied extensively by X-ray diffraction, electron diffraction and high resolution electron microscopy, and the basic crystal structures of most of the oxides is well documented.

The development of transmission electron microscopes capable of resolving features with dimensions of the order of a few Angstroms has enabled the detailed structure of imperfections in some suitable specimens to be observed. These high resolution techniques have been used to advantage in the study of the higher niobium oxides ( $\text{Nb}_{12}\text{O}_{29}$  -  $\text{Nb}_2\text{O}_5$ ).

After a brief description of the mechanisms of image formation in the electron microscope and the experimental techniques used, this chapter is devoted to observations of the microstructures of the "as grown" crystals.  $\text{NbO}_2$  crystals were studied by conventional transmission electron microscope techniques and the  $\text{Nb}_{12}\text{O}_{29}$  and  $\text{H-Nb}_2\text{O}_5$  crystals were studied principally by high resolution electron microscopy (HREM). The other oxide crystals have not so far been studied in detail by these methods.

#### 5.1 Electron Diffraction and Image Formation in the Transmission Electron Microscope

A detailed treatment of contrast mechanisms in electron microscopy is beyond the scope of this thesis. A comprehensive analysis of electron diffraction and image theory can be found in standard text books (for example Hirsch et al(1)). However, a brief description of the principles of image formation is presented here.

##### 5.1.1 Electron diffraction

High energy electrons can interact with thin crystalline foils in a number of ways. The scattering processes which occur can be

classified as either inelastic or elastic interactions.

In inelastic scattering, some of the energy of the incident electrons is dissipated by interactions with atoms in the specimen. This exchange of energy may result in for example the generation of X-rays or phonons. Elastically scattered electrons result in the formation of electron diffraction patterns. By analogy with X-ray diffraction, elastic scattering of electrons can be described by Bragg's Law:

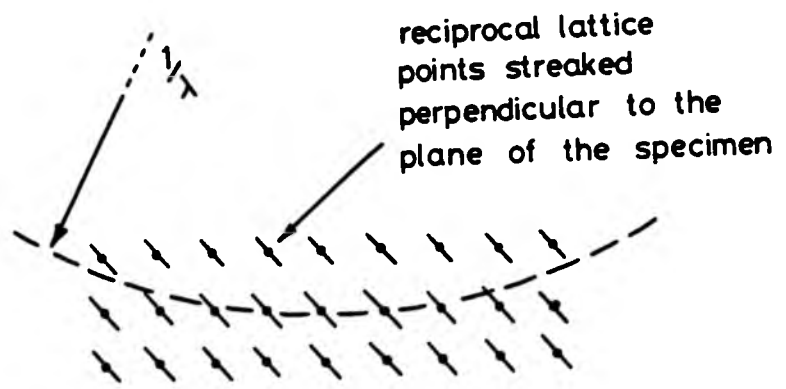
$$n\lambda = 2d \sin \theta \quad \dots\dots\dots (1)$$

where d is the interplanar spacing  
n is the order of reflection  
 $\lambda$  is the electron wavelength  
 $\theta$  is the Bragg angle

Thus when a beam of electrons interacts with a crystalline specimen, diffracted beams will be produced whenever the Bragg condition is satisfied. The concept of the reciprocal lattice and the Ewald sphere construction are convenient ways of explaining the observed electron diffraction patterns and are described in detail in standard textbooks on electron microscopy (see Hirsch et al (1)).

The Ewald sphere construction is illustrated diagrammatically in Figure 5.1. Each interplanar spacing,  $d(hkl)$  has a corresponding reciprocal lattice vector  $g(hkl)$ . The Ewald sphere is a sphere in reciprocal space with radius  $\frac{1}{\lambda}$  (where  $\lambda$  is the electron wavelength). One point on the circumference of this sphere is fixed at the origin of the reciprocal lattice and this represents the transmitted beam. Where the sphere intersects other reciprocal lattice points, the Bragg condition is satisfied and the corresponding diffraction spots will be observed. In fact, since the specimens are very thin for transmission electron microscopy, the reciprocal lattice spots are elongated in a direction perpendicular to the specimen plane. This results in the appearance of





Predicted diffraction pattern - 1st Laue Zone  
(see ref.1.)

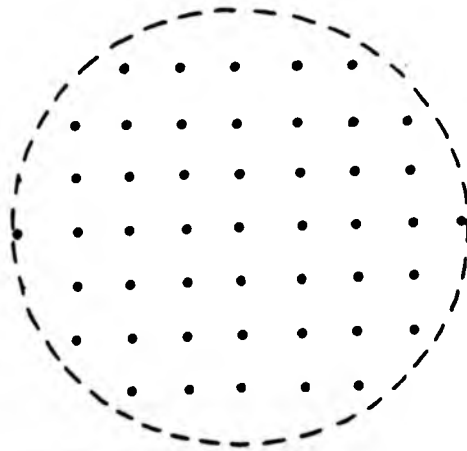


Fig. 5.1. The Ewald sphere construction.

diffraction spots for which the Bragg condition is not exactly satisfied. Small variations in orientation within the selected area will also result in an increased number of diffraction spots.

The radius of the Ewald sphere is very large compared to the distance between the reciprocal lattice points and consequently the observed diffraction pattern will approximate to a planar section through the reciprocal lattice as indicated in Figure 5.1.

By tilting the specimen, different reciprocal lattice sections can be observed and in this way a three-dimensional model of the reciprocal lattice can be constructed.

#### 5.1.2 Image formation by diffraction contrast

High contrast images are generally obtained in the electron microscope by the following procedures:

- (i) The specimen is tilted in such a way that only one diffracted beam is strongly excited. This is normally referred to as a two-beam condition since most of the electrons which pass through the specimen are concentrated into either the undiffracted beam or the strongly excited diffracted beam.
- (ii) If the undiffracted beam is selected by using an objective aperture a "bright field" image is formed on the screen. In this case features which give rise to strong diffraction will appear dark.
- (iii) A "dark field" image can be produced by positioning the objective aperture in such a way that only the strongly excited diffracted beam contributes to the image. New features which are strongly diffracting will appear bright on the image. In this case since the diffracted beam does not pass through the centre of the imaging lenses it will be affected by spherical aberration. This problem can be overcome by changing the angle

of illumination of the specimen in such a way that the diffracted beam can pass down the centre of the column. Modern microscopes are provided with a set of beam tilting controls for this purpose.

The contrast in images formed by these processes can be successfully explained by the two-beam dynamical theory developed by Howie and Whelan(2). This theory predicts the amplitudes of the undiffracted and diffracted beams after they have left the specimen by considering a continuous series of scattering events between the incident wave with wave vector  $k$  and the diffracted wave, with wave vector  $(k + g + s)$ , where  $g$  is the reciprocal lattice vector and  $s$  is a small vector corresponding to the deviation from the exact Bragg condition.

The amplitudes  $\phi_0$  and  $\phi_g$  of the undiffracted and diffracted beams at a depth  $z$  in the crystal are given by:

$$\frac{d\phi_0}{dz} = \frac{\pi i}{\xi_0} \phi_0 + \frac{\pi i}{\xi_g} \phi_g \exp(2\pi i s z) \dots\dots\dots(2)$$

$$\frac{d\phi_g}{dz} = \frac{\pi i}{\xi_0} \phi_0 + \frac{\pi i}{\xi_g} \phi_g \exp(-2\pi i s z) \dots\dots\dots(3)$$

$\xi_0$  and  $\xi_g$  are known as the extinction distances for scattering in the forward and diffracted directions respectively, and are given by:

$$\xi_0 = \frac{\pi V_c \cos \theta}{\lambda F_0} \dots\dots\dots(4)$$

$$\xi_g = \frac{\pi V_c \cos \theta}{F_g} \dots\dots\dots(5)$$

where  $\theta$  is the Bragg angle  
 $V_c$  is the unit cell volume  
 $F_0$  is the structure factor for forward scattering and depends on the electron scattering power of the atoms in the unit cell at zero angle  $F_0$

and  $F_g$  is the structure factor for scattering through the Bragg angle, and depends on the position of the atoms in the unit cell and their electron scattering power,  $F_0$ .

The detailed solution of equations (2) and (3) is beyond the scope of this work, however it is found that both  $\phi_0$  and  $\phi_g$  have two independent solutions, referred to as Bloch waves, and contrast effects can be explained in terms of beating between these waves. Differences in scattering of these waves leads to the anomalous absorption effect and this is normally taken into account by modifying the extinction distances,

i.e.  $\frac{1}{\xi_0}$  and  $\frac{1}{\xi_g}$  are replaced by:

$$\frac{1}{\xi_0} + \frac{i}{\xi_0} \quad \text{and} \quad \frac{1}{\xi_g} - \frac{i}{\xi_g}$$

$$\text{where } \frac{\xi_0}{\xi_g} = \frac{\xi_g}{\xi_0}$$

Crystalline defects in the electron microscope sample give rise to changes of phase of the Bloch waves and the corresponding changes in the image contrast are characteristic of the type of defect.

A simple treatment of the contrast effects at inclined anti-phase boundaries (APB's) will be given in a subsequent section.

### 5.1.3 The formation of lattice images

Diffraction contrast images are formed using either the undeviated transmitted electron beam or one of the diffracted beams. If two or more coherent beams are selected a periodic image can be generated. The mechanism by which such images arise can be simply demonstrated using the kinematical approximation. (The kinematic theory of electron diffraction does not take into account the multiple scattering of electrons.

For very thin specimens the agreement between the predictions of this theory and experimental observations is qualitatively very good.) Consider the simplest case of an image formed by using the undeviated beam and one diffracted beam. Following the argument of Hirsch et al(1): the total wave function can be written:

$$\psi = e^{2\pi i \underline{k} \cdot \underline{r}} + \phi_g e^{2\pi i \underline{k}^1 \cdot \underline{r}} \dots\dots\dots (6)$$

(incident beam of unit amplitude)      (diffracted beam)      where  $\underline{k}^1 = \underline{k} + \underline{g}$

$$\therefore \psi = e^{2\pi i \underline{k} \cdot \underline{r}} \left( 1 + \phi_g e^{2\pi i \underline{g} \cdot \underline{r}} \right) \dots\dots\dots (7)$$

Let  $\phi_g = \text{Re}^{i\delta} \dots\dots\dots (8)$

Then  $\psi = e^{2\pi i \underline{k} \cdot \underline{r}} \left( 1 + \text{Re}^{i(2\pi \underline{g} \cdot \underline{r} + \delta)} \right) \dots\dots\dots (9)$

The total intensity I is given by:

$$I = \psi \psi^* = 1 + R^2 + 2R \cos(2\pi \underline{g} \cdot \underline{r} + \delta) \dots\dots\dots (10)$$

Now the kinematical theory gives:

$$\phi_g = \frac{i\pi \sin \frac{\pi t s}{\xi_g}}{\xi_g} e^{-\pi i t s} \dots\dots\dots (11)$$

where  $\xi_g$  is the extinction distance  
 t is the specimen thickness  
 s is the deviation from the Bragg condition

Comparing Equations (8) and (11)

$$R = \frac{\pi \sin \frac{\pi t s}{\xi_g}}{\xi_g} \dots\dots\dots (12)$$

and  $\delta = \frac{\pi}{2} - \pi t s \dots\dots\dots (13)$

Rewriting Equation (10) and substituting for  $\delta$

$$I = 1 + R^2 + 2R \sin(2\pi \underline{g} \cdot \underline{r} - \pi t s) \dots\dots\dots (14)$$

Now  $g$  is nearly normal to the incident beam and a co-ordinate  $x$  can be chosen parallel to this direction in a plane normal to the beam.

Equation (14) can then be rewritten:

$$I = 1 + R^2 + 2R \sin\left(2\pi \frac{x}{d} - \pi t s\right) \dots\dots\dots (15)$$

The third term in this equation represents a sinusoidal variation in the image intensity with a periodicity equal to  $d$ , the lattice spacing corresponding to the reciprocal lattice vector  $g$ .

The image contrast will also be a function of thickness\* and orientation of the specimen (Equation (14) shows the dependence of  $R$  on  $S$  and  $t$ ). Thus two beam lattice images consist of parallel sine fringes.

A more rigorous dynamical treatment of two beam lattice image contrast can be found in the work of Hashimoto et al (3).

By using a larger objective aperture several diffracted beams can be allowed to contribute to the image and where non-colinear diffraction spots are used two dimensional lattice images can be generated. In fact the generation of lattice images is in many ways analagous to the process of Fourier synthesis used in structure determination by X-rays. For a structural determination the intensity of a large number of diffracted X-ray beams is measured, and these are recombined, taking into account the relative phases, to reconstruct the structure. In the electron microscope, a limited number of diffracted beams can be automatically recombined with approximately correct phase relationships to form a lattice image. In principle, the greater the number of beams which contribute to the image, the better the correspondence between the image and the parent structure. In practice however, spherical aberration leads to incorrect phase differences between diffracted beams and this becomes a serious limitation for all but the low order reflections. The amount of detailed structural information which can be gained by this technique is limited by the resolving power of the electron microscope.

\* See note overleaf

Note:

Lattice fringe contrast is a consequence of the recombination of elastically scattered beams of electrons. Thus for best fringe visibility it is advantageous to use very thin specimens where the intensity of inelastically scattered electrons is small.

#### 5.1.4 Factors influencing the contrast in lattice images

To fully understand the lattice images produced in the transmission electron microscope it is important to consider the influence of both instrumental effects and specimen dependent effects. The dependence of lattice images on specimen thickness and orientation has already been introduced (see Equations (14) and (15)). The dynamical treatment of the two-beam lattice image contrast enabled Hashimoto et al (3) to predict this dependence in detail. In a wedge shaped crystal the position of the fringes shifts laterally as the thickness changes, the shift being one fringe spacing for each change in thickness of one extinction distance. Deviations from the exact Bragg condition lead to slight changes in fringe spacing. This dependence of fringe contrast on thickness and orientation means that a satisfactory correspondence between fringe detail and the structure can only be achieved under well defined conditions. Generally, the specimens used for lattice image work are very thin (about 100 Å) and have to be carefully oriented using the goniometer stage in the electron microscope. However, even under closely controlled conditions, it has been shown, using the two-beam approach, that the images of defects such as dislocations may not necessarily have a one to one correspondence with the structure at the defect (4). Thus it would appear that the correspondence between lattice images and the structure cannot easily be interpreted. However, over the past ten years, a number of experimental observations has suggested that there are some circumstances when many-beam lattice images correlate well with the crystal structure. Many of these observations relate to complex oxide structures including the niobium oxides and will be referred to in a later section.

There are several important instrumental effects which



influence the resolution and contrast of lattice images, and it is useful to consider these in some detail.

(a) Specimen drift

If during the time of exposure there is relative motion of the specimen with respect to the microscope column the contrast of the lattice image will be reduced. If, for example, the specimen moves by a distance equivalent to half a fringe spacing during the exposure, then the lattice image will not be recorded at all.

(b) Lens current and H.T. fluctuations

Variation of the H.T. during the recording of an image causes a variation in the wavelength of the electrons. As the wavelength varies, so does the focal position of the lenses (chromatic aberration) and the image which is recorded is equivalent to a superposition of images taken under different focussing conditions. Variations in lens currents during exposure result in a similar degradation of the recorded images. It should be pointed out that in modern instruments such variations are small and the aberrations which result are not generally very important.

(c) Contamination of the specimen

The effect of the electron beam on the hydrocarbons in the microscope vacuum results in the gradual build-up of an amorphous deposit on the specimen under the beam. At high magnification, a high beam current density is required for a bright image and during lattice resolution work the same area of specimen is often under observation for a considerable time. Consequently the degradation of images by the build-up of contamination can be a serious problem, and steps are generally taken to reduce the effect by introducing liquid nitrogen cooled baffles near the specimen

onto which the contaminants can be condensed.

(d) Spherical aberration

The effect of spherical aberration of the objective lens has already been discussed briefly. However, as this effect has an important influence on the image contrast it is worthy of further consideration.

A diffracted beam which traverses the lens at an angle  $2\theta$  to the optic axis suffers a phase retardation,  $\Omega$ , given by:

$$\Omega = \frac{8\pi \cdot C_s}{\lambda} \theta^4 \dots\dots\dots (16)$$

where  $C_s$  is the spherical aberration coefficient

$\lambda$  is the electron wavelength

$\theta$  is the Bragg angle.

Since  $\theta$  is small for electron diffraction

$$\lambda = 2d\theta$$

and therefore

$$\Omega = \frac{\pi C_s \lambda^3}{2d^4} \dots\dots\dots (17)$$

Now if the diffracted beam corresponding to the spacing,  $d$ , is subjected to a phase retardation of  $\pi$  or more with respect to the undeviated beam, the contrast will be significantly modified.

For example with  $C_s = 3 \text{ mm}$

$$\lambda = 0.0037 \text{ nm (for 100 kV electrons)}$$

$\Omega$  will have a value of  $\pi$  or greater for diffracted beams which correspond to  $d_{hkl}$  of 0.5 nm or less and the contribution of such diffracted beams would be detrimental to the resulting image.

For this reason an objective lens aperture is selected so as to allow only those diffracted beams which have a suitably low phase shift, to contribute to the image.

onto which the contaminants can be condensed.

(d) Spherical aberration

The effect of spherical aberration of the objective lens has already been discussed briefly. However, as this effect has an important influence on the image contrast it is worthy of further consideration.

A diffracted beam which traverses the lens at an angle  $2\theta$  to the optic axis suffers a phase retardation,  $\Omega$ , given by:

$$\Omega = \frac{8\pi \cdot C_s \theta^4}{\lambda} \dots\dots\dots (16)$$

where  $C_s$  is the spherical aberration coefficient

$\lambda$  is the electron wavelength

$\theta$  is the Bragg angle.

Since  $\theta$  is small for electron diffraction

$$\lambda = 2d\theta$$

and therefore

$$\Omega = \frac{\pi C_s \lambda^3}{2d^4} \dots\dots\dots (17)$$

Now if the diffracted beam corresponding to the spacing,  $d$ , is subjected to a phase retardation of  $\pi$  or more with respect to the undeviated beam, the contrast will be significantly modified.

For example with  $C_s = 3 \text{ mm}$

$$\lambda = 0.0037 \text{ nm (for 100 kV electrons)}$$

$\Omega$  will have a value of  $\pi$  or greater for diffracted beams which correspond to  $d_{hkl}$  of 0.5 nm or less and the contribution of such diffracted beams would be detrimental to the resulting image.

For this reason an objective lens aperture is selected so as to allow only those diffracted beams which have a suitably low phase shift, to contribute to the image.

The phase changes which occur as the angle with the optic axis varies (equation (16)) means that there is some advantage in keeping the illumination convergence as low as possible. This can be achieved by selecting a small condenser aperture. However, the advantage gained by this is offset to some extent by the diminished brightness of the image and the longer exposure times which have to be used.

In practice, the smallest condenser aperture consistent with an exposure time of 5-10 seconds seems to give the best results.

Note:

Lattice images can be formed by the recombination of any of the diffracted beams with the undiffracted beam (bright field lattice imaging) or indeed by recombining diffracted beams only (dark field lattice imaging).

Bright field multi-beam lattice images are normally obtained by positioning the objective aperture in such a way that its centre coincides with the undiffracted beam. In this way pairs of symmetric reflections contribute to the lattice image. Thus the intensity and phase of each diffracted beam will be approximately matched by the corresponding symmetrical reflection. In this way the intensity contribution from each pair of reflections will be symmetrical. The contributions from unpaired reflections could result in a distortion of the lattice fringe profiles.

(e) Focussing condition

A change in focal length of the objective lens will cause a relative phase change between the undeviated and diffracted electron beams. (5) There is a significant amount of experimental evidence to suggest that the best lattice images are formed at a certain underfocus with respect to the Gaussian image plane. This underfocus is generally reported to be of the order of 50-100 nm.

(f) Objective lens astigmatism

This lens defect can result in serious degradation of detail, particularly in the case of two-dimensional lattice images. Fortunately in modern microscopes stigmators are provided and the effects can be almost entirely eliminated.

Sections (a), (b) and (c) above describe instrumental effects which cannot readily be taken into account when analysing the detailed contrast of lattice images. However, measures can be taken to reduce these effects by instrument design or operating procedures. For example, modern stage design in high resolution microscopes is such that specimen drift is typically much less than 0.1 nm per sec. Similarly, high performance, high brightness electron sources have resulted in shorter exposure times and with thin specimens lattice images can be recorded in a matter of a few seconds at magnification of 250,000 times.

The effects of spherical aberration (d) and focussing (e) can, in principle, be corrected for. Workers in Australia have in fact developed a computer programme to predict contrast in many beam lattice images (5-8) and corrections for these effects are incorporated. In the cases so far examined they have obtained excellent agreement between the predicted and observed images.

## 5.2 Experimental Techniques for Electron Microscopy

### 5.2.1 Specimen preparation

With the exception of NbO and the suboxide phases, the oxides of niobium are very brittle. The most commonly reported technique of specimen preparation for these materials is by fragmentation (see for example Iijima(9), Hutchison et al (10)). Crystals of the niobium oxide are crushed into small fragments and these can then be dispersed on a holey carbon support film for observation in the electron microscope. In this work, an alternative method of supporting the fragments was used. The adhesive from a short (3-4 inch) strip of "sellotape" was dissolved in about 25 ml of chloroform. Using fine tweezers a standard 100-mesh copper electron microscope grid was immersed in this solution for a few seconds until it had been thoroughly wetted and then removed. The chloroform evaporated after a short time, leaving the grid bars coated with a thin layer of adhesive. The grid was then pressed into the fragments of oxide and some of them adhered to the grid bars. After tapping carefully to remove the excess fragments, the specimen was ready for the microscope.

No noticeable problems of drift or charging were experienced during observations on specimens prepared in this way, lattice images of 4-5 Å resolution being recorded routinely with suitable materials.

### 5.2.2 The electron microscopes

The majority of the microscopy carried out during the course of this work was performed using a JEOL JEM 200 electron microscope operating at 200 kV. This instrument was equipped with a top entry double-tilt goniometer stage. A liquid nitrogen cooled anti-contamination device was fitted in the specimen chamber. Some of the high resolution lattice images presented in this chapter were obtained using a recently acquired JEM 100C microscope. In this case the goniometer stage was of

the side entry type with a eucentric tilting axis.

Reference to Equation (17) indicates that the use of a higher accelerating voltage (lower electron wavelength,  $\lambda$ ) should result in a reduction in the effects of spherical aberration. However, in this case the superior inherent resolution of the JEM 100C and the significantly better spherical aberration coefficient of the objective lens more than compensates for the effect of wavelength and the lattice images produced in the JEM 100C are appreciably better.

### 5.2.3 Obtaining lattice images

The procedure used for obtaining lattice images can be described as follows:

- (a) The instrument was prepared for high resolution work by filling up the cold traps and anti-contaminator with liquid nitrogen to minimise the degradation of the specimen.
- (b) The full alignment procedure of the optical system of the electron microscope was carefully carried out to ensure that where possible the diffracted beams used to form the images were symmetrically disposed about the axis of the microscope.
- (c) A suitable area of the specimen was selected. Ideally this was a very thin fragment of crystal with an orientation close to the required zone axis.
- (d) By observing the diffraction pattern the crystal fragment of interest was oriented such that a systematic row of diffraction spots or a two-dimensional array of diffraction spots appeared symmetrically on the fluorescent screen. The correct orientation of the fragment is critical for the formation of high quality lattice images.
- (e) At this stage an objective aperture was introduced to select a number of beams which were to contribute to the lattice image.

the side entry type with a eucentric tilting axis.

Reference to Equation (17) indicates that the use of a higher accelerating voltage (lower electron wavelength,  $\lambda$ ) should result in a reduction in the effects of spherical aberration. However, in this case the superior inherent resolution of the JEM 100C and the significantly better spherical aberration coefficient of the objective lens more than compensates for the effect of wavelength and the lattice images produced in the JEM 100C are appreciably better.

### 5.2.3 Obtaining lattice images

The procedure used for obtaining lattice images can be described as follows:

- (a) The instrument was prepared for high resolution work by filling up the cold traps and anti-contaminator with liquid nitrogen to minimise the degradation of the specimen.
- (b) The full alignment procedure of the optical system of the electron microscope was carefully carried out to ensure that where possible the diffracted beams used to form the images were symmetrically disposed about the axis of the microscope.
- (c) A suitable area of the specimen was selected. Ideally this was a very thin fragment of crystal with an orientation close to the required zone axis.
- (d) By observing the diffraction pattern the crystal fragment of interest was oriented such that a systematic row of diffraction spots or a two-dimensional array of diffraction spots appeared symmetrically on the fluorescent screen. The correct orientation of the fragment is critical for the formation of high quality lattice images.
- (e) At this stage an objective aperture was introduced to select a number of beams which were to contribute to the lattice image.



This aperture was carefully positioned as symmetrically as possible about the central undeviated beam.

(f) After switching to the imaging mode at high magnification and focussing the image, lattice fringes were observed on the screen.

(g) Using the binocular viewer, the lattice image was focussed as nearly as possible and at this point the final correction of the objective lens astigmatism was carried out.

(h) As it was difficult to observe the finest image detail directly on the screen, a through focus series of micrographs was generally recorded. By carefully selecting the illumination conditions it was possible to record images at 250,000 times magnification in exposure times of about five seconds or less.

By using this method, lattice images of 7-10 Å resolution were obtained routinely using the JEM 200 microscope and 4-5 Å resolution for the JEM 100C.

### 5.3 The Microstructure of NbO<sub>2</sub> Crystals

The structure of NbO<sub>2</sub> was discussed briefly in Chapter 4. However, a more detailed description of the structure is necessary for the discussion of the microstructural observations obtained by transmission electron microscopy.

Brauer (11) obtained X-ray diffraction data from powdered NbO<sub>2</sub> and was able to index most of the strong reflections on the basis of a tetragonal unit cell with a rutile type structure (Figure 5.2). However, the presence of additional weaker reflections suggested a superstructure which was eventually determined by Magneli et al (12). The structure proposed by Magneli is based on a tetragonal unit cell with  $a = 13.71 \text{ \AA}$   $c = 5.985 \text{ \AA}$  and containing 32 NbO<sub>2</sub> formula units. The NbO<sub>6</sub> octahedra share edges and corners as in the rutile structure and are arranged in

Fig. 5.2

The rutile-type unit cell

The high temperature form of  $\text{NbO}_2$  has the rutile ( $\text{TiO}_2$ ) structure. The diagram indicates the positions of the Nb and O atoms in the tetragonal unit cell. The Nb atoms are positioned at the centres of octahedra formed by the oxygen atoms.

Fig. 5.3

The arrangement of  $\text{NbO}_6$  octahedra

The  $\text{NbO}_6$  octahedra are arranged in chains as indicated in the diagram.

Fig. 5.4

The low temperature  $\text{NbO}_2$  structure

The low temperature form of  $\text{NbO}_2$  has a tetragonal unit cell which is based on an arrangement of slightly distorted rutile-type units shown in Fig. 5.2. The arrangement of the 16 rutile-type units to form the enlarged low temperature unit cell is indicated.

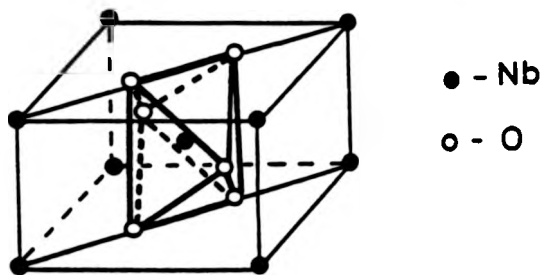


Fig. 5.2. The Rutile type unit cell.

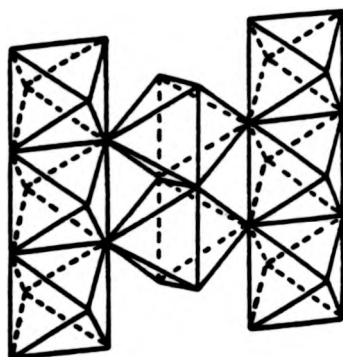


Fig. 5.3. The Rutile structure indicating the arrangement of  $\text{NbO}_6$  octahedra.

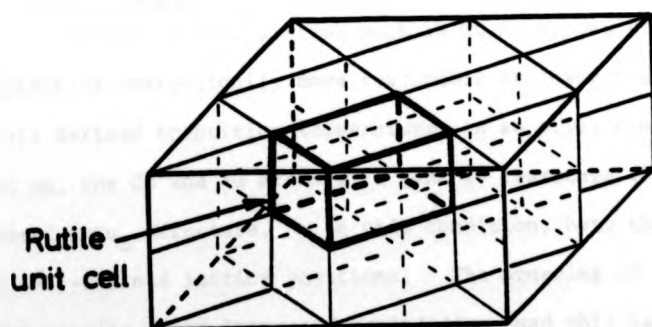


Fig. 5.4. The arrangement of Rutile-type units in the low temperature structure of  $\text{NbO}_2$ .

strings running in the C-axis direction (Figure 5.3). Within these strings, the distances between adjacent niobium atoms are alternately shorter (2.80 Å) and longer (3.20 Å). The relationship between the unit cell proposed by Magneli and the rutile unit cell is shown in Figure 5.4.

The use of a high temperature X-ray powder diffraction camera enabled Sakata et al (13,14), to demonstrate the existence of a structural phase transition at about 850°C. They found that below this temperature the X-ray diffraction data was consistent with the structure proposed by Magneli (12) but at temperatures above 900°C, the reflections corresponding to the superstructure were no longer present, suggesting a rutile type high temperature structure. A discontinuity in the expansion coefficient of the unit cell was also detected at about 800°C. This is approximately the same temperature at which a discontinuity in the electrical conductivity of NbO<sub>2</sub> has been observed (15). Since the periodic distortion of the rutile structure generates a low temperature structure with a unit cell of increased size, it is in many ways analogous to the order-disorder transformations which are observed in many materials and it is useful at this stage to explore some of these similarities. In a normal solid solution, atoms are randomly distributed on the atomic positions of the lattice. However in some systems such as Cu-Au alloys (16), an ordered arrangement is energetically more favourable at lower temperatures. Thus at a well defined transition temperature, in an alloy containing about 25 percent Au, the Cu and Au atoms will tend to rearrange themselves to form an ordered AuCu<sub>3</sub> structure. In this condition, both the Cu and Au atoms occupy well-defined lattice positions. The ordering of the random solid solution results in an increased periodicity, and this is generally described in terms of a superlattice.

Similar order-disorder transformations were observed in interstitial compounds such as vanadium carbide (17). In this case

above a certain transition temperature, a fraction of the interstitial sites are randomly occupied, but below the transition temperature, the interstitial atoms arrange themselves in an orderly fashion on the available sites. Again, the long-range ordering of the interstitial atoms increases the unit cell size and the structure of the ordered compound is again normally described in terms of a superlattice.

Now in the case of  $\text{NbO}_2$ , above the transition temperature the structure is rutile type. However on cooling it becomes advantageous for the structure to distort. The displacement of the atoms from their ideal rutile positions occurs with a well defined periodicity and consequently results in a low temperature unit cell of increased size. Therefore, although no movement of atoms between lattice sites occurs during the transformation a long-range ordering does take place and can be usefully described in terms of a superlattice. It is important to recognise that the transition in  $\text{NbO}_2$  is not an order-disorder transformation since the high temperature structure does not consist of a random arrangement of distorted rutile units.

In the discussions which follow the concept of a superlattice is frequently used and the extra reflections which occur in electron and X-ray diffraction work as a result of the extra ordering are referred to as superlattice reflections.

Common features observed by transmission electron microscopy of ordered structures arise because of mistakes in the periodicity. These features are referred to as antiphase boundaries (APB's) and will be described further in the following sections.

### 5.3.1 Electron diffraction

Single crystal electron diffraction patterns can readily be obtained from the thin edges of fragmented specimens of  $\text{NbO}_2$ . The use

of computed lists of interplanar spacings and angles facilitates the rapid indexing of these patterns. Some typical diffraction patterns are shown in Figure 5.5. In the schematic diagrams, the spots are indexed in terms of the unit cell proposed by Magneli. The most intense spots can also be indexed in terms of the basic rutile type unit cell as indicated. In Table 5.1 some of the strongest reflections are listed and indexed in terms of both the rutile type unit cell and the Magneli unit cell.

The less intense spots in the diffraction patterns of  $\text{NbO}_2$  arise as a consequence of the periodic displacement of atoms from their positions in the ideal rutile structure. Since only relatively small displacements are involved, the resulting diffraction spots have low structure factors. Again it is useful to compare this situation with the case of ordered compounds such as  $\text{CuAu}$ . In this case the superlattice reflections arise because the two species have slightly different scattering factors. Thus in the ordered state when each species is associated with particular lattice sites, extra reflections are allowed, but the structure factors will be low.

Thus in each case, the increased periodicity due to the ordering will result in the generation of extra, low-structure factor, diffracted beams.

In discussions of anti-phase boundaries, it is useful to index these superlattice reflections in terms of the basic subcell. Thus for  $\text{NbO}_2$ , a superlattice reflection can be indexed as  $\frac{m}{n}(\text{hkl})_R$ , where  $m$  and  $n$  are integers and  $(\text{hkl})_R$  represents a reflection which corresponds to the basic rutile structure. This convention simplifies the comparisons between the low temperature ordered structure and the basic rutile structure.

Fig. 5.5

Electron diffraction patterns for NbO<sub>2</sub>

The diffraction patterns illustrated were obtained from thin single fragments. The accompanying schematic diagrams show the principal reflections indexed. The indices refer to the tetragonal low temperature unit cell of NbO<sub>2</sub>.

The more intense spots in each of the patterns could also be interpreted as reflections arising from the rutile-type subcells.

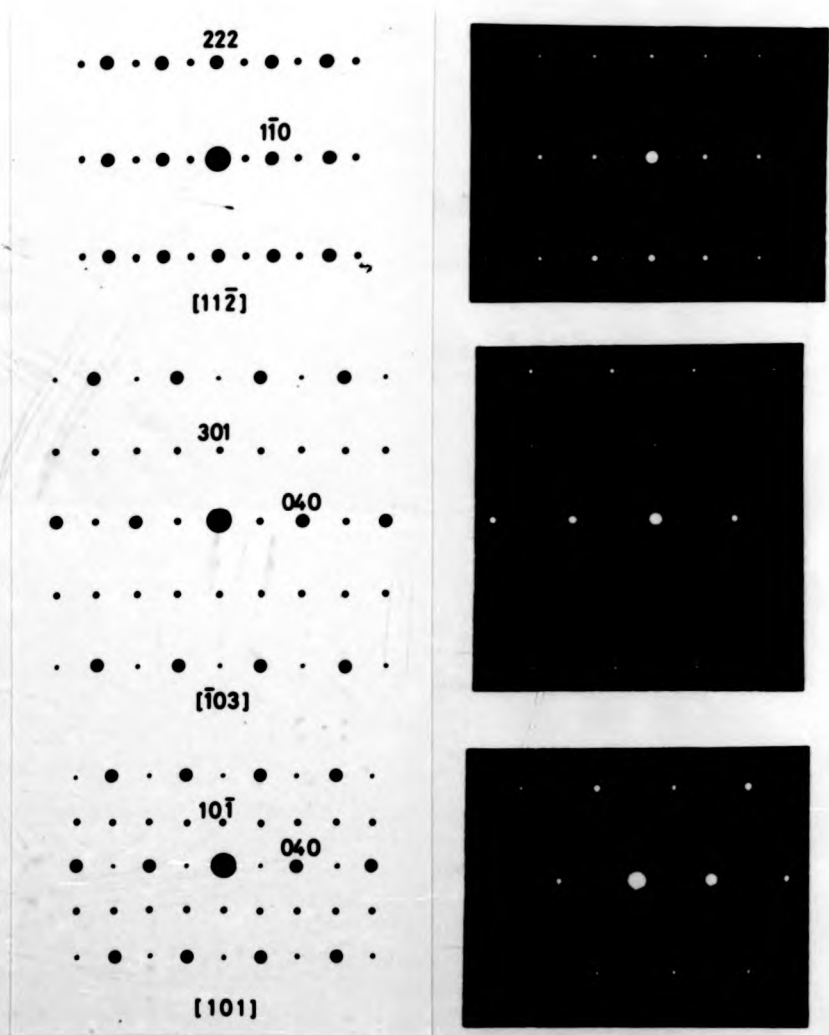


Figure 5.5 Electron diffraction patterns for NbO<sub>2</sub>



TABLE 5.1

DIFFRACTION DATA CONSISTENT WITH A RUTILE UNIT CELL

Interplanar spacing $d(\text{\AA})$	hkl ( $\text{NbO}_2$ structure)	hkl (rutile structure)
4.847	220	100
3.428	400	110
2.995	002	001
2.55	222	101
2.25	402	111
1.756	622	211

TABLE 5.1

DIFFRACTION DATA CONSISTENT WITH A RUTILE UNIT CELL

Interplanar spacing $d(\text{\AA})$	hkl ( $\text{NbO}_2$ structure)	hkl (rutile structure)
4.847	220	100
3.428	400	110
2.993	002	001
2.55	222	101
2.25	402	111
1.756	622	211

5.3.2 Contrast at antiphase boundaries

Images of APB's can be obtained in thin crystals of NbO<sub>2</sub> by bright or dark field imaging when a superlattice reflection is operating. A comprehensive treatment of antiphase structures has been given by Marcinkowski (18) but it is useful at this point to discuss briefly the contrast at APB's and to consider under what conditions they can be imaged.

In many ways an APB can be regarded as being similar to a stacking fault, and the observed contrast can be explained using the same arguments. Thus an APB which is inclined at an angle to the incident electron beam will exhibit fringe contrast when an appropriate superlattice reflection is operating. The principal difference in the contrast however is in the number of fringes which are observed for a given thickness of specimen. In general, images of APB's consist of only two or three fringes whereas stacking fault images often consist of many more. This difference in the numbers of fringes observed is a consequence of the different extinction distances.

The number of fringes, N, observed at an inclined planar feature imaged with g(hkl) as the operating reflection is given by:

$$N = \frac{t}{\xi_{g(hkl)}} \dots\dots\dots (18)$$

where t is the specimen thickness at the feature and  $\xi_{g(hkl)}$  is the extinction distance when g(hkl) is operating

The extinction distance  $\xi_{g(hkl)}$  has been given in Equation (5):

$$\xi_g = \frac{\pi V_c \cos \theta}{\lambda F_{g(hkl)}} \dots\dots\dots (5)$$

By inspection of these two equations, the number of fringes N should be proportional to  $F_{g(hkl)}$ , the structure factor for the operating diffraction beam. Now APB's are imaged using superlattice reflections

for which the structure factor is invariably low. Consequently the images consist of a low number of fringes. The operating reflections for the imaging of stacking faults are by comparison of much higher structure factor and a proportionally larger number of fringes is therefore observed.

As with stacking faults, at an APB there is a discontinuous displacement across one plane of atoms which results in a phase change,  $\alpha$ , in the electron waves which is given by:

$$\alpha = 2\pi \mathbf{g} \cdot \mathbf{R} \dots\dots\dots (19)$$

where  $\mathbf{R}$  is the displacement vector.

If this phase change,  $\alpha$ , has a value 0 or  $2n\pi$  (where  $n$  is an integer) then there will be no apparent change in the electron waves and the fault will not be observed. By determining under what diffraction conditions the fringes are visible or invisible, it is possible to determine  $\mathbf{R}$ , the antiphase displacement vector.

### 5.3.3 Antiphase boundaries in NbO<sub>2</sub>

Figure 5.6(a) ... (d) shows an area of NbO<sub>2</sub> containing antiphase domains imaged under different conditions. The operating reciprocal lattice vectors in each case are indexed in terms of the rutile subcell. This series of pictures shows that there were two distinct sets of APB's in this area which were imaged separately by selecting different diffraction conditions.

On the basis of a systematic study of the images obtained with different superlattice reflections operating, it was possible to deduce the possible antiphase vectors for the two types of APB. For the purpose of discussion, the APB's shown in Figure 5.6(a)(b)(c) will be referred to as Type 1 APB's with antiphase displacement vector  $\mathbf{R}_1$  and the APB's imaged in Figure 5.6(d) will be referred to as Type 2 with antiphase

Fig. 5.6

Anti-phase boundaries in NbO<sub>2</sub> crystals

Four typical micrographs taken from a region of an NbO<sub>2</sub> fragment are depicted. In each case the principal operating reflection is indicated. The individual diffraction patterns were not recorded.

5.6 (a) is a dark field image obtained using the  $\frac{1}{4}g(\bar{1}72)_R$  reflection. A number of boundaries are distinctly visible. 5.6 (c) is the corresponding bright field image with the same operating reflection and shows the same set of boundaries but with contrast reversed.

5.6 (b) is another dark field micrograph and the same set of boundaries are again in contrast. In this case the fragment has been tilted slightly to excite a different reflection.

In 5.6 (d) the dark field image has been recorded with yet another diffracted beam operating. In this case a different set of boundaries is in contrast.

In some of the micrographs in this series, the contrast effects cannot be simply interpreted on the basis of the simple 2-beam dynamical theory, and many beam effects must be invoked.

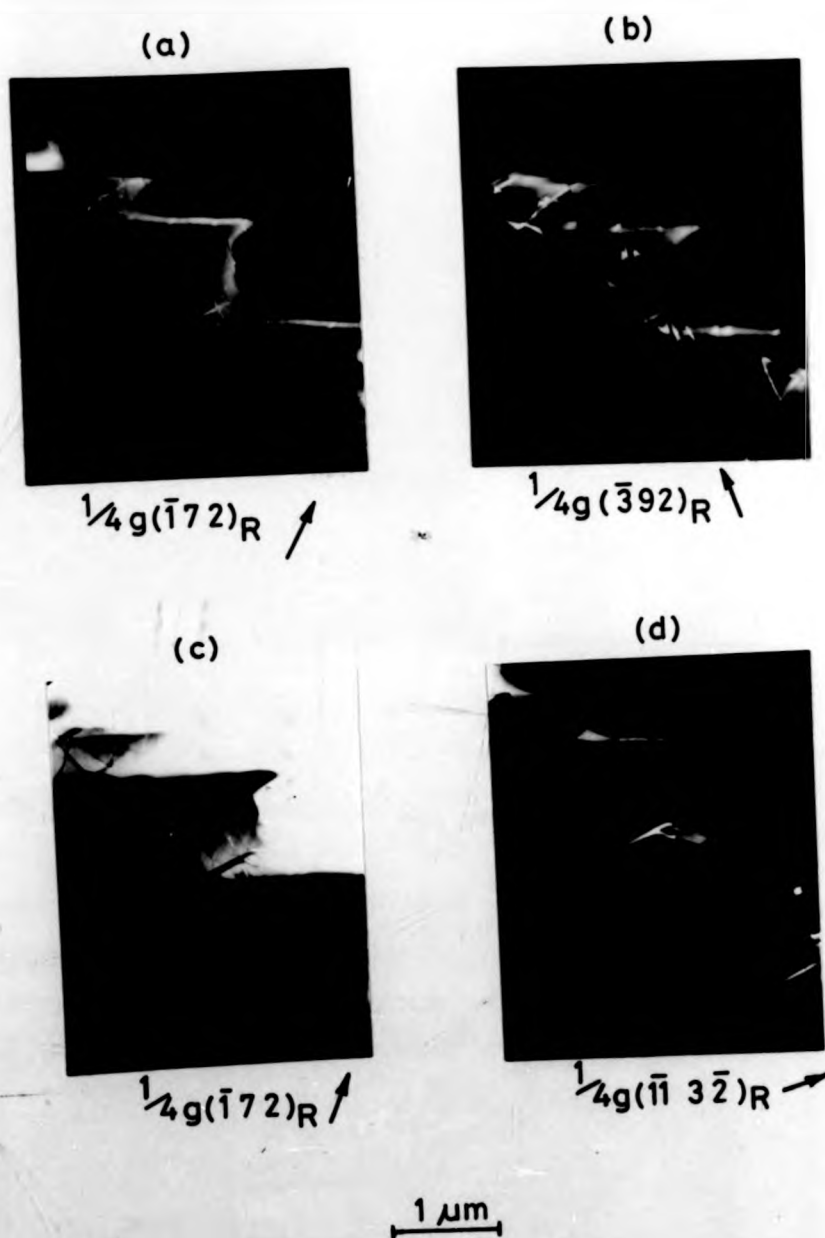


Figure 5.6 A.P.B.'s in  $NbO_2$  crystals imaged under different conditions

Fig. 5.7

Crystallography of the A.P.B.'s in NbO<sub>2</sub>

The low temperature unit cell of NbO<sub>2</sub> is shown in (a). The arrangement of rutile-type subcells is indicated (see Fig. 5.4). The  $[110]$  and the  $[11\bar{1}]$  lattice vectors are shown. (The indices in this case refer to the rutile subcell).

An anti-phase boundary with a  $[110]_R$  displacement vector is shown in (b). Similarly an A.P.B. with a  $[11\bar{1}]_R$  displacement vector is illustrated in (c).

Since in each case the displacement vectors are lattice vectors of the rutile sublattice, the arrangement of the rutile-type subcells is unchanged by the anti-phase boundary.

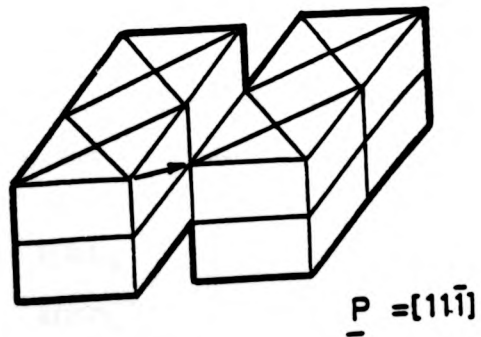
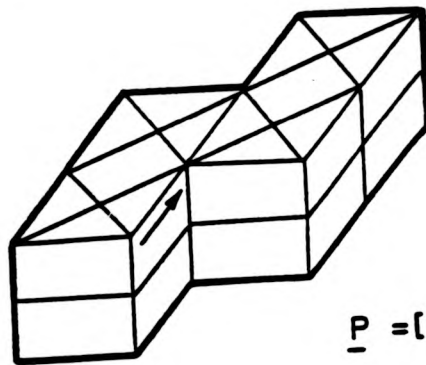
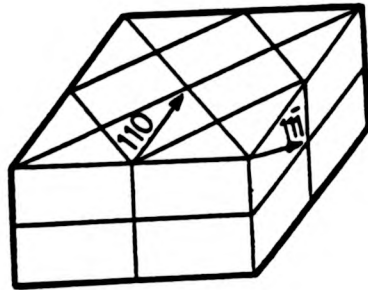


Fig. 5.7. APB's in  $\text{NbO}_2$



vector  $\underline{R}_2$ .

Considerations of several structurally possible antiphase vectors eventually leads to the conclusion that for each set of APB's two possible types of antiphase vector could explain the observed contrast. Table 5.2 is a list of the superlattice reflections together with the calculated phase angles,  $\alpha$ , for each of the possible values of  $\underline{R}_1$  and  $\underline{R}_2$ .

TABLE 5.2

g	$\alpha$ $\underline{R} = \langle 110 \rangle_R$	$\alpha$ $\underline{R} = \langle \bar{1}\bar{1}0 \rangle_R$	$\alpha$ $\underline{R} = \langle 11 \rangle_R$	$\alpha$ $\underline{R} = \langle \bar{1}\bar{1} \rangle_R$
$\frac{1}{2}(\bar{1}72)_R$	$3\pi$	$-4\pi$	$4\pi$	$3\pi$
$\frac{1}{2}(\bar{0}\bar{1}3\bar{2})_R$	$-4\pi$	$-7\pi$	$5\pi$	$-8\pi$
$\frac{1}{2}(\bar{3}92)_R$	$3\pi$	$-6\pi$	$4\pi$	$-5\pi$
$\frac{1}{2}(152)_R$	$3\pi$	$-2\pi$	$4\pi$	$-\pi$
$\frac{1}{2}(\bar{1}10)_R$	0	$-2\pi$	0	$-2\pi$

Whenever  $\alpha$  is an odd multiple of  $\pi$  the APB's corresponding to the antiphase displacement vector will appear in the appropriate dark field image.

As an example consider APB's with  $\underline{R} = [110]_R$ . The table shows that these APB's will be in contrast when the following superlattice reflections are selected to form the image:

$$\begin{aligned} &\frac{1}{2}(\bar{1}72)_R \\ &\frac{1}{2}(\bar{3}92)_R \\ &\frac{1}{2}(152)_R \end{aligned}$$

However when  $\frac{1}{2}g(\bar{0}\bar{1}3\bar{2})_R$  or  $\frac{1}{2}g(\bar{1}10)_R$  are operating, no contrast would be expected. These results correspond well to the observations of the type 1 APB's and so  $\underline{R}_1$  could take the value  $[110]_R$ . Similarly Type 2 APB's are only in contrast for  $\frac{1}{2}g(\bar{1}\bar{1}, 3\bar{2})_R$  and so referring to Table 5.2,

$R_2$  could take the value  $(1\bar{1}0)_R$ .

The results presented so far however are also consistent with values of  $R_1 = [1\bar{1}1]_R$  and  $R_2 = [111]_R$ . An example of each of the families of possible APB's is shown schematically in Figure 5.7.

At this point it is useful to discuss the arrangements of APB's in  $NbO_2$ . Consider first the case when the antiphase vector lies in the plane of the APB. This simply represents the gliding of the structure on one side of the fault plane relative to the structure on the other side. In substitutional or interstitial ordered phases this will not result in any change in the local composition of the material and so such a fault is commonly termed a conservative APB. However, in the general case when the displacement vector is not parallel to the fault plane, the situation is not as simple.

To maintain the integrity of the crystal structure, the displacement of the region on one side of the fault plane in a direction which does not lie in this plane, requires the incorporation or removal of one or more planes of atoms. Now in for example a substitutional ordered compound, the association of the different atomic species with specific sites may mean that these planes of atoms are richer in one of the species. Such a boundary would not therefore maintain the stoichiometry of the ordered phase and consequently could be referred to as a non-conservative APB.

In  $NbO_2$ , however, the low temperature ordered structure arises because of the periodic displacement of the atoms from their ideal rutile type positions. At an APB in such a structure this periodicity is disrupted and so the displacements of the atoms on one side of the interface are not consistent with the ordered structure on the other side. Thus the interatomic distances at an APB will be non-ideal.

Clearly these APB's in no way affect the stoichiometry of the material even in cases for which the antiphase vector does not lie in the fault plane. It can therefore be misleading to refer to these APB's in  $\text{NbO}_2$  as conservative or non-conservative defects. In this discussion of APB's it is worthwhile pointing out that the closely related titanium dioxide (rutile) crystal structure can accommodate a type of APB which has not so far been observed in  $\text{NbO}_2$  crystals. In slightly reduced  $\text{TiO}_2$ , non-conservative APB's occur which correspond to the removal of planes of oxygen atoms (19). The incorporation of such faults in the rutile ( $\text{TiO}_2$ ) structure represents an important mechanism for the accommodation of non-stoichiometry and it is the formation of these defects which explains the extended phase field of  $\text{TiO}_2$ .

Although  $\text{NbO}_2$  has a crystal structure which is closely related to the rutile structure, the composition range is very restricted. This implies that the shear plane mechanism for the accommodation of non-stoichiometry is not effective in  $\text{NbO}_2$  crystals. Thus it is not surprising that such defects have not been observed.

#### 5.3.4 The formation of antiphase domains in $\text{NbO}_2$

Antiphase domains separated by antiphase boundaries occur in crystals as a consequence of mistakes in the long-range ordered structure. Such faults in the periodicity can arise in several possible ways. For example:

- (a) in  $\text{NbO}_2$ , the passage of a dislocation with a Burger's vector appropriate to the rutile subcell would generate an antiphase boundary on its slip plane,
- (b) during growth, mistakes in the generation of new layers may lead to the formation of antiphase boundaries,
- (c) during the transformation from the high temperature, rutile type structure to the low temperature long-range ordered structure,

the ordering may be initiated at several points in the crystal. As the transformation proceeds the ordered regions will grow consuming the regions which still retain the high temperature structure. As the process nears completion, adjacent ordered regions meet and if the long-range ordering is out of step in the two regions, the interface will be an antiphase boundary. If however, the two regions are indistinguishable then the two growing domains will coalesce to form a larger antiphase domain, or (d) if a dislocation exists in the high temperature structure, then, depending on its Burger's vector, when the crystal is cooled through the transformation temperature, an antiphase boundary will be formed. Figure 5.8 shows diagrammatically the generation of an APB by such a mechanism.

To determine which of these mechanisms is responsible for the formation of APB's in  $\text{NbO}_2$  it is necessary to examine carefully their shape and character.

It is significant that the vast majority of the APB's observed during this study either formed closed continuous loops or terminated at the edge of the crystal. This observation suggests that in general the APB's were not associated with dislocations. In fact only a few isolated examples of dislocations have been observed in  $\text{NbO}_2$ . Figure 5.9 shows an area containing "superdislocations". A superdislocation consists of a dissociated pair of dislocations such that their individual Burger's vectors correspond to lattice vectors of the subcell, but that their combined Burger's vectors add up to correspond to a superlattice vector. The pair of dislocations is therefore connected by an antiphase boundary. Again the analogy with stacking faults and partial dislocations is useful. The superdislocations

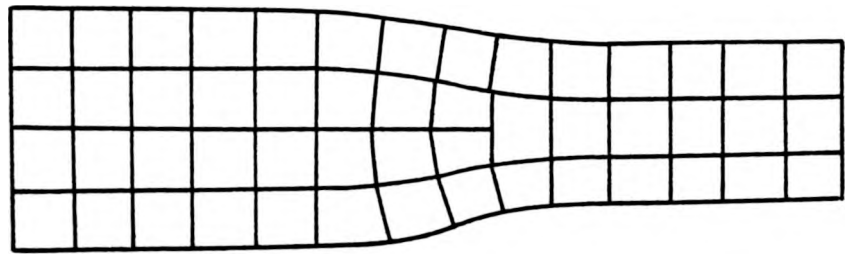
Fig. 5.8

The generation of an A.P.B. by a dislocation

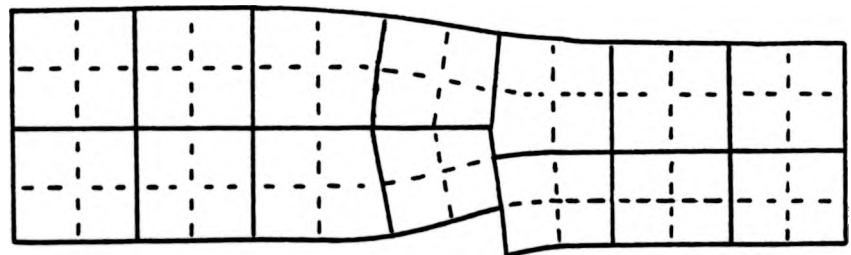
The upper diagram shows schematically the arrangement of unit cells in a region of the crystal containing a dislocation.

The lower diagram is a similar region in which the structure can be regarded as an ordered arrangement of the smaller, dotted unit cells. In this case the burgers vector of the dislocation does not correspond to a unit cell parameter of the ordered structure and thus an anti-phase boundary results.

As indicated in the diagram, the transformation to a longer range ordered structure will result in A.P.B.'s which terminate at dislocations.



↓ transformation



↑ APB

Fig. 5. 8. APB generated by a dislocation.

Fig. 5.9

Superdislocations in NbO<sub>2</sub> crystals

This transmission electron micrograph of a fragment of an NbO<sub>2</sub> single crystal shows a number of "paired" dislocations. Such pairs of dislocations are characteristic of long range ordered structures and are known as superdislocations.

The individual components of the superdislocations each have burgers vectors which correspond to sublattice vectors. Thus the passage of such a dislocation through the crystal generates an A.P.B. However, the summed burgers vectors of the components are equivalent to superlattice vectors and therefore the second component of the superdislocation restores the long range order. Hence the defects can be considered as two sublattice dislocations which are separated by an A.P.B.



0.5  $\mu\text{m}$

**Figure 5.9 Superdislocations in  $\text{NbO}_2$  crystals**



observed here are almost certainly artefacts, due to the fragmentation technique of specimen preparation. Since the crystals of  $\text{NbO}_2$  were grown at a temperature above the transformation temperature, the observed antiphase boundaries cannot be regarded as manifestations of growth accidents.

Thus the most likely explanation of the antiphase domains is that they were generated as the crystals cooled through the transformation temperature by a process of nucleation and growth.

#### 5.4 Electron Microscopy of the $\text{Nb}_{12}\text{O}_{29}$ Crystals

Norin (20,21) used single crystal X-ray techniques to determine the structures of both orthorhombic  $\text{Nb}_{12}\text{O}_{29}$  and the monoclinic form. He obtained the single crystals from arc-melted pellets and by a chemical transport method. The structures which he deduced were the same as those proposed by Wadsley (22) for the two polymorphic forms of  $\text{Ti}_2\text{Nb}_{10}\text{O}_{29}$ .

The structures of the two forms of  $\text{Nb}_{12}\text{O}_{29}$  have already been described in some detail (see Chapter 4).

The orthorhombic form has four formula units per unit cell with

$$\begin{aligned} a &= 28.90 \pm 0.02 \text{ \AA} \\ b &= 3.835 \pm 0.002 \text{ \AA} \\ c &= 20.72 \pm 0.02 \text{ \AA} \end{aligned}$$

The monoclinic unit cell proposed by Norin also contains four formula units with

$$\begin{aligned} a &= 31.32 \pm 0.05 \text{ \AA} \\ b &= 3.832 \pm 0.006 \text{ \AA} \\ c &= 20.72 \pm 0.04 \text{ \AA} \\ \beta &= 112^\circ 93' \end{aligned}$$

The structures of both of these polymorphs can be described in terms of blocks of  $\text{NbO}_6$  octahedra ( $4 \times 3 \times \infty$ ). It has already been

pointed out that such "block structure" oxides are eminently suitable for investigation by high resolution electron microscopy. By carefully orienting the crystal so that the electron beam direction is parallel to the column direction (i.e. the b-axis direction) the arrangement of the columns can be directly observed and any irregularities in the arrangement of the blocks can be studied.

Several such studies of the microstructure of  $\text{Nb}_{12}\text{O}_{29}$  have been conducted and various types of defects have been observed.

Iijima et al (23) studied  $\text{Nb}_{12}\text{O}_{29}$  prepared by the controlled oxidation of  $\text{NbO}_2$  and observed both planar and "point" defects. The planar defects were parallel to the c-axis and corresponded to mistakes in the orthorhombic arrangement of the blocks. These faults can be considered to be microdomains of the monoclinic modification one unit cell in width. As these faults merely involve local rearrangements of the structure, there is no associated change in the stoichiometry. However, the "point" defects (really line defects parallel to the b-axis) which were observed were interpreted as being due to the incorporation of Nb-O complexes into the structure. Faults of this type do result in a local change in the stoichiometry.

In another study Hutchison et al (24) observed twinning in monoclinic  $\text{Nb}_{12}\text{O}_{29}$  crystals. The details of sample preparation were not given in this work, although it is believed that the crystals were grown by a chemical transport method (25).

The object of this study is to relate high resolution microstructural observations of the  $\text{Nb}_{12}\text{O}_{29}$  specimens to the growth of the crystals.

#### 5.4.1 Electron diffraction

In the crystals which were grown by the chemical transport of a powder with starting composition equivalent to  $\text{NbO}_2$ , all the electron diffraction patterns which were obtained could be indexed in terms of the orthorhombic unit cell of  $\text{Nb}_{12}\text{O}_{29}$ . Thus the crystals which were selected for electron microscopy had clearly been grown under conditions which favoured the growth of the orthorhombic form of  $\text{Nb}_{12}\text{O}_{29}$  rather than the monoclinic.

Figure 5.10 (a)(b) shows some typical electron diffraction patterns of orthorhombic  $\text{Nb}_{12}\text{O}_{29}$ . Figure 5.10(c) is a similar diffraction pattern taken from a different fragment and in this example there is a distinct streaking of the diffraction spots along  $g(100)$  indicating the possible existence of faulting on planes parallel to the  $c$  axis. Patterns which exhibited streaking were frequently observed, particularly for crystals which had been grown at a rapid rate, and consequently one would expect to find a high density of faults in such crystals.

#### 5.4.2 Lattice imaging of $\text{Nb}_{12}\text{O}_{29}$

Using the tilt facilities of the electron microscope, thin fragments of the  $\text{Nb}_{12}\text{O}_{29}$  crystals could be oriented such that the diffraction pattern consisted of rows of  $h00$  diffraction spots as shown in Figure 5.10(a). By carefully tilting the specimen until these rows of spots were symmetrical about the centre and by inserting a suitable objective aperture to select several of the beams, a one-dimensional lattice image of the structure could be formed.

Figure 5.11 shows such an image taken from a thin bent crystal of  $\text{Nb}_{12}\text{O}_{29}$ . The position of the objective aperture which was used in the formation of these images is indicated on the diffraction pattern in Figure 5.12. The variations in orientation of the buckled

Fig. 5.10

Electron diffraction patterns for Nb<sub>12</sub>O<sub>29</sub>

The first two diffraction patterns are the [ 001 ] and the [ 010 ] patterns and can be indexed as shown in the accompanying diagrams.

The other diffraction pattern is also an [ 010 ] zone axis pattern but in this case many of the spots are streaked parallel to  $g(200)$  indicating the presence of planar defects on the  $\{200\}$  planes.

..... 010 .....

..... 200 400 .....

.....

[001]

..... 002 .....

..... 001 .....

..... 200 400 .....

.....

.....

[010]

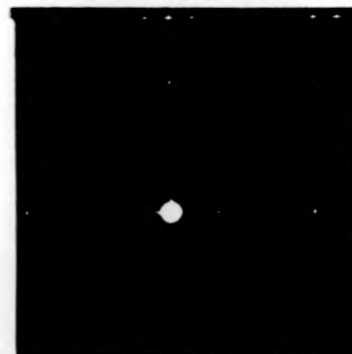
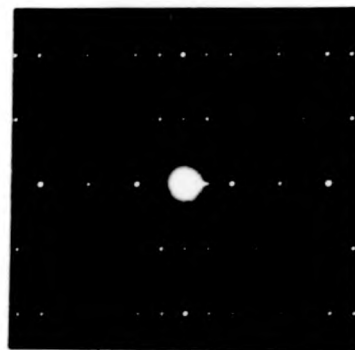
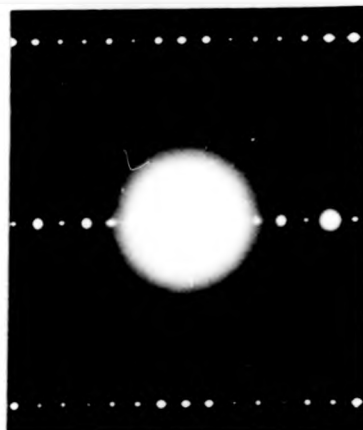


Figure 5.10 Electron diffraction patterns for Nb<sub>12</sub>O<sub>29</sub>

Fig. 5.11

1-d lattice image of a bent region of  $\text{Nb}_{12}\text{O}_{29}$

This micrograph illustrates some of the contrast effects which can complicate the interpretation of lattice images. The lattice fringes imaged correspond to the  $28.9 \text{ \AA}$ , (100), lattice spacing of  $\text{Nb}_{12}\text{O}_{29}$ .

In the regions arrowed, the thickness and the orientation of the fragment are such that the  $14.45 \text{ \AA}$  (200) fringes can be seen.

The shift of the fringes as they cross extinction contours is also clearly illustrated.

Fig. 5.12

The imaging conditions used for lattice imaging of  $\text{Nb}_{12}\text{O}_{29}$

This electron diffraction pattern obtained from part of the area shown in Fig. 5.11 has the outline of the objective aperture superimposed to indicate which of the reflections contributed to the image. In this case some of a systematic row of (h 0 0) diffraction spots were used.



1000 Å

Figure 5.11 - 1-d lattice image of a bent region of Nb<sub>12</sub>O<sub>29</sub>

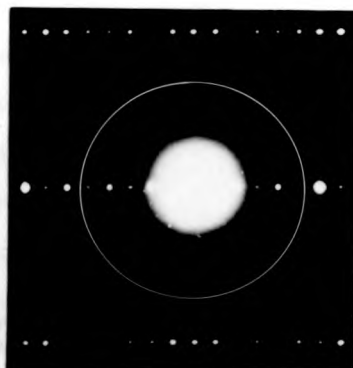


Figure 5.12 Electron diffraction pattern showing the position of the objective aperture used for lattice imaging

crystal over the field of view cause changes in the fringe contrast and spacing as predicted by Hashimoto's dynamical treatment of lattice images (3). As well as these orientation dependent contrast effects it is also apparent that the differences in thickness also change the appearance of the lattice fringes. For example, in the regions arrowed, the 14.45 Å spacing is clearly resolved, whereas over most of the field of view only the 28.9 Å fringes are in good contrast. Again this is further evidence that dynamical effects need to be considered for the correct interpretation of lattice images.

Figure 5.13(a)(b) show lattice images obtained from relatively undistorted regions of an  $\text{Nb}_{12}\text{O}_{29}$  fragment. Again the imaging conditions which were used were similar to the conditions indicated in Figure 5.12. The principal fringes have the 28.9 Å spacing corresponding to the orthorhombic unit cell dimension.

Intermediate fringes are also visible in some areas and these correspond to the spacing of the "shear" planes which separate the (4 x 3 x ∞) blocks.

The images shown here contain a high density of planar defects of various types. Careful measurement of the faults labelled (A) on the micrographs, shows that the fringes on either side of the fault plane are shifted with respect to one another by about 14.5 Å. This would be consistent with the assumption that these faults are equivalent to the insertion or removal of a single plane of (4 x 3 x ∞) blocks. These faults have been observed by Iijima et al (23) in  $\text{Nb}_{12}\text{O}_{29}$  crystals prepared by the controlled oxidation of  $\text{NbO}_2$ .

Figure 5.14(a)(b) depicts the two possible arrangements of the structural blocks at these defects.

Both types of these defect are illustrated in Figures 5.13 and marked A or B. The micrographs clearly show the differences in



Fig. 5.13

Lattices images of faulted regions of an  $\text{Nb}_{12}\text{O}_{29}$  crystal

In the two regions illustrated examples of four apparently different types of fault can be found and are labelled types A - D.

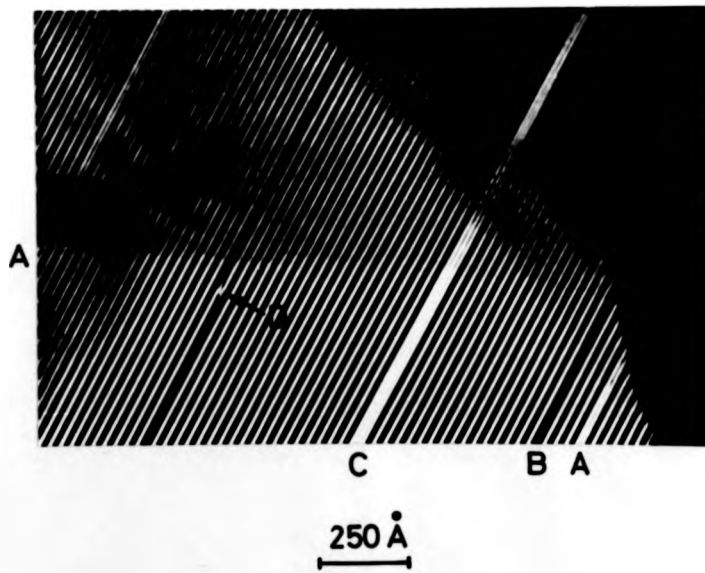
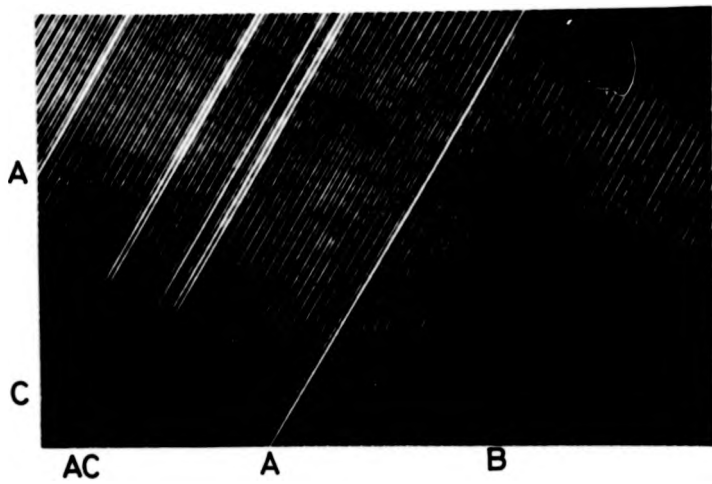
At type A faults, two regions of regular lattice fringes are displaced with respect to one another by about  $14.5\text{\AA}$  and an extra bright fringe is incorporated.

Type B defects are very similar except that the  $14.5\text{\AA}$  discrepancy is accounted for by the incorporation of an extra dark fringe.

Defects of type C are also similar in appearance to type A, but in this case several extra fringes are incorporated. Although the type C defects shown here are only 3 or 4 fringes in width, other similar areas have been observed with faults up to 9 fringes wide.

Generally defects of types A, B and C are continuous over large distances. However occasionally faulting of these defects has been observed. The feature labelled D shows such a fault in a type B defect.

The detailed structure of these defects is discussed in the text.



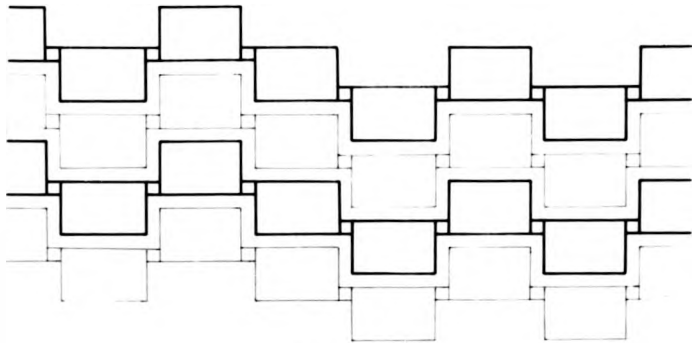
**Figure 5.13** 1-d lattice images of faulted regions of  $\text{Nb}_{12}\text{O}_{29}$

Fig. 5.14

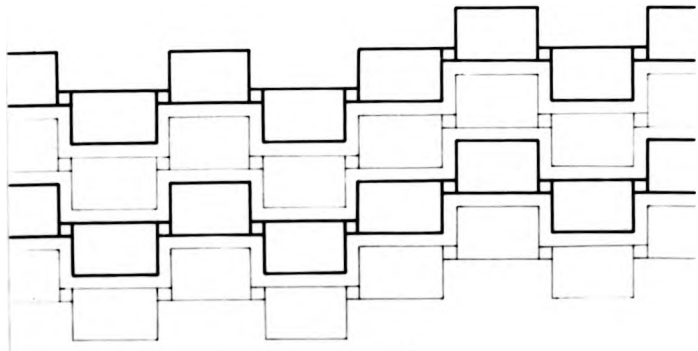
The arrangement of blocks at faults in  $\text{Nb}_{12}\text{O}_{29}$

The schematic diagrams show the arrangement of blocks at faults of type A and B. In each case the faults can be considered as an extra plane of  $4 \times 3$  blocks. Inspection of the two types shows them to be related enantiomorphically. However the lattice images display different contrast since they are not enantiomorphic with respect to the beam direction.

These faults can also be thought of as microdomains of monoclinic -  $\text{Nb}_{12}\text{O}_{29}$ , one unit cell thick.



↑  
A



↑  
B

Figure 5.14 Schematic diagrams showing the arrangements of blocks at faults in  $Nb_{12}O_{29}$

contrast which occur depending on the nature of the fault. These faults can be regarded as a type of stacking fault or as microdomains of the monoclinic form of  $\text{Nb}_{12}\text{O}_{29}$ , only one unit cell wide. The faults marked C in the micrographs (Figure 5.13) are examples of larger microdomains of monoclinic  $\text{Nb}_{12}\text{O}_{29}$ .

Generally the lattice fringes of  $\text{Nb}_{12}\text{O}_{29}$  observed in this way were continuous and straight, terminating only at the edges of the crystal fragment. This also was generally true of the planar defects. However, a few isolated examples of discontinuities in the fault planes were observed. One such feature is illustrated in Figure 5.13(b) and labelled D. In this region there is a distinct step in the fault plane. Examination of the fringes and faults in the vicinity of this feature shows that it is not simply a contrast effect but is structural. Figure 5.15 shows a possible arrangement of blocks at such a defect. If this interpretation is correct it requires the presence of an oversized ( $6 \times 4 \times \infty$ ) block. The origin of these defects will be discussed presently.

If the specimen can be tilted until the beam direction coincides with the [010] direction in the crystal, a two-dimensional lattice image can be formed. In this case, the objective aperture is positioned symmetrically about the centre spot so that beams of the  $h00$  type and the  $00l$  type are selected (Figure 5.16). Figure 5.17 shows a two-dimensional lattice image of orthorhombic  $\text{Nb}_{12}\text{O}_{29}$  obtained in this way. The  $4 \times 3$  blocks are clearly resolved and in some regions the structure within the blocks can be distinguished (Figure 5.18). In these cases the bright spots correspond to the tunnels between  $\text{NbO}_6$  octahedra. Consequently the  $4 \times 3$  blocks appear as a  $3 \times 2$  array of bright spots.

Fig. 5.15

A possible arrangement of blocks at a  
type D fault in Nb<sub>12</sub>O<sub>29</sub>

The lattice image in Fig. 5.13 shows that a fault of type D occurs when a type A fault suffers a displacement. The arrows in the diagram show the positions of the type A fault indicating the displacement. Such a displacement could be accommodated by the incorporation of the shaded block as shown.

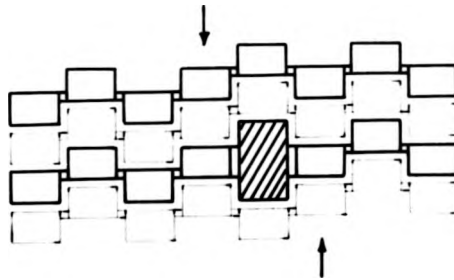


Figure 5.15 The possible arrangement of blocks at a type D fault in  $Nb_{12}O_{29}$

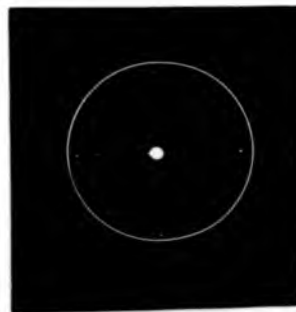


Figure 5.16 [010] diffraction pattern for Nb<sub>12</sub>O<sub>29</sub> showing the position of the objective aperture for lattice imaging





Figure 5.16 [010] diffraction pattern for Nb<sub>12</sub>O<sub>29</sub> showing  
the position of the objective aperture for  
lattice imaging

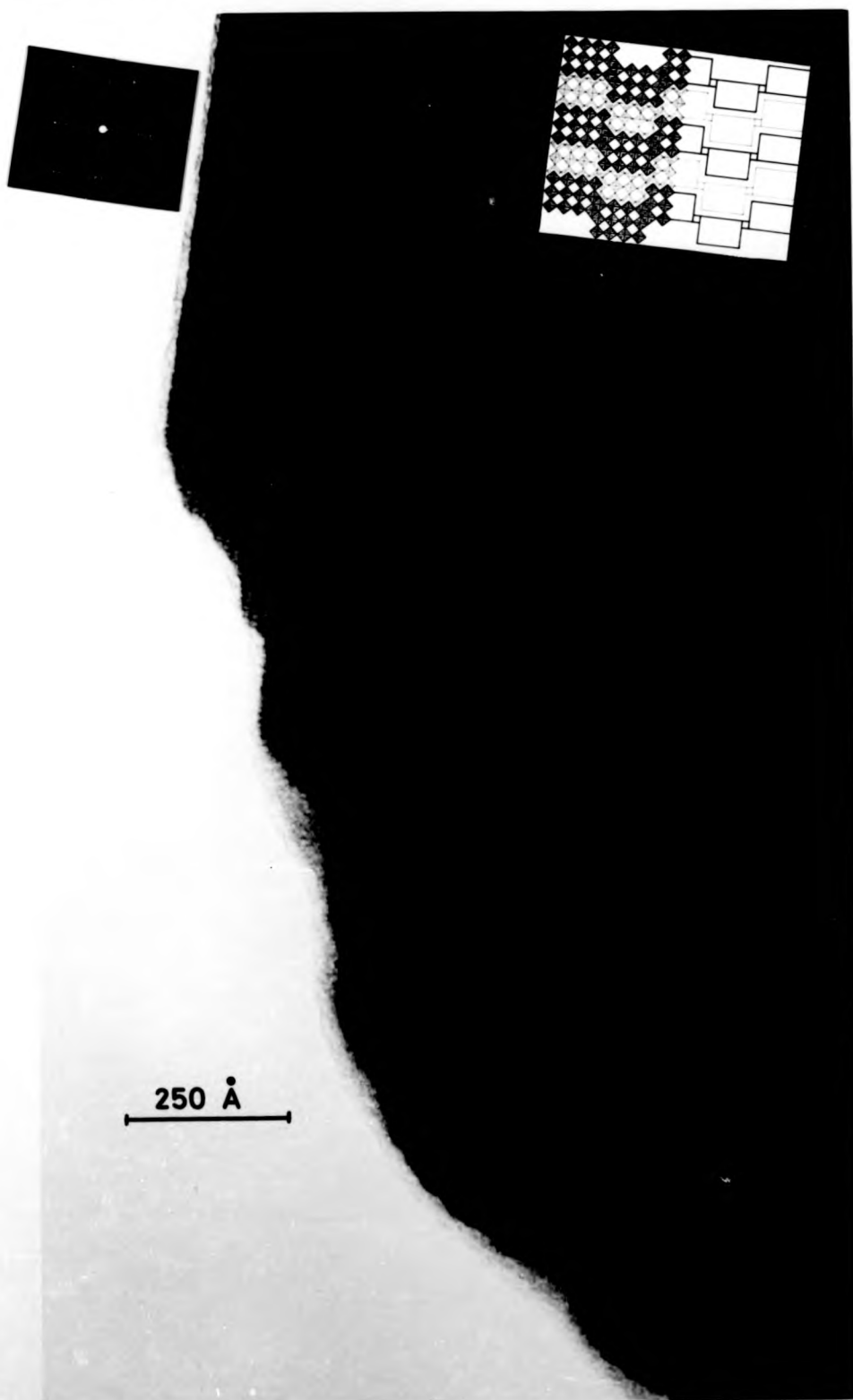
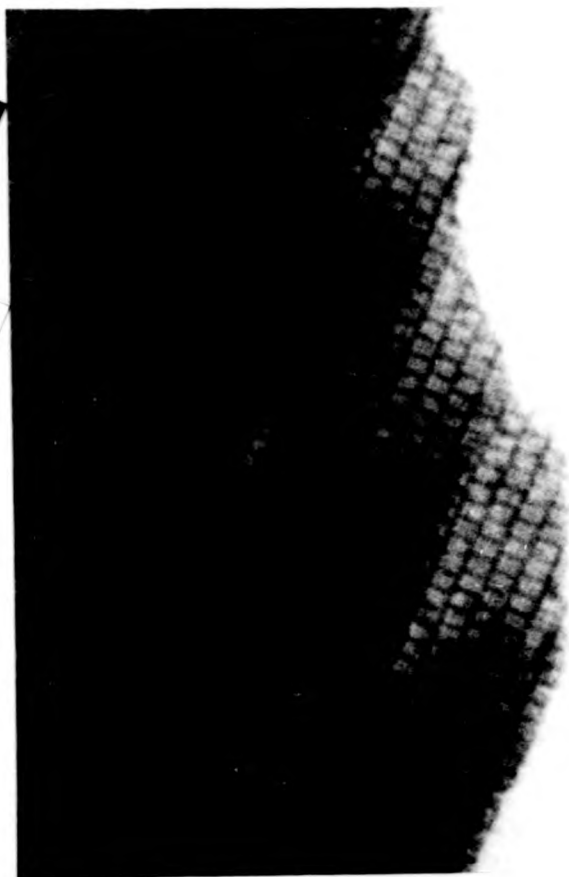


Fig. 5.17. Lattice image of ortho-Nb<sub>2</sub>O<sub>5</sub>



100Å

Figure 5.18 High magnification image of  $\text{Nb}_{12}\text{O}_{29}$  showing the structure within the blocks

#### 5.4.3 The generation of defects in Nb<sub>12</sub>O<sub>29</sub> crystals

It has already been established by X-ray techniques that the principal growth axis of the Nb<sub>12</sub>O<sub>29</sub> crystals is along [010]. When viewed in the [010] direction, the lattice images of the as-grown crystals indicate that each new layer of NbO<sub>6</sub> octahedra exactly overlaps the previous layer. This is true even when the crystals contain the planar defects already described. Now the specimens used for lattice imaging are typically of the order of 100 Å thick and since each layer of octahedra is 3.84 Å thick, the areas of interest correspond to about 30 layers. Of the many samples of Nb<sub>12</sub>O<sub>29</sub> observed in this way, no evidence of any mistakes in this layer growth has been observed and this implies that the occurrence of faults parallel to the (010) planes is very rare. Faults of this type have been observed in block structure oxides prepared from the melt (26) and these features manifest themselves in lattice images as dark areas. This is because when such a fault occurs, some of the tunnels between octahedra on one side of the faults are overlapped by octahedra on the other side.

The frequency of observation of the planar defects on (100) planes (features A and B in Figures 5.13) indicates that they are low energy faults. This fact and the occurrence of microdomains of monoclinic Nb<sub>12</sub>O<sub>29</sub> several unit cells across indicates that the monoclinic form is only slightly less stable than the orthorhombic form under the growth conditions used.

Since no observations of such faults terminating within the crystal and only a few isolated examples of steps in these faults have been recorded (figure D in Figure 5.13) it would seem that in general once such a defect has nucleated it propagates through the crystal creating a complete planar fault.

In the previous chapter evidence was presented to indicate that new growth layers on the (100) planes were generated by the action of screw dislocations concentrated at the twin boundary. The images shown in Figure 5.13 show that in that particular crystal a mistake in the orthorhombic block stacking sequence occurs approximately every twenty layers. Now, if several nucleation sites are responsible for the generation of new layers then one would expect that as the faulted layer grew it would eventually encounter normal layers originating from another growth centre and where this occurred the fault would be terminated. Such an event could explain the existence of the type D fault in Figure 5.13 (b). However, observations of such faults are extremely unusual in the crystals studied and therefore it can be concluded that the spacing between the active growth centres on the (100) planes is large compared to the areas observed in the electron microscope. In fact, measurements of many areas suggest that this spacing is on average at least 25  $\mu\text{m}$ .

It is interesting to note that in all the areas studied, no examples of faults parallel to the (001) planes have been observed. New layers on these planes emanate from the TPRE sites and it is useful to consider in more detail the nucleation process at such sites. A schematic diagram of the TPRE region is shown in Figure 5.19.

The block structure of  $\text{Nb}_{12}\text{O}_{29}$  again results in the (001) surface of the crystal being decorated with a series of parallel steps. However, unlike the (010) surface, there are no positions on these steps equivalent to the kink sites described in Section 4.3.1. Thus atoms arriving at the (001) surface quickly diffuse to step site positions, but only those which subsequently diffuse along the steps to the more favourable TPRE sites are captured. The nucleation of a new block at the TPRE is illustrated in Figure 5.19. The spacing of the steps on the (001) surface will restrict the maximum dimension of new blocks in the [100] direction because it is

Fig. 5.19

Initiation of new growth blocks at the TPPE

This diagram represents the arrangement of 4 x 3 x ∞ columns in the  $\text{Nb}_{12}\text{O}_{29}$  crystals at the TPPE. The crystal surfaces each have a series of parallel ledges and where these intersect at the TPPE, favourable positions occur for the addition of new growth units. A small block of new growth is shown boldly outlined.

parallel  
ourable  
its.  
ned.

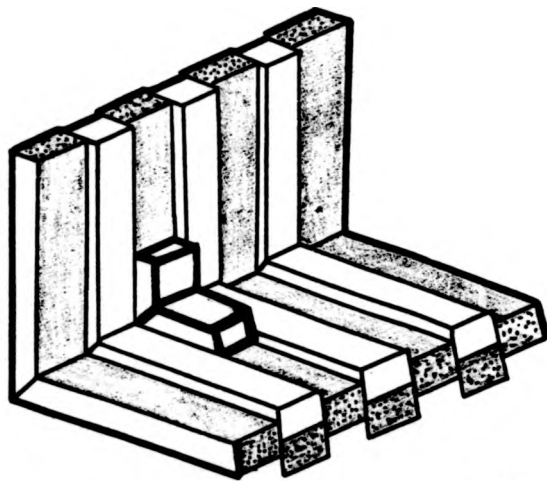


Fig. 5.19. Initiation of a new block at the TPRES

structurally impossible for a coherent  $\text{ReO}_3$  type block to develop beyond either of the two limiting steps between which it was nucleated. However, no such structural limitations apply to the block dimension in the [001] direction.

Having discussed the growth of  $\text{Nb}_{12}\text{O}_{29}$  crystals in some detail it is appropriate at this point to consider the morphologically similar crystals of as yet undetermined stoichiometry which were obtained by chemical transport using  $\text{Nb}_{12}\text{O}_{29}$  as the source material (see Sec. 2.10).

#### 5.5 Oxides of Undetermined Stoichiometry

The crystals which were grown using  $\text{Nb}_{12}\text{O}_{29}$  as the source material were blue/black in colour and were generally obtained in the form of thin twinned plates, strongly resembling the  $\text{Nb}_{12}\text{O}_{29}$  crystals in appearance. Examination in the electron microscope, however, reveals that the microstructure of these crystals is in many respects very different from the idealised  $\text{Nb}_{12}\text{O}_{29}$  structure.

##### 5.5.1 Electron diffraction and high resolution electron microscopy

Lattice images were obtained for these crystals by tilting the specimens until the electron beam direction coincided with the column direction of the block structure. In this orientation the diffraction pattern obtained is shown in Figure 5.20. The diffuse and streaked nature of the diffraction spots in this pattern indicates a highly faulted structure and this is confirmed by the high resolution lattice images.

Figure 5.21 shows a typical image obtained from a fragment of this material and the highly disordered block structure is clearly resolved. An image from another fragment (Figure 5.22) shows that although large disordered regions are present, there are some large regions which show a high degree of order. The regions labelled A in



Fig. 5.20

Diffraction pattern obtained from  
the "disordered" crystals

This diffraction pattern consists of a number of well defined spots which are associated with diffuse streaking.

This streaking indicates a highly faulted structure.

of  
ise

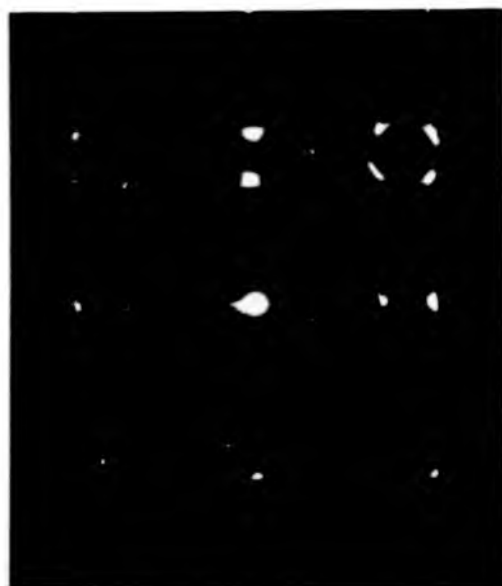


Figure 5.20 Diffraction pattern obtained from the disordered  
crystals

Fig. 5.21

High resolution electron micrograph of  
a disordered block structure region

In this region the structure consists of an arrangement of  $\text{ReO}_3$  type blocks of different sizes. The variations in block size, linkage and density of tetrahedral Nb sites indicates local variations in stoichiometry.



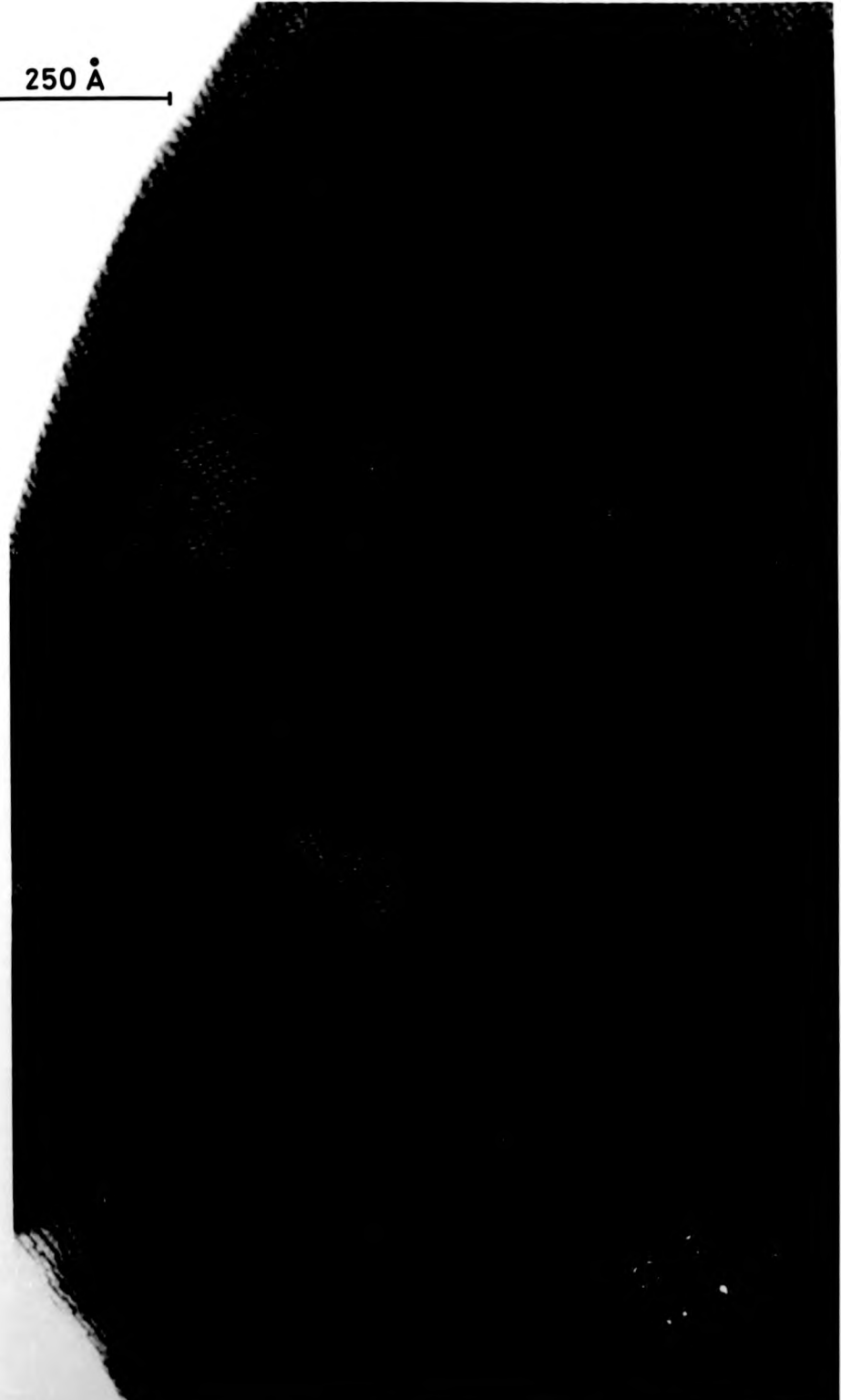
Fig. 5. 21. Disordered block structure.

Fig. 5.22

Domains of  $\text{Nb}_{22}\text{O}_{54}$  in a "disordered" crystal

In this micrograph the lattice imaging technique reveals the presence of domains of  $\text{Nb}_{22}\text{O}_{54}$  structure within the "disordered" crystal.

250 Å

An electron micrograph showing a large, dark, roughly triangular domain of a crystal. The domain is oriented with its hypotenuse towards the top-left. The interior of the domain shows a fine, granular texture. A horizontal scale bar is located in the upper left quadrant of the image, consisting of a line with vertical end caps and the text '250 Å' centered above it.

que  
ure

Fig. 5.22. Part of a "disordered" crystal containing large domains of  $\text{Nb}_{21}\text{O}_{24}$

Figure 5.22 correspond to domains of  $\text{Nb}_{22}\text{O}_{54}$ . This arrangement has been observed by Iijima (27) and is shown schematically in Figure 5.23.

Smaller domains of other ordered arrangements have also been observed in this material and the region shown in Figure 5.24 can be represented diagrammatically by the block diagram, Figure 5.25.

Such a region corresponds to an oxide phase with composition  $\text{Nb}_{31}\text{O}_{79}$  with a monoclinic unit cell with:

$$\begin{aligned} a &= 41.5 \text{ \AA} \\ b &= 3.83 \text{ \AA} \\ c &= 39.5 \text{ \AA} \\ \beta &= 73^\circ \end{aligned}$$

A careful examination of the disordered regions of Figures 5.22 and 5.23 reveals a wide variation in possible block sizes; (3 x 3) blocks are frequently observed and occasionally large blocks of up to (6 x 3) have been found (a (6 x 3) block is indicated by arrow B in Figure 5.22).

Blocks of similar sizes are often observed grouped together in domains. Figure 5.26(a) shows such a region which contains a number of above-average sized blocks. Again the arrangement of the blocks is indicated in a block diagram (Figure 5.26(b)).

Despite the disordered appearance of the region, the blocks are almost invariably rectangular and the orthogonality of the  $\text{ReO}_3$  type parent structure is maintained. The disordering occurs by the variations in block sizes and by the incorporation of randomly distributed tetrahedrally coordinated Nb atoms. The structural variations observed will obviously be accompanied by variations in the stoichiometry of the crystal.

Fig. 5.23

The idealised Nb<sub>22</sub>O<sub>54</sub> structure

The schematic diagram shows that the structure consists of (4 x 3) blocks and (3 x 3) blocks with Nb atoms in the tetrahedral sites.



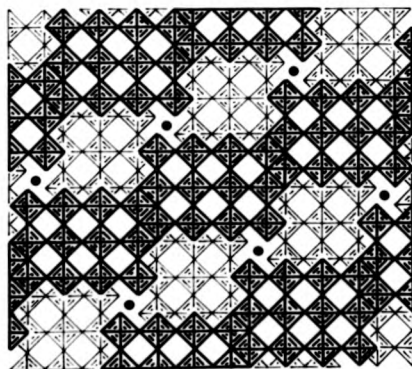


Figure 5.23 The idealised Nb<sub>22</sub>O<sub>54</sub> structure

Fig. 5.24

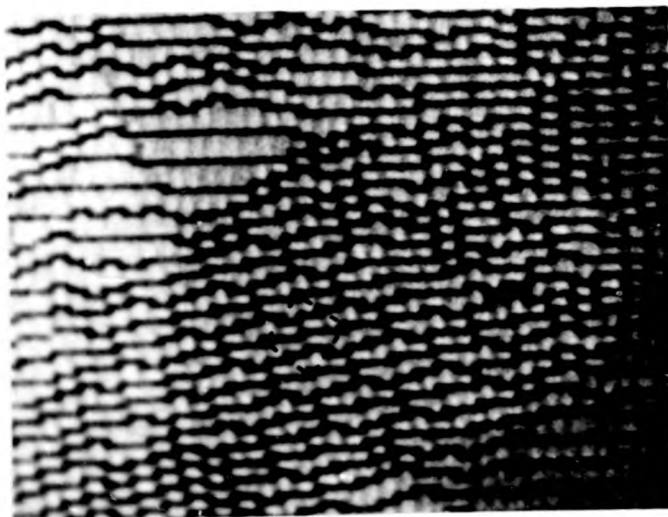
An ordered microdomain in the disordered crystal

This micrograph shows part of an area of disordered structure which contains a microdomain of an ordered block structure. The unit cell of the ordered structure is indicated.

Fig. 5.25

Schematic diagram of the ordered block structure

This block diagram shows the arrangement of structural units which constitute the ordered structure shown in Fig. 5.24.



50 Å

Figure 5.24 A region containing a small domain of an ordered block arrangement

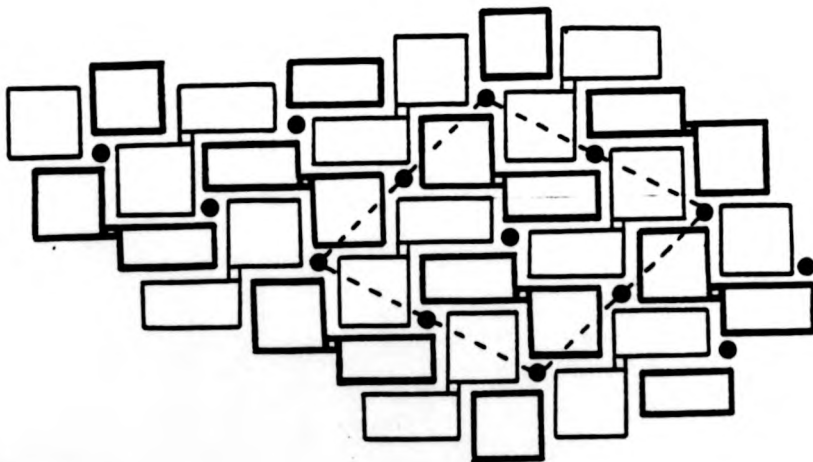
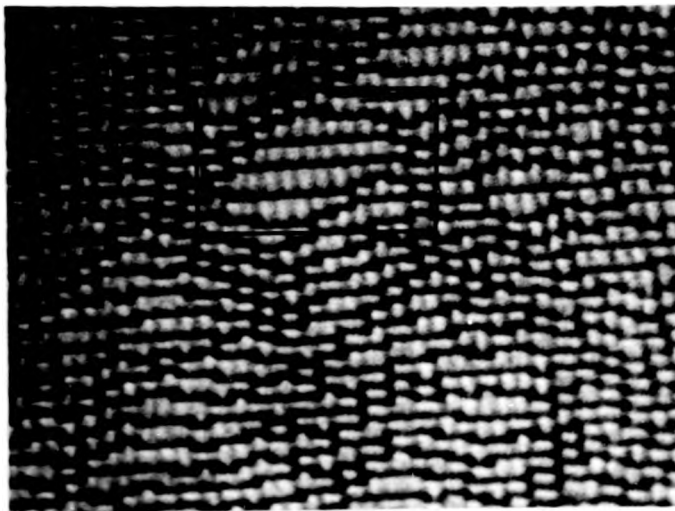


Figure 5.25 A diagram showing a possible arrangement of the blocks

Fig. 5.26

Region containing a number of unusually large blocks

The micrograph (a) shows the disordered structure and a region of abnormally large structural blocks is outlined. The schematic arrangement of these blocks is indicated in (b).



50 Å

Figure 5.26 (a) Disordered region containing large blocks

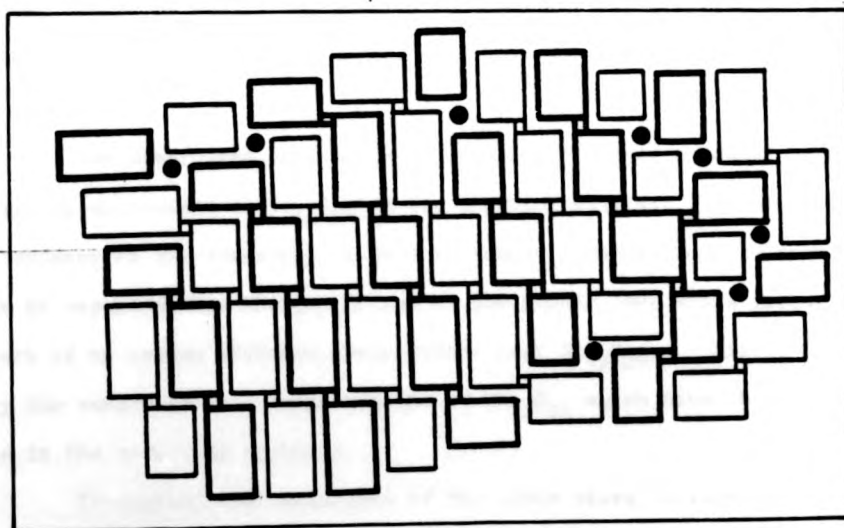


Figure 5.26 (b) Diagram of the arrangement of blocks

cs  
re  
is  
s

### 5.5.2 Evidence relating to the growth of these crystals

Despite the fact that the crystals described above show a high degree of disorder with wide variations in block sizes and block linkage arrangements, no evidence of any faults with a component parallel to the (010) planes has been found. Indeed, the fact that lattice images can be obtained from large areas of crystal up to several hundred Angstroms thick indicates that each successive layer of the structure faithfully reproduces the previous layer during growth in the [010] direction. Thus, once a block of a certain cross section has formed it will grow in the [010] direction maintaining this cross-section. To explain the development of an irregular block structure it is therefore necessary to discuss the generation of new blocks on the (h0l) type faces of the crystal.

The similarities in the growth behaviour of these disordered crystals and the orthorhombic  $\text{Nb}_{12}\text{O}_{29}$  crystals indicates that in each case growth occurs by similar mechanisms. The structural differences may be accounted for by considering the growth rates and vapour compositions in each case.

The disordered crystals were obtained by using a powder with a composition equivalent to  $\text{Nb}_{12}\text{O}_{29}$  as the starting material, and because of the tendency of the transport reagent to remove niobium from the system, it might be expected that the conditions at the growth zone would favour the growth of an oxygen enriched phase rather than  $\text{Nb}_{12}\text{O}_{29}$ . This is probably the reason for the large domains of  $\text{Nb}_{22}\text{O}_{54}$  which have been observed in the resulting crystals.

To explain the variations of the block sizes it is necessary to reconsider and modify the mechanisms proposed for the growth of  $\text{Nb}_{12}\text{O}_{29}$ .

Consider first the generation of new blocks at the TPPE sites.

The fact that no faults have been observed on (100) planes in  $\text{Nb}_{12}\text{O}_{29}$  supports the supposition that the new blocks which are generated on these surfaces are strongly influenced by the substrate layer. In fact it would appear that new blocks are constrained to grow with the dimension in the [100] direction exactly matching the substrate. An examination of the structure of the surface clearly shows that it would be impossible for a new block to exceed this [100] dimension of the substrate structure, although if the growth conditions were suitable, the incorporation of smaller blocks into the structure seems feasible. This could give rise to the occurrence of tetrahedral sites as indicated in Figure 5.27.

This diagram also shows how the incorporation of a smaller block might result in the generation of a site suitable for a larger than normal block in the next layer. It has already been pointed out in the discussion of  $\text{Nb}_{12}\text{O}_{29}$  crystals that there are no structural constraints on the dimensions of blocks in the [001] direction. However, the range of block sizes which can be generated in this way will be restricted because of the long-range interatomic forces.

It is interesting to note that although this mechanism gives a plausible explanation for the generation of blocks of various sizes it implies that the number of blocks on the growing (001) face will be conserved. In other words each exposed substrate block will eventually nucleate a single new block. This must be so since the blocks are separated by shear planes on (100), and it is therefore impossible for a single coherent  $\text{ReO}_3$  type block to grow over two or more adjacent substrate blocks.

Examination of the high resolution micrographs shows that this condition is satisfied and that although the shear planes meander due to the variations in block size they are nevertheless continuous across the field of view in the [001] direction and the number of blocks in

Fig. 5.27

A possible mechanism to explain the incorporation of  
"wrong sized" blocks into the crystal structure

The schematic diagram (1) shows the block arrangement at the growing surface. New blocks may grow on this surface as indicated by the shaded blocks in (2). Normally the blocks will maintain the crystal structure. However, variations in the vapour composition, impurity effects or temperature fluctuations may lead to the formation of smaller blocks.

In order to maintain the integrity of the structure further growth layers will also have "wrong sized" blocks as shown in (3).

This sequence demonstrates how smaller blocks, larger blocks and tetrahedral sites can arise during crystal growth.



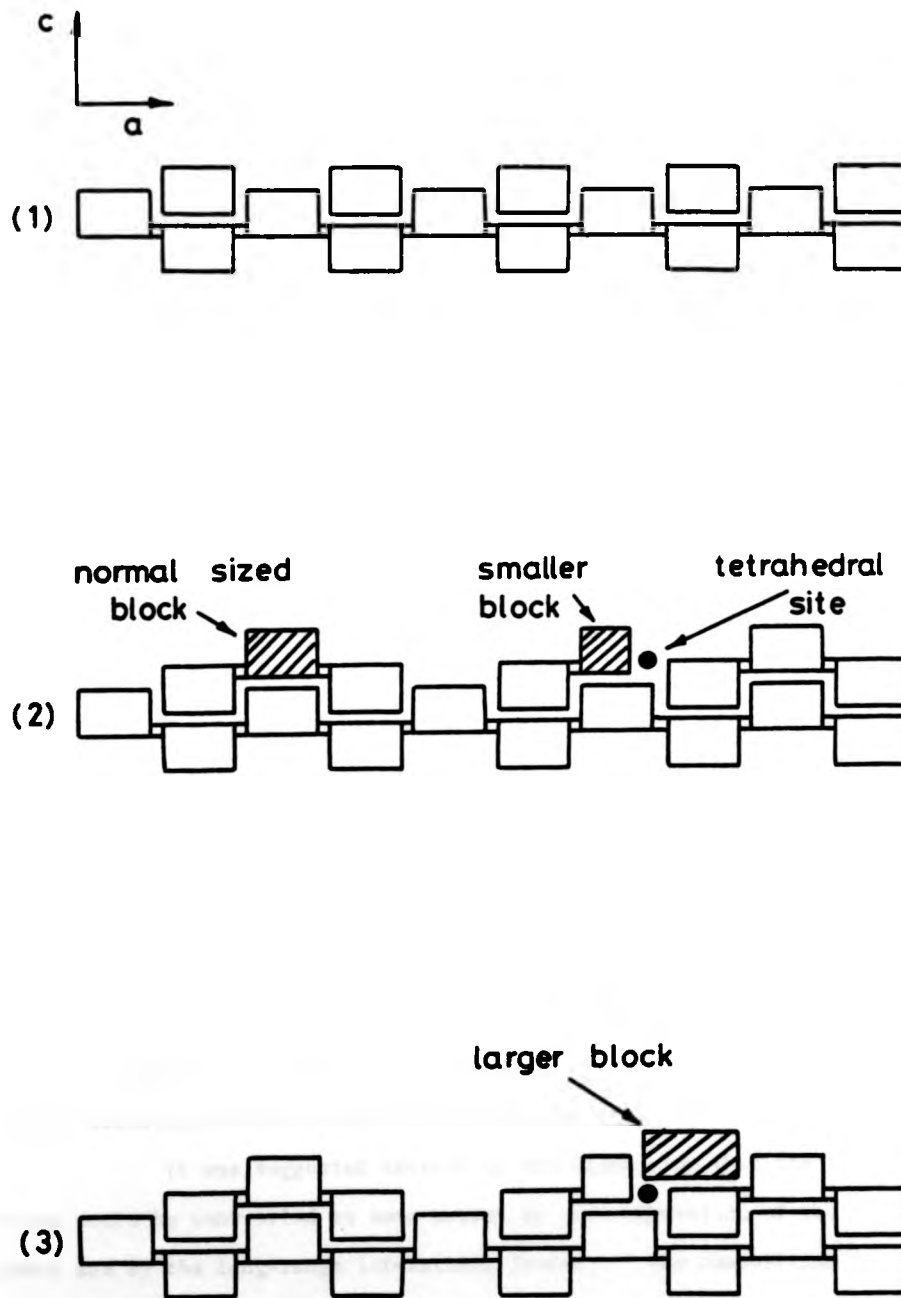


Fig. 5.27. A possible mechanism for the incorporation of "wrong sized" blocks.

successive layers is conserved.

The growth of  $\text{Nb}_{12}\text{O}_{29}$  type crystals in the [100] direction seems to occur principally by the propagation of dislocation generated steps.

Consider the progress of a step on a (100) face in the [001] direction and assume that the step height is equivalent to the dimension of the block in the [100] direction. The addition of a new block to such a step will be influenced by the structure of the surface to which it is attaching itself and by the structure of the step. For example, it is unlikely that a new block of a size which would increase the step height would be added, although it would not seem unreasonable for a smaller block to be added. Thus as a step propagates it would be expected to either maintain a constant height, or to decrease in height by a series of discrete steps corresponding to changes in block size equivalent to the dimension of one  $\text{NbO}_6$  octahedron ( $\approx 4 \text{ \AA}$ ).

The propagation of a series of such steps might therefore be expected to result in a distribution of block sizes as shown in Figure 5.28.

Again this arrangement of blocks compares favourably with the structures observed in the electron microscope.

Thus both the TPPE mechanism and the step growth mechanism can account for the incorporation of blocks of varying sizes into the crystal structure. However in each case it is important to consider the growth conditions which could lead to the nucleation of such blocks.

It was suggested earlier in the discussion that the block sizes would be controlled to some extent by the composition of the vapour phase and by the long-range interatomic forces. The composition of the vapour will determine both the growth rate and the stoichiometry of the crystal and the interatomic forces will tend to impose a long-range order on the block structure if possible.

Fig. 5.28

Block size variations during step growth

This diagram depicts the possible arrangement of blocks which might occur during the growth of successive layers (1-4) in the C direction.

As the first layer of blocks is deposited, (layer 1), the step height is either maintained or decreased (by units of  $\text{NbO}_6$ ) octahedra.

The subsequent growth layers (2-4) exhibit a similar behaviour, except that the steps which occur in the substrate layer can result in increases in block size.

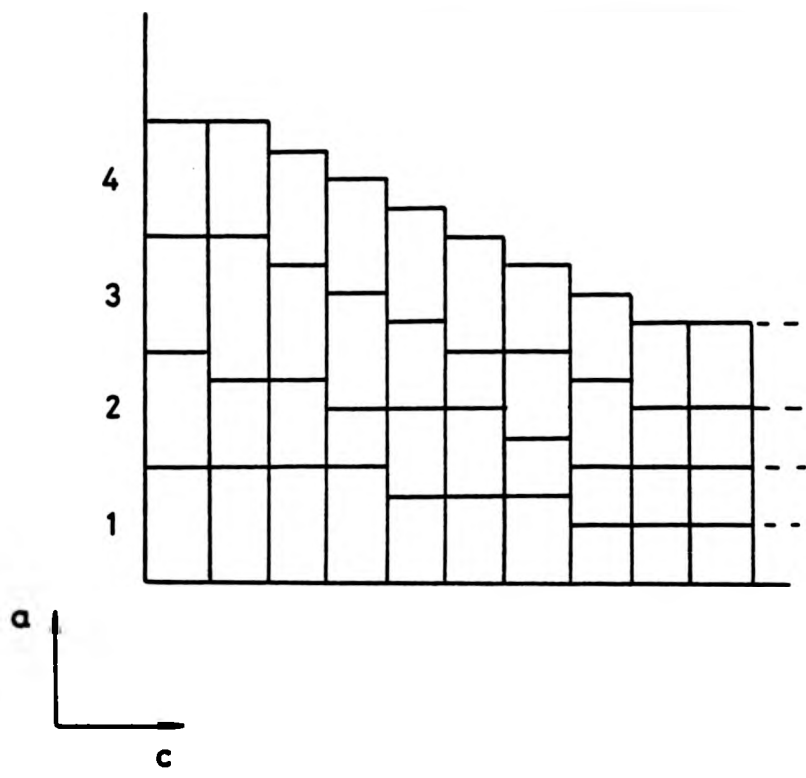


Fig. 5.28. Variations in block size which could occur during the propagation of steps.

Of the block structure oxides  $Nb_{12}O_{29}$  has the highest Nb-O ratio. Now the  $Nb_{12}O_{29}$  crystals grew from a vapour phase with a high Nb-O ratio since the source material for the process was  $NbO_2$ . Deviations of the block structure from the ideal  $Nb_{12}O_{29}$  structure are almost invariably non-conservative, and decrease the Nb-O ratio, therefore because of the composition of the vapour such deviations would not be favourable.

When the  $Nb_{12}O_{29}$  is used as the source material for chemical transport however, the tendency of the vapour phase to gradually become enriched in "Nb" favours the growth of oxide phases with compositions between  $Nb_{12}O_{29}$  and  $Nb_2O_5$ . Several crystal phases have been identified in this composition range, having different arrangements of different sized blocks. It has been established that the stability of these phases is particularly sensitive to variations in the oxygen partial pressure (28,29). Consequently small changes in the composition of the vapour phases during growth could easily result in changes in block size and linkage arrangements. Thus if the growth rate is reasonably rapid so that structural rearrangements on the growing surface cannot occur, "wrong sized" blocks will be incorporated into the crystal structure.

#### 5.6 The Microstructure of H-Nb<sub>2</sub>O<sub>5</sub> Crystals

The H-form of  $Nb_2O_5$  has probably been one of the most thoroughly studied of all the niobium oxides. Being the thermodynamically stable phase at high temperatures it can easily be prepared by several techniques. For example, Iijima (30) used specimens, quenched from the melt for his high resolution studies of lattice defects in H-Nb<sub>2</sub>O<sub>5</sub>. Anderson, Browne and Hutchison (31) used crystals prepared by chemical transport with  $NbCl_5$  as transporting agent and for their work on the related  $MgF_2$ - $Nb_2O_5$  system (32) the material was produced by sintering a mixture of powders at 1270°K for 160 hr followed by rapid quenching to

room temperature. In all these cases the use of HREM has enabled the detailed structures of many lattice defects to be observed and analysed.

The most commonly reported defects were twin lamellae often only one unit cell in width, the twin plane invariably being  $(10\bar{1})$ . However several other types of defect have been observed involving irregularities in the block linkage structures or small domains of "wrong-sized" blocks. In the material prepared by quenching from the melt, large areas of heavily faulted structure were observed (30) being unusual arrangements of blocks and occasionally abnormally shaped blocks.

The defect structure of the crystals of  $\text{H-Nb}_2\text{O}_5$  grown by the methods described in Chapter 2 has been investigated and will be discussed in the following sections.

#### 5.6.1 Electron diffraction and lattice imaging

Figure 5.29(a) is a  $[010]$  diffraction pattern of a thin fragment of  $\text{H-Nb}_2\text{O}_5$ . Again the circle indicates the position of the objective aperture and the number of diffracted beams which contribute to the lattice images.

Figure 5.30 is an example of a two-dimensional lattice image formed in this way and the details of the block structure can be resolved and several defects can be identified.

The most commonly observed defects in these crystals are twin lamellae, often only one unit cell wide. The block structure of such a defect is depicted in Figure 5.31.

In some of the fragments examined much larger twinned regions were observed. An example of a macroscopic twin is shown in Figure 5.32. A diffraction pattern obtained from a twinned region of this type is shown in Figure 5.29(b). The extra spots in the pattern can be clearly seen.

The structure of the twin boundaries in these vapour grown



(a) pattern from a 'perfect' region of crystal showing the position of the objective aperture used for lattice imaging

---



(b) pattern from a twinned region showing the extra 'twin' spots

---

Figure 5.29 Diffraction patterns for H-Nb<sub>2</sub>O<sub>5</sub>

Fig. 5.30

A lattice image of a faulted region of  $\text{H-Nb}_2\text{O}_5$

In this micrograph, the individual (4 x 3) and (5 x 3) structural blocks are resolved as white rectangles. The array of dark spots corresponds to the arrangement of tetrahedrally co-ordinated Nb atom sites. Careful inspection reveals the presence of a large number of structural faults.



les.  
of  
ection  
ults.

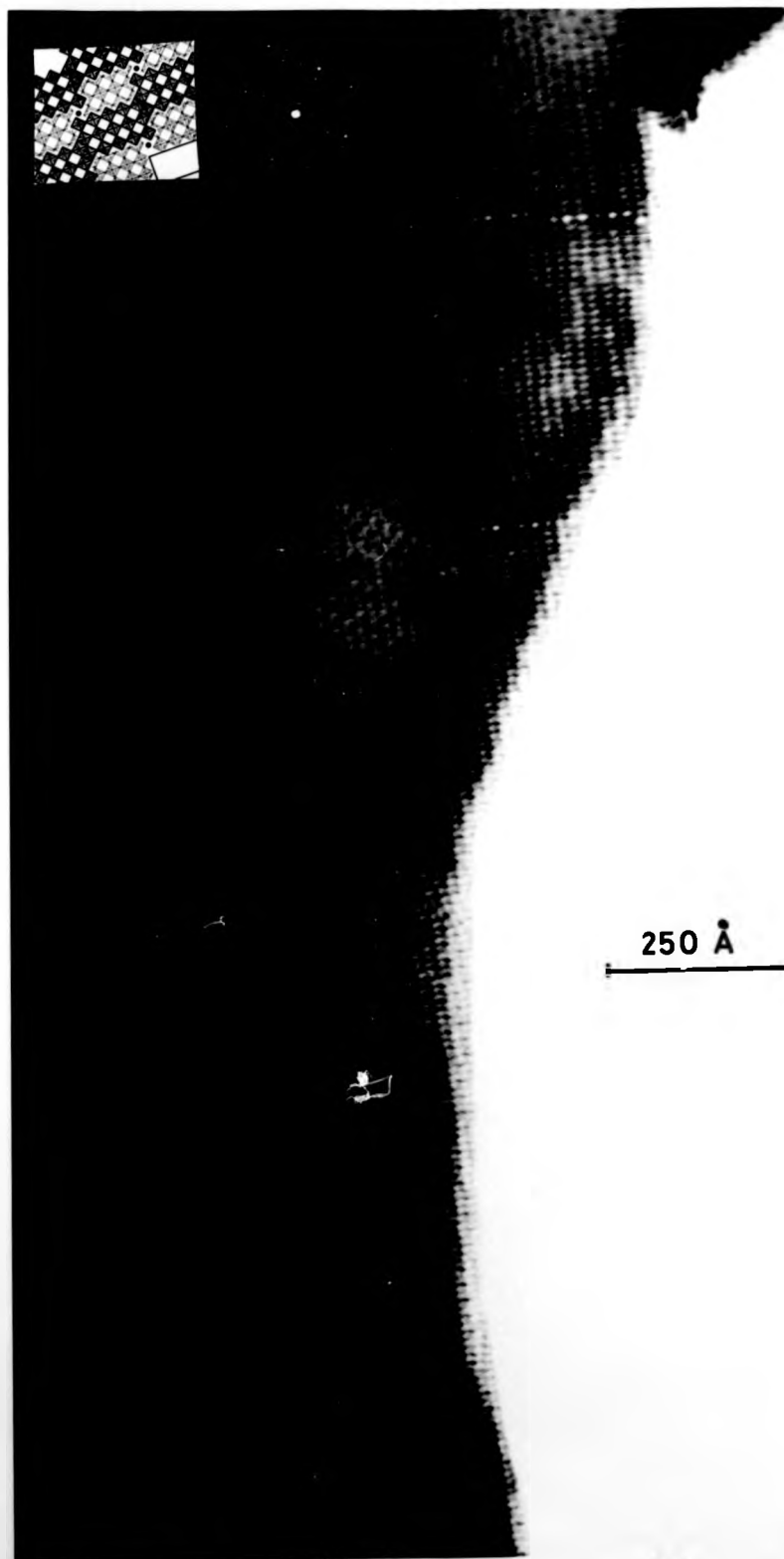


Fig. 5.30. Area of H-Nb<sub>2</sub>O<sub>5</sub>, containing various types of faults.

Fig. 5.31

A twin lamella in H-Nb<sub>2</sub>O<sub>5</sub>

The fault plane arrowed in the lattice image can be identified as a twin lamella of the type shown in the block diagram. Faults of this kind were frequently observed in the vapour grown crystals.



100 Å

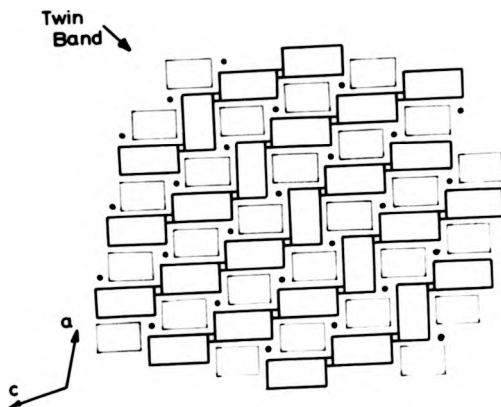


Figure 5.31 A twin Lamella in H-Nb<sub>2</sub>O<sub>5</sub>

Fig. 5.32

Twinning in H-Nb<sub>2</sub>O<sub>5</sub>

In this lattice image there are a number of large twin related domains. In general the twin boundaries are crystallographic. However in some cases highly faulted boundaries can be observed.

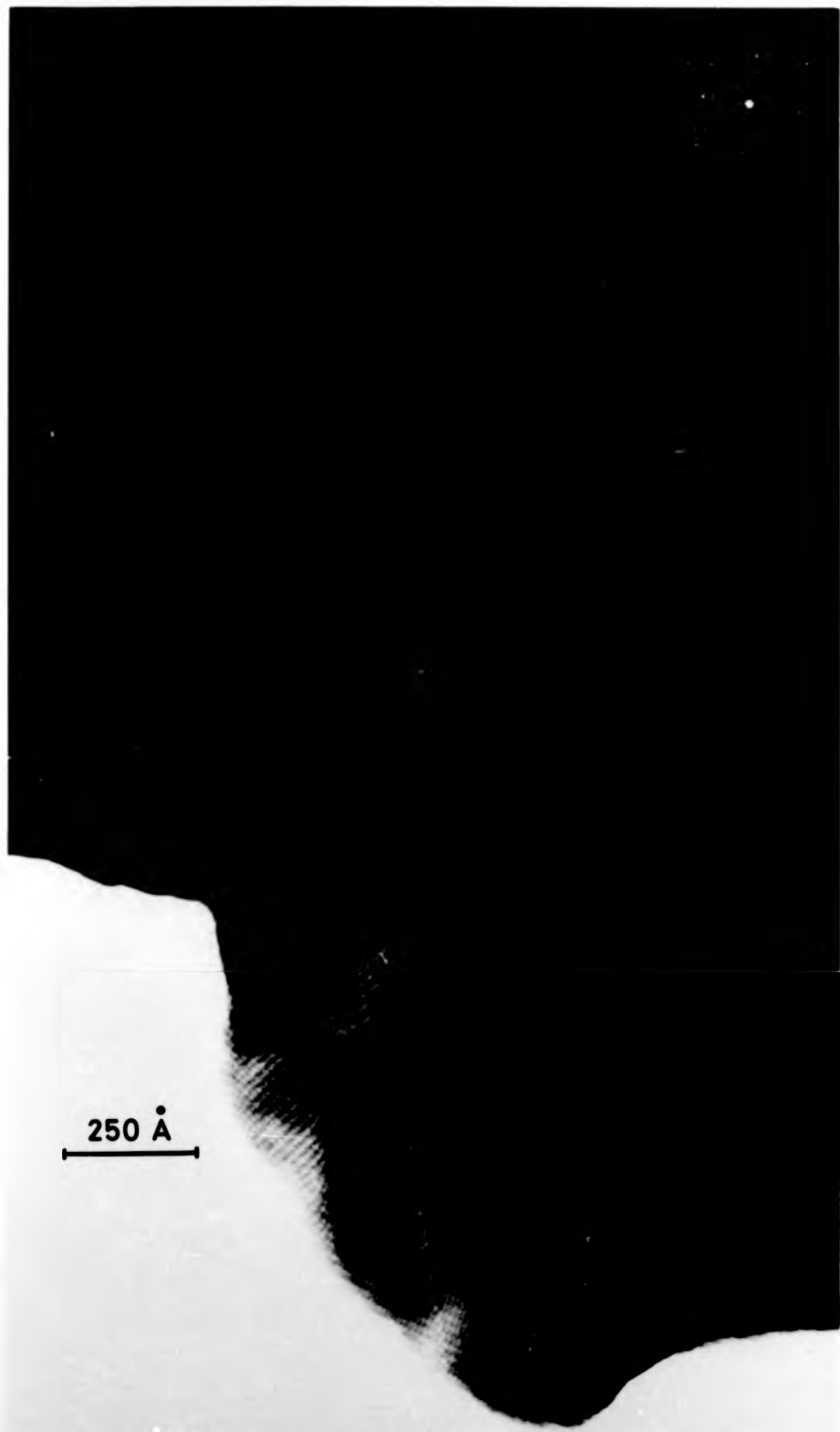


Fig. 5.32. Area of  $\text{H-Nb}_2\text{O}_5$  containing large twinned regions.

crystals generally involves no change in stoichiometry. Occasionally the twin interface deviates from the ideal  $(10\bar{1})$  twin plane and to maintain the coherency of the structure it is necessary to include "wrong-sized" blocks. The twin boundary then becomes a non-conservative fault since there is a local change in stoichiometry. Several other non-conservative planar defects can be identified from high resolution micrographs. For example, another commonly occurring defect is depicted in Figure 5.33. In this case an extra plane of  $(5 \times 3)$  blocks is incorporated into the structure.

The description of these defects and several other types of planar fault found in  $\text{H-Nb}_2\text{O}_5$  crystals has been given by Iijima (30) and Hutchison et al (31).

Since no well defined growth mechanism has been proposed for the generation of new blocks in  $\text{H-Nb}_2\text{O}_5$  crystals, it is difficult to discuss the occurrence of defects in terms of the growth behaviour. Once again the observed lattice images confirm that the incidence of defects on  $(010)$  planes is very low and that the cross-section of the blocks is preserved during growth along the  $[010]$  direction with each newly deposited layer exactly matching the previous layer.

#### Other Crystals

With the exception of the work on  $\text{NbO}_2$  crystals, the main interest in electron microscopy was to study the detailed block structure of vapour-grown oxides. Since the crystals of  $\text{NbO}$ ,  $\text{B-Nb}_2\text{O}_5$  and  $\text{P-Nb}_2\text{O}_5$  do not have suitable structures they were not studied in detail.

Electron diffraction proved to be useful for the identification of the  $\text{NbTe}_2$  crystals. However, vapour-grown crystals of  $\text{NbTe}_2$  have already been extensively studied by Amelinckx et al (33).

Fig. 5.33

A faulted region in H-Nb<sub>2</sub>O<sub>5</sub>

The fault plane indicated by the arrows in the lattice image is generated by the incorporation of an extra plane of (5 x 3) blocks as shown in the block diagram. In this case the fault is non-conservative fault, resulting a slight increase in the oxygen to niobium atom ratio.



100 Å

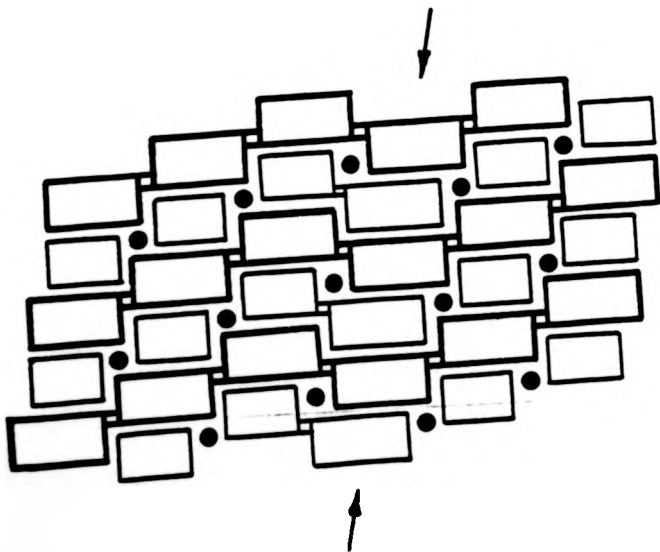


**Figure 5.33** A faulted region in  $\text{H-Nb}_2\text{O}_5$ . The arrows indicate an extra plane of  $5 \times 3$  blocks



REFERENCES

- (1) P.B. Hirsch, A. Howie, R.B. Nicholson, D.W. Pashley and M.J. Whelan, "Electron Microscopy of Thin Crystals", Butterworths, London (1965)
- (2) A. Howie and M.J. Whelan.. "Electron Microscopy of Thin Crystals" Butterworths, London (1965)
- (3) H. Hashimoto, M. Mannami and T. Naiki. Phil.Trans.R.Soc.A. 253, 459 (1961)
- (4) J. M. Cowley, Acta Cryst, 12, 367, (1959)
- (5) J. G. Allpress, E. A. Hewat, A. F. Moodie, J. V. Sanders; Acta Cryst. A28, 528 (1972)
- (6) D. F. Lynch and M. A. O'Keefe; Acta Cryst. A28, 536 (1972)
- (7) G. R. Anstis, D. F. Lynch, A. F. Moodie and M. A. O'Keefe, Acta Cryst. A29, 138, (1973)
- (8) M. A. O'Keefe, Acta Cryst. A29, 389 (1973)
- (9) (S. Iijima, Acta Cryst. A29, 18-24 (1973))
- (10) J. S. Anderson, J. M. Browne and J. L. Hutchison, J. Solid State Chem. 5, 419-431 (1972)
- (11) G. Brauer Z. anorg. allgem. chem. 248 p.1 (1941)
- (12) A. Magneli, G. Andersson and G. Sundkvist. Acta Chem.Scand. 9 p.1402 (1955)
- (13) T. Sakata, K. Sakata and I. Nishida, Phys. Stat. Sol. 20 K155 (1967)
- (14) K. Sakata. J. Phys. Soc. Japan 26, 867, (1969)
- (15) R. J. Janninck and D. H. Whitmore, J. Phys. Chem.Solids, 27, 1183-1187 (1966)
- (16) C. S. Barrett "Structure of Metals" McGraw-Hill, London (1952)
- (17) J. Billingham, P. S. Bell and M. H. Lewis. Phil. Mag. 25, 661 (1972)
- (18) M. J. Marcinkowski in "Electron microscopy and strength of crystals" eds. G. Thomas & J. Washburn, Interscience N.Y. (1962).
- (19) J. van Landuyt. Phys. stat.sol. 16, 585 (1966)
- (20) R. Norin, Acta Chem. Scand 17, 1391 (1963)
- (21) R. Norin, Acta Chem. Scand 20, 871 (1966)
- (22) A. D. Wadsley, Acta Cryst 14, 664 (1961)
- (23) S. Iijima, S. Kimura and M. Goto, Acta Cryst. A29, 632 (1973)
- (24) J. L. Hutchison and J. S. Anderson, JEOL News 10e 13-18 (1973)

- (25) J. L. Hutchison, Private Communication (1973)
- (26) S. Iijima, Acta Cryst. A29, 18-24 (1973)
- (27) S. Iijima, J. Appl. Phys. 42, 5891, (1971)
- (28) H. Schafer, D. Bergner and R. Gruehn, Z. anorg allgem.chem. 365, 31-50 (1969)
- (29) S. Kimura, J. Solid State Chem. 6, 438-449 (1973)
- (30) S. Iijima, Acta Cryst. A29, 18-24 (1973)
- (31) J. S. Anderson, J. M. Browne and J. L. Hutchison. J. Solid State Chem. 5, 419-431 (1971)
- (32) J. L. Hutchison, J. Solid State Chem. 10, 312-322, (1974)
- (33) J. van Landuyt, G. Remaut and S. Amelinckx, Phys. Stat. Sol., 41, 271 (1970)

CHAPTER SIX

SUMMARY AND DISCUSSION

The aim of this final chapter is to discuss the significance of the results of this work in terms of currently accepted ideas.

6.1 The Chemical Transport Growth Technique

The chemical transport method with tellurium tetrachloride as the transport reagent has enabled crystals of  $\text{NbO}$ ,  $\text{NbO}_2$ ,  $\text{Nb}_{12}\text{O}_{29}$ ,  $\text{H-Nb}_2\text{O}_5$ ,  $\text{B-Nb}_2\text{O}_5$  and  $\text{P-Nb}_2\text{O}_5$  to be grown. Crystals with compositions between  $\text{Nb}_{12}\text{O}_{29}$  and  $\text{Nb}_2\text{O}_5$  have also been obtained. The structure of these crystals is highly irregular and so the stoichiometry is not well defined.

In addition to the obvious versatility of the technique, growth by chemical transport has other important advantages. For example, it has been pointed out that the growth of crystals at temperatures considerably below their melting points eliminates many of the practical difficulties associated with the containment of high melting point materials. Furthermore, the range of growth temperatures which can be used often enables the lower temperature forms of crystals to be grown. This proved to be useful for the growth of B- and P- $\text{Nb}_2\text{O}_5$ .

However, there are certain disadvantages associated with crystal growth by chemical transport which can be summarised as follows:

- (a) It is difficult to control nucleation on the walls of the reaction vessel and, as a consequence of this, the crystals which are produced are generally small. For some materials, techniques of seeded growth have been developed for the production of larger crystals.
- (b) The chemistry and thermodynamics of chemical transport reactions are often very complicated and it can be difficult to establish the exact growth conditions.

(c) During the growth of some of the niobium oxides using  $\text{TeCl}_4$ , the chemistry of the reaction is such that the transport reagent is effectively "consumed". In these non-ideal processes, the total yield of certain crystal species is found to be a function of the initial concentration of the transport reagent.

### 6.2 Chemical Transport Growth in Related Systems

In the related vanadium-oxygen system,  $\text{TeCl}_4$  has been successfully used in the chemical transport growth of a range of oxides of varying composition (1,2). In each case, however, the resulting crystals corresponded closely to the composition of the source material indicating an "ideal" transport reaction. Similarly, crystals of titanium oxides (3) and iron oxides (4) have also been prepared using  $\text{TeCl}_4$  and again the evidence suggests that the process is "ideal", with no apparent degradation of the  $\text{TeCl}_4$ .

Non-ideal chemical transport of niobium oxides is not specifically associated with the use of  $\text{TeCl}_4$  as the transport reagent since Kodama and Goto (5,6) have used a range of transport reagents including  $\text{Nb}_4\text{Cl}$ ,  $\text{NH}_4\text{Br}$  and  $\text{NbCl}_5$  and in each case they observed the growth of  $\text{Nb}_{12}\text{O}_{29}$  crystals when the starting material was of a composition corresponding to  $\text{NbO}_2$ .

### 6.3 Non-Ideal Chemical Transport

The term "non-ideal chemical transport" has been used in this work to describe crystal growth processes in which the reaction at the growth zone is not the exact reverse of the source zone reaction. This will result in the composition of the crystals produced being different from the composition of the source material. However it is important to distinguish between this process and what could be termed selective

chemical transport.

Selective chemical transport refers to processes in which only part of the source material reacts with the transport reagent. In this case the products in the growth zone will generally have a different composition from the source material. However, during the course of the reaction, the overall composition of the source material will be gradually changed. This type of reaction has been frequently utilised for the separation or purification of materials.

In contrast during non-ideal chemical transport reactions the composition of the source material is not generally changed during the process, although the composition of the vapour phase compounds is.

It is useful to consider some of the implications of non-ideal chemical transport and these can be listed as follows:

- (a) The growing crystals have a different composition from the source material. This difference is accompanied by a change in the composition of the vapour phase components.
- (b) The reaction at the growth zone does not result in the complete regeneration of the transport reagent. An increasing proportion of the transport reagent becomes irreversibly combined as vapour phase reaction products.
- (c) This gradual removal of the active transport reagent means that the maximum total yield is a function of the initial quantity of reagent present.
- (d) The changing composition of the vapour phase during the transport process may result in the conditions becoming favourable for the nucleation of a different phase.
- (e) As the proportion of active transport reagent in the system is reduced, the transport rate is reduced. This leads to a fall in the effective supersaturation at the growth zone and this can

lead to differences in growth behaviour.

By applying these considerations to the niobium oxides, a number of observations can be explained.

For example, during chemical transport with  $\text{NbO}_2$  as the starting material, crystals of  $\text{Nb}_{12}\text{O}_{29}$  formed a large proportion of the yield. In all of the experiments conducted on this system, the total yield of  $\text{Nb}_{12}\text{O}_{29}$  crystals was found to be below the maximum possible yield predicted by considering the point in the reaction when all the transport reagent had been used up.

The reduction in the effective supersaturation towards the end of the growth process probably accounts for the development of  $\{110\}$  facets which were observed on many of the crystals. When growth was interrupted at an earlier stage when the supersaturation was higher, no such facets were observed.

The change in composition of the vapour phase compounds during growth eventually leads to conditions which are favourable for the growth of  $\text{NbO}_2$  crystals. As these conditions are achieved by a gradual change of vapour composition, it would seem reasonable to assume that the crystals grow under conditions of low supersaturation. Well-formed, faceted, octahedral crystals are thus obtained in this way.

The  $\text{NbO}_2$  crystals which are obtained when  $\text{NbO}$  is used as the starting material begin to grow when the concentration of the transport reagent is relatively high. It is not too surprising therefore that they adopt a different growth mechanism. However, during the course of the crystal growth the proportion of active transport reagent decreases. In some cases the concomitant decrease in the effective supersaturation has resulted in the development of  $\{111\}$  facets.

#### 6.4 Crystal Growth Mechanisms

The differences in growth mechanisms which have been observed for the various crystals can generally be interpreted in terms of the differences in crystal structure and the growth conditions.

The growth of  $\text{NbO}_2$  crystals provides a good example of the changes in growth mechanism which can occur as a consequence of changes in growth conditions. At low supersaturations, faceted growth has been observed, but at higher supersaturations a different growth behaviour involving the TPRE mechanism operates.

In the closely related block structure oxides, the principal growth direction invariably coincides with the direction of propagation of the columns of blocks. Thus both  $\text{Nb}_{12}\text{O}_{29}$  and  $\text{H-Nb}_2\text{O}_5$  grow primarily in the  $[010]$  direction. Similarly, other workers (7,8) have observed that  $\text{N-Nb}_2\text{O}_5$  and  $\text{R-Nb}_2\text{O}_5$  grow in needle form with the growth direction parallel to the columns of  $\text{ReO}_3$  type blocks. In all these oxides, the structure is such that the surface responsible for growth in the preferred direction has a network of steps with kink sites and during growth these steps are continually regenerated.

Crystals of  $\text{Nb}_{12}\text{O}_{29}$ ,  $\text{NbO}_2$  and  $\text{B-Nb}_2\text{O}_5$  frequently exhibit twinning, and the TPRE growth mechanism is important for each of these crystals. The operation of this mechanism can significantly influence the appearance of the resulting crystals. For example,  $\text{Nb}_{12}\text{O}_{29}$  crystals can grow as needles, but if a twin related region is nucleated, the crystals develop as plates.

A preliminary investigation of the octahedral form of  $\text{NbO}_2$  crystals revealed the presence of a number of triangular spiral depressions. Such features cannot easily be reconciled with the classical mechanism of dislocation generated growth. However, a model has been developed to explain these theories based on the assumption that in the vicinity of the

core, the probability of atoms becoming attached to a step site is low. Similar triangular surface depressions have been observed on octahedral surfaces of diamonds (9) and it is possible that these "trigons" could also be explained in this way.

#### 6.5 The Microstructure of the Crystals

In general, the microstructural observations obtained by transmission electron microscopy were consistent with the proposed growth mechanisms. For example, the mistakes in the block stacking sequence which were frequently observed in  $\text{Nb}_{12}\text{O}_{29}$  crystals were generally continuous. This is consistent with the model proposed for growth by the TPPE mechanism which predicts that the number and size of blocks which nucleate at a TPPE will be constrained by the existing layer which acts as the substrate.

The APB's which were observed in both types of  $\text{NbO}_2$  crystals could be explained by the nucleation and growth of antiphase domains during cooling from the growth temperature through the transition temperature. In general these APB's were not associated with dislocations.

#### 6.6 Non-Stoichiometry

In a general compound of the form MX, non-stoichiometry can be accommodated in the following five ways:

- (a) Substitution. An excess number of M atoms can occupy vacated X sites or vice-versa.
- (b) Interpolation. Sites which are normally vacant may be occupied by excess M or X atoms, or even by atoms of a third element.
- (c) Subtraction. Atoms of M or X may be missing from sites normally occupied.



(d) Crystallographic Shear. Vacant sites of M, or more usually X, may form planar arrays which collapse by shear, resulting in modified co-ordination for one type of atom.

(e) Intergrowth. Different overall compositions may be achieved by a mixture of two related compounds having a coherent interface plane.

In all these cases, non-stoichiometry is associated with lattice defects. These may be point defects such as vacancies, or planar defects such as shear planes. In general crystal defects can be categorised as either non-conservative or conservative, the non-conservative defects being responsible for local changes in stoichiometry.

It is interesting to compare the mechanisms for the accommodation of non-stoichiometry in the Nb-O system with those observed in other related systems.

In general the monoxides of the Group IVa and Va metals have large homogeneity ranges. For example, titanium monoxide has a phase field which extends from about  $\text{TiO}_{0.7}$  to  $\text{TiO}_{1.25}$  (10). This wide compositional variation is possible because vacancies can occur in both the metal and oxygen sublattices without disrupting the NaCl type structure. In many cases, ordered arrangements of these vacancies have been observed (11). Niobium oxide, however, has a more restricted range of homogeneity (12) and this implies that vacancies cannot be incorporated into the structure as readily.

Titanium dioxide has been the subject of a great deal of interest in recent years because of its tendency to accommodate non-stoichiometry by the shear plane mechanism (13). In slightly reduced rutile ( $\text{TiO}_2$ ), oxygen vacancies tend to accumulate on certain crystallographic planes and eventually the structure collapses to form shear planes (14). This

mechanism explains the wide phase field of  $\text{TiO}_2$  and the ordering of these shear planes also accounts for the formation of a Magneli series of phases related to the rutile structure (15). These Magneli phases have the general formula  $\text{Ti}_n\text{O}_{2n-1}$  (16). A similar series of phases has also been reported in the vanadium-oxygen system (17).

Niobium dioxide, however, does not exhibit the same range of composition as these related compounds. In fact Janninck and Whitmore (18) report that the homogeneity range of the  $\text{NbO}_2$  phase extends from  $\text{NbO}_{1.9975}$  to  $\text{NbO}_{2.003}$  at  $1100^\circ\text{C}$ . Thus, although  $\text{NbO}_2$  is structurally very similar to  $\text{TiO}_2$  it cannot tolerate the same degree of deviation from ideal stoichiometry. The investigation of the microstructure of "as grown"  $\text{NbO}_2$  crystals reveals the presence of a type of APB but no evidence of shear planes was obtained. The APB's which were observed have no effect on the composition of the crystals. It seems reasonable to conclude from this that non-stoichiometry in  $\text{NbO}_2$  can be accounted for by a low concentration of vacancies.

The higher niobium oxides are closely related to the  $\text{ReO}_3$  structure and can be derived from such a structure by the incorporation of a regular array of shear planes. The variations in shear plane spacing which can occur accounts for the multiplicity of phases which have been observed in the block structure niobium oxides. The ordered arrangements of shear planes which can exist constitute discrete phases and these compounds can be referred to as an homologous series having a general formula such as  $\text{Nb}_{3n}\text{O}_{8n-3}$  or  $\text{Nb}_{3n+1}\text{O}_{8n-2}$  (19). Irregularities in these ordered shear plane structures can account for small deviations from the ideal composition.

Such non-conservative faults have frequently been observed in the vapour-grown crystals and under some conditions highly disordered arrangements of blocks have been observed.

Other workers have reported significant structural effects when small impurity additions are incorporated into the structure. For example it has been established that  $N\text{-Nb}_2\text{O}_5$  is stabilised by the presence of a trace of a fluoride in the system (20). Larger additions of for example  $\text{TiO}_2$  result in the formation of ordered inter-growth structures (21).

The main achievements of the work reported in this thesis can be summarised as follows:-

- (a) The chemical transport technique using  $\text{TeCl}_4$  as the transport reagent has been developed to enable single crystals of  $\text{NbO}$ ,  $\text{NbO}_2$ ,  $\text{Nb}_{12}\text{O}_{29}$  and various polymorphic forms of  $\text{Nb}_2\text{O}_5$  to be grown.
- (b) An explanation of the non-ideal chemical transport process has been proposed. Evidence of a relationship between the maximum yield and the starting quantity of  $\text{TeCl}_4$  is presented in support of this explanation. Further support for the model comes from the identification of some of the predicted reaction by-products such as tellurium.
- (c) Growth experiments in which more than one crystal species were deposited simultaneously provided a further insight into the chemistry of the chemical transport reactions. In particular the conditions for which the growth of  $\text{NbTe}_2$  crystals was favoured were established. Furthermore, the temperature ranges over which each of the principal polymorphic forms of  $\text{Nb}_2\text{O}_5$  were stable were measured.
- (d) Each of the crystal species was examined and where possible the principal growth directions, facet

planes and twinning relationships were determined. From the morphological and crystallographic evidence, the dominant growth mechanisms were identified where possible and in some instances related to the growth conditions which existed during chemical transport.

- (e) Planar crystal defects in the  $\text{NbO}_2$  crystals were identified by conventional transmission electron microscopy as a type of antiphase boundary. These are believed to have been generated during the structural transition which occurs on cooling from the growth temperature.
- (f) For the higher oxides of niobium the detailed crystal structures were studied by H.R.E.M. Mechanisms have been suggested to account for the presence of the observed crystal defects.
- (g) A previously unreported highly disordered block structure oxide has been grown, and two-dimensional lattice images have been obtained. Within this generally disordered structure microdomains of  $\text{Nb}_{22}^{54}\text{O}_{54}$  have been identified and in one area an unreported ordered structure has been observed.

#### Further Work

Despite recent advances, the electronic transport properties of transition metal oxides are still not fully understood. There is a need for experimental data to test the models which have been proposed, and this is best obtained from single crystals.

Of particular interest to the solid state physicist are the oxides which exhibit transitions from semiconducting to metallic behaviour at well defined temperatures. Niobium dioxide is an example of this class

of oxide (18), although so far no results from single crystals have been reported.

Experiments combining techniques such as N.M.R. with electrical conductivity measurements and thermoelectric power measurements for single crystals should yield valuable information with which to test the theoretical models.

There is also clearly scope for a great deal of work aimed at the understanding of the long range forces which clearly exist in shear structures and which are responsible for the complicated ordering arrangements which are observed.

REFERENCES

- (1) K. Nagasawa, Y. Bando, T. Takada, Japan J. Appl. Phys. 9, 841, (1970)
- (2) K. Nagasawa, Y. Bando and T. Takada, J. Cryst. Growth 17, 143, (1972)
- (3) T. Niemyski and W. Piekarczyk. J. Cryst Growth 1, 177, (1967)
- (4) J. Remier. Unpublished work
- (5) H. Kodama and M. Goto. J. Cryst. Growth 29, 77 (1975)
- (6) H. Kodama and M. Goto. J. Cryst. Growth 29, 222 (1975)
- (7) H. Schafer, F. Schulte and R. Gruehn, Angew. Chem., 76, 536 (1964)
- (8) R. Gruehn, J. Less Common Metals, 11, 11 (1966)
- (9) S. Tolansky, "Surface Microtopography" p.71, Whitefriars Press (1960).
- (10) P. Ehrlich, Z. Anorg. allg. chem., 247, 53 (1941)
- (11) P. S. Bell, Ph.D. Thesis, University of Warwick(1972)
- (12) G. Brauer, Z. anorg. chem., 248, 1-31 (1941)
- (13) B. G. Hyde and L. A. Bursill, in "The Chemistry of Extended Defects in Non-Metallic Solids", Ed. L. Eyring and M. O'Keefe, North Holland, London (1969)
- (14) L. A. Bursill, B. G. Hyde, O. Terasaki and D. Watanabe, Phil.Mag. 20, 347, (1969)
- (15) L. A. Bursill and B. G. Hyde, Phil. Mag. 23, 3, (1971)
- (16) S. Andersson, Acta Chem. Scand. 14, 1161, (1960)
- (17) L. A. Bursill and B. G. Hyde, Phil. Mag. 20, 657 (1969)
- (18) R. F. Janninck and D. H. Whitmore, J. Phys. Chem. Solids, 27, 1183 (1966).
- (19) S. Iijima, Acta Cryst. A30, 251 (1974)
- (20) J. L. Hutchison and J. S. Anderson, Phys. Stat. sol.(a) 9, 207, (1972)
- (21) S. Iijima and J. G. Allpress, J. Solid State Chem. 7, 94-105 (1973).